Spring 4-20-2012

CHARACTERIZATION OF VISCOELASTIC AND FRACTURE PROPERTIES OF ASPHALTIC MATERIALS IN MULTIPLE LENGTH SCALES

Soohyok Im
University of Nebraska-Lincoln, sooim@huskers.unl.edu

CHARACTERIZATION OF VISCOELASTIC AND FRACTURE PROPERTIES OF ASPHALTIC MATERIALS IN MULTIPLE LENGTH SCALES

by

Soohyok Im

A DISSERTATION

Presented to the Faculty of

The Graduate College at the University of Nebraska

In Partial Fulfillment of Requirements

For the Degree of Doctor of Philosophy

Major: Engineering

(Civil Engineering)

Under the Supervision of Professor Yong-Rak Kim

Lincoln, Nebraska

May, 2012

CHARACTERIZATION OF VISCOELASTIC AND FRACTURE PROPERTIES OF ASPHALTIC MATERIALS IN MULTIPLE LENGTH SCALES

Soohyok Im, Ph.D.

University of Nebraska, 2012

Advisor: Yong-Rak Kim

Asphaltic materials are classical examples of multi-phase composites in different length scales. The understanding of the mechanical behavior of asphaltic materials has been a challenge to the pavement mechanics community due to multiple complexities involved: heterogeneity, anisotropy, nonlinear inelasticity, and damage in multiple forms. The micromechanics-based models based on numerical methods have been receiving attention from the pavement mechanics community because the modeling method can account for those complexities of asphaltic materials by considering the effects of material properties and geometric characteristics of individual components on overall performance behavior of mixture or structure. As a step-wise effort, this study intends to identify some of key relevant mechanical characteristics such as linear viscoelastic, non-linear viscoelastic, and fracture properties of asphaltic materials in two different length scales, e.g., mixture scale and component scale. More specifically, this study developed testing-analysis methods to rigorously define the stress-dependent nonlinear viscoelastic material characteristics at various stress levels and the viscoelastic mixed-mode fracture properties at different loading rates and testing temperatures.

The results from three-dimensional finite element simulations of the pavement structure presented significant differences between the linear viscoelastic approach and the nonlinear viscoelastic modeling in the prediction of pavement performance with respect to rutting. This implies that differences between the two approaches are considered significant and should be addressed in the process of performance-based pavement design.

The Semi-circular Bend (SCB) fracture test presented reasonable and repeatable results. The test and analysis results in this study suggest that the rate-, temperature-, mode- dependent fracture properties are necessary in the structural design of asphaltic pavements with which a wide range of strain rates and service temperatures is usually associated.

DEDICATION

This dissertation is sincerely dedicated to my wife, Jihyun Choi. Her support, and numerous scarifies made it possible.

AKNOWLEDGEMENTS

I would like to sincerely thank my advisor Dr. Yong-Rak Kim for his support and direction during my time at Lincoln. Without his guidance this dissertation would not have been possible.

I would also like to thank my committee members, Dr. Nowak, Dr. Szerszen, and Dr. Yang for their willingness to serve on my committee and provide their assistance during my graduate career.

I would like to thank my co-workers, Dr. Hoki Ban, Dr. Junghun Lee, Dr. Jamilla Lutif, Dr. Francisco Aragao, Mr. Minki Hong, Mr. Pravat Karki, Mr. Leonardo de Souza, Mrs. Ingryd Pinto, Mr. Mohammad Javaherian, and Mr. Jun Zhang for their cooperation and support.

I do not know how to thank my parents and parents-in-law for their unconditional love and support. Finally, I would like to thank my wife Jinhyun. You encouraged me to have confidence all the time. Without you I would not be here. It is now time for me to care of you and support you until the end of my life.

FINANCIAL SUPPORT

I would like to thank the Nebraska Department of Roads (NDOR) and the Mid-America Transportation Center (MATC) for the financial support.

TABLE OF CONTENTS

Page

LIST OF FIGURES

Page

LIST OF TABLES

Page

CHAPTER 1

INTRODUCTION

Distresses in asphalt pavements, such as rutting and fatigue cracking, are critical safety issues for roadway users. Rutting or permanent deformation is a surface depression resulting from the accumulation of vertical displacements in asphalt pavement layers. The presence of this distress can be even more dangerous for the roadway users when the surface depression is filled with water. Accumulation of water in the depressions not only creates unsafe conditions such as hydroplaning of the vehicles but also contributes to the loss of strength of pavement layers due to freezing and thawing cycles observed in cold regions. Large damage areas, such as potholes, are created due to severe fatigue cracking in the pavement combined with thermal stresses. Thus, pavement design methods need to take into consideration a combination of factors that cause these distresses, i.e., traffic loads, environmental effects, and composite material constituent's combinations and interactions, to improve the reliability of the structures.

To examine the effects of these factors on the pavement response, some approaches have been taken by the research community. Conventional asphalt pavement design methods assume that asphalt layers are made of materials with linear-elastic response; however, asphaltic materials present viscoelastic material behavior that is significantly affected by the rate of loading and time as well as by the temperature conditions. It has been observed that results from elastic analyses do not correlate well with field measurements. To improve the accuracy of the analyses, many studies have considered the viscoelastic constitutive model to predict the behavior of asphaltic

materials (Al-Qadi et al., 2005; Elseifi et al., 2006; Yoo. 2007; Kim et al., 2008; Kim et al., 2009). However, nonlinear response was not taken into consideration in these models in spite of abundant experimental observations (Collop et al. 2003; Masad and Somadevan 2002; Airey et al. 2004) that present nonlinear response of asphalt binders and mixes at certain levels of stress and strain. Therefore, it is necessary to consider the nonlinear viscoelastic responses which are the stress-dependent nonlinear viscoelastic material characteristics at various stress levels.

The recent mechanistic-empirical (M-E) design guide predicts fatigue cracking resistance of asphalt pavements by considering various factors mentioned above. However, the M-E design guide is known to be limited in its ability to accurately predict mechanical responses in asphaltic pavements due to the use of empirically developed prediction models based on accumulated databases from extensive laboratory tests. Recently, the fracture behavior of asphalt mixtures has been studied by several researchers performing fracture tests and numerical analysis by means of a cohesive zone model (Marasteanu et al., 2002; and Wagoner et al., 2005 and 2006; Kim et al., 2008). However, most studies were conducted at low temperature conditions and considered only pure mode I fracture due to many difficulties involved in performing mode II fracture tests. In fact, fracture behavior at intermediate service temperatures is sensitive to the loading rates, and mode I cracking does not occur solely due to traffic loads on asphalt pavements. A combination of mode I and mode II cracking, so-called mixed-mode cracking, usually occurs under load applications. Therefore, it is important to investigate not only the mode I fracture mechanisms but also the mode II crack growth behavior, including rate-dependent fracture behavior, in asphalt pavements.

There is a need for mechanistic models that can account for these material responses in asphaltic materials. As shown in Figure 1-1, asphalt mixtures are heterogeneous materials consisting of irregularly shaped and randomly oriented aggregate particles and asphalt binder. Recently, the micromechanics-based models, based on numerical methods, have been receiving attention from the pavement mechanics community, because the modeling method can account for these complexities of asphaltic materials by considering the effects of material properties and geometric characteristics of individual components on overall performance behavior of mixtures or structures. For example, a multiscale model based on numerical methods can solve these complexities of asphaltic materials by linking a homogenized global scale to a heterogeneous local scale, which can account for the effect of material heterogeneity, inelasticity, and damage evolution in the small scale on the overall performance of larger scale mixtures or structures. The micromechanics approach has a unique characteristic that is based on the concept of the representative volume element (RVE). Mechanical analyses of a large-scale heterogeneous asphalt mixture can be reasonably converted to mechanical analyses of a small-scale heterogeneous body (typically referred to as the RVE), since the selected scale is sufficient to reflect the overall behavior of the large-scale body. Micromechanics-based modeling has typically been implemented with the help of well-established computational techniques to solve composite media that exhibit extremely complex phase geometry and such inelastic mechanical behavior as viscoelasticity (Kim et al., 2005)

This study intends to identify some of the key relevant mechanical characteristics such as linear viscoelastic, non-linear viscoelastic, and fracture properties of asphaltic materials in two different length scales, i.e., mixture scale and component scale. More

specifically, this study develops testing-analysis methods to rigorously define the stress-dependent nonlinear viscoelastic material characteristics at various stress levels and the viscoelastic mixed-mode fracture properties at different loading rates and testing temperatures. These mechanical characteristics have not been fully understood in the pavement community due to difficulties involved in performing tests and analysis. Thus, outcomes from this study will provide a better understanding and identification of the true mechanical behavior of asphaltic materials, which will lead to better design of roadway structures.

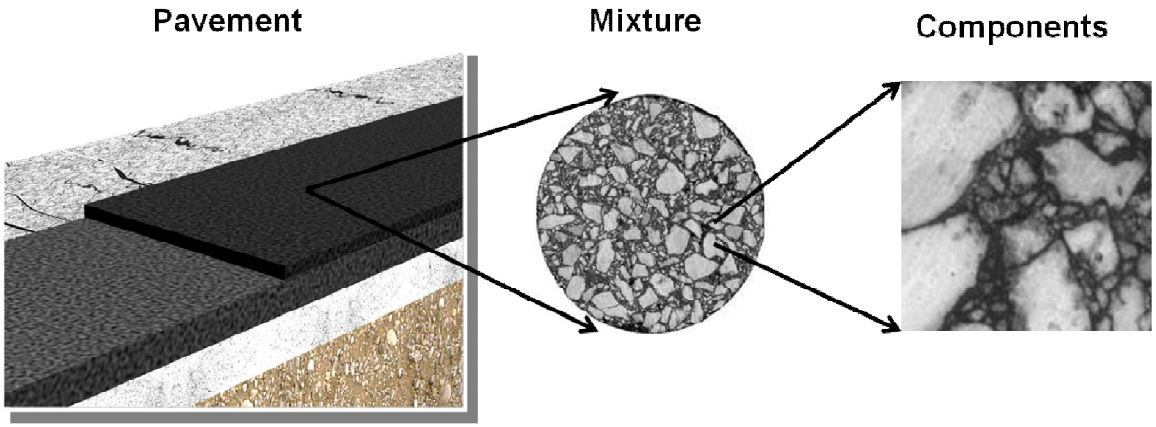

Figure 1-1. Asphaltic Media in Different Length Scales

1.1. Objectives

The primary objective of this study is to characterize material properties of asphaltic materials based on multi-scale laboratory tests. This study intends to identify some of the key relevant mechanical characteristics such as linear viscoelastic, non-linear viscoelastic, and fracture properties of asphaltic materials in two different length scales,

i.e., mixture scale (asphalt concrete (AC) mixture) and component scale (fine aggregate matrix (FAM) mixture). More specifically, the objectives are as follows:

1. Development of appropriate testing protocols for the characterization of viscoelastic properties and fracture properties of asphaltic materials,
2. Characterization of the stress-dependent nonlinear viscoelastic material properties for both AC and FAM at various stress level conditions, and
3. Characterization of viscoelastic mixed-mode fracture properties at various loading rates and testing temperatures.

1.2. Research Methodology

To meet the study objectives, appropriate testing protocols will be developed to characterize linear viscoelastic, non-linear viscoelastic, and fracture properties of asphaltic materials at two different mixture scales. Figure 1-2 illustrates the research methodology, and Table 1-1 presents the testing plan designed for this study. Details of each phase of this study are described in the following sections.

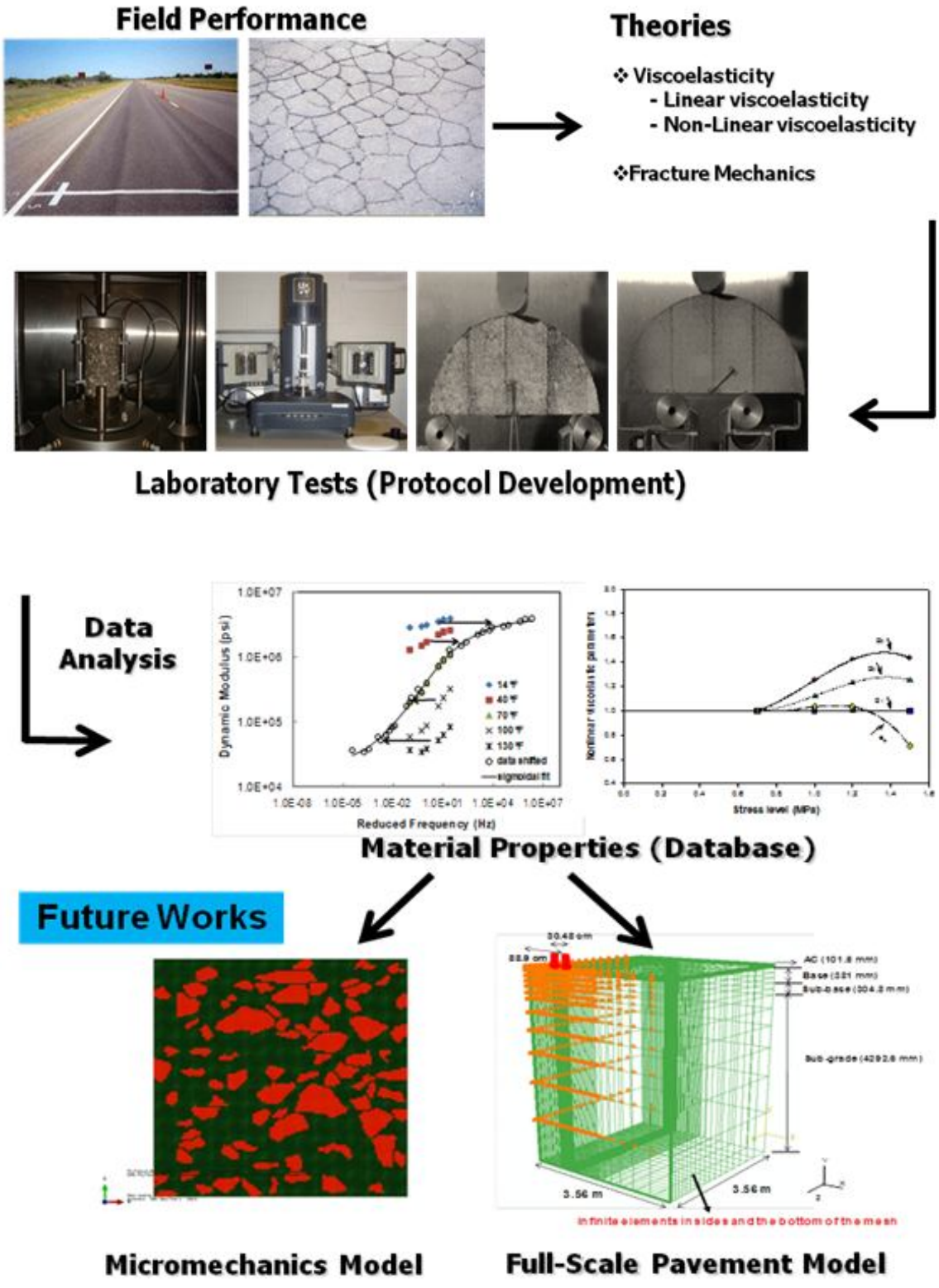

Figure 1-2. Research Methodology of This Study

Table 1-1. Laboratory Test Plan

	AC Mixture	FAM Mixture
Linear Viscoelastic Properties	- **Dynamic Modulus Test** (uniaxial compression mode at-10, 4.4, 21.1, 37.8, and 54.4°C)	- **Dynamic Modulus Test** (torsional shear mode at5, 20, and 40°C)
Non-Linear Viscoelastic Properties	- **Creep and Recovery Test** (uniaxial compression mode at 30°C)	- **Creep and Recovery Test** (torsional shear mode at 30°C)
Fracture Properties	- **Mode I Fracture Test** (semi-circular bending mode at 1, 5, 10, 50 mm/min and at -10, 0, 21, and 30°C)	- **Mode I Fracture Test** (semi-circular bending mode at 1, 5, 10, 50, 200, 600 mm/min and at 21°C) -- **Mixed-mode Fracture Test** (semi-circular bending mode at 10 mm/min and at 21°C) - **Mode II Fracture Test** (semi-circular bending mode at 5, 10, 50, 200, mm/min and at 21°C)

1.3. Organization of Dissertation

This dissertation is composed of seven chapters. Following this introduction, Chapter 2 summarizes literature reviews of studies on rutting and cracking in the asphalt pavement. Chapter 3 presents the material and testing facility used in this study. In Chapter 4, linear viscoelastic material characteristics are described based on the dynamic modulus test results. Chapter 5 identifies nonlinear viscoelastic material characteristics based on the creep and recovery test results and presents the results from three-dimensional finite element simulations of the pavement structure. Characterization of viscoelastic mixed-mode fracture properties at various loading rates and testing temperatures is presented in Chapter 6. Finally, Chapter 7 provides a summary and the conclusions for this study.

CHAPTER 2

LITERATURE REVIEW

2.1. Studies on Rutting

Rutting is one of the primary distresses in flexible pavement systems. Rutting is caused by the plastic or permanent deformation in the AC, unbound layers, and foundation soils. The M-E design guide predicts rutting performance of flexible pavements by considering the constitutive relationship between prediction of rutting in the asphalt mixture and a field-calibrated statistical analysis of laboratory repeated load permanent deformation tests. The laboratory-derived relationship is then adjusted to match the rut depth measured from the roadway. (AASHTO, 2008):

Although the M-E design guide employs various design parameters (climate, traffic, materials, etc) to predict the performance of flexible pavements, it is known to be limited in its ability to accurately predict mechanical responses in asphaltic pavements due to the use of simplified structural analysis methods, a general lack of understanding of the fundamental constitutive behavior and damage mechanisms for paving materials, and the use of circular tire loading configurations.

To overcome the limitations in the layered elastic approaches, many researchers have made tremendous efforts to develop structural mechanistic models that are able to predict the performance of asphaltic pavements. In order to represent the behavior of asphalt mixtures under different boundary conditions, it is necessary to incorporate constitutive material models into these structural mechanistic models. Computational approaches such as the finite element (FE) technique has received increased attention

from the pavement mechanics community due to its extremely versatile implementation of mechanical characteristics in addressing complex issues such as inelastic constitutive behavior, irregular pavement geometry (Blab and Harvey, 2002; Al-Qadi et al. 2002; Al-Qadi et al. 2004; Al-Qadi et al. 2005; Collop et al., 2003), and growing damage (Mun et al., 2004; Kim et al. 2006; Elseifi and Al-Qadi, 2006).

Recently, several studies (Al-Qadi et al., 2005: Elseifi et al., 2006; Kim et al., 2009) have conducted viscoelastic analyses that consider the asphalt layer as linear viscoelastic and the other layers as elastic, using the FE method in two dimensional (2-D) or three-dimensional (3-D) models for predicting the time-dependent response of flexible pavement. However, nonlinear response was not taken into consideration for their models in spite of abundant experimental observations (Collop et al.,2003; Masad and Somadevan, 2002; Airey et al. 2004) that present nonlinear response of asphalt binders and mixes at certain levels of stress and strain. For example, Figure 2-1 presents test results from Masad and Somadevan's study. As shown in the figure, the nonlinearity is evident as the shear modulus decreases with an increase in the strain level. For a linear material, the curves in the figure would coincide. Therefore, it is necessary to consider the nonlinear viscoelastic responses when asphalt pavements are subjected to heavy loads.

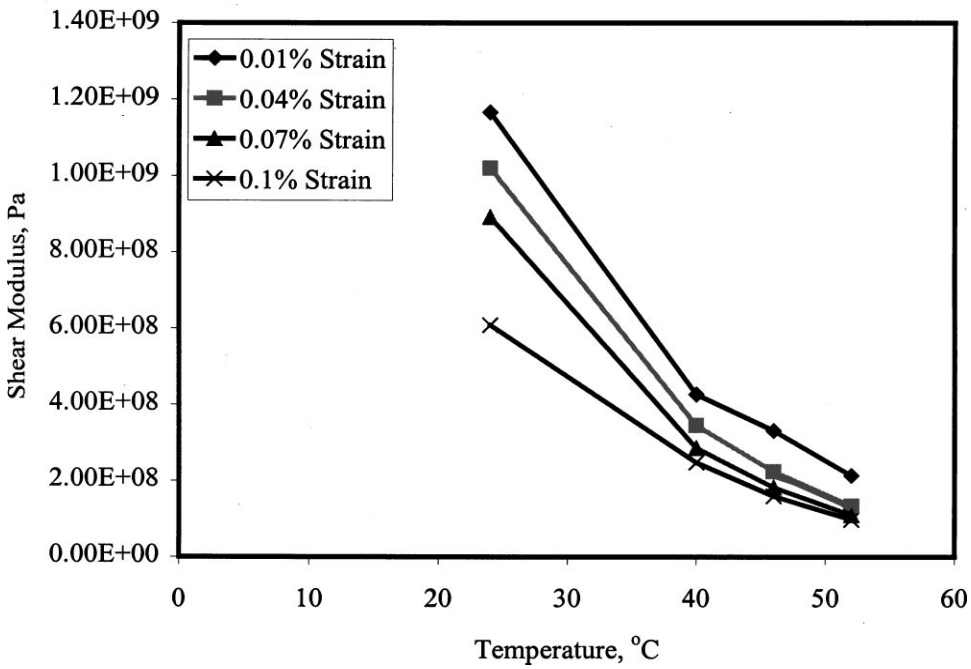

Figure 2-1. Test Results from Masad and Somadevan's Study

2.2. Studies on Cracking

Various asphalt pavement distresses are related to fracture including fatigue cracking (both top-down and bottom-up), thermal (transverse) cracking, and reflective cracking of the asphalt layer. Cracking in asphaltic pavement layers causes primary failure of the roadway structure and leads to long-term durability issues that are often related to moisture damage. The fracture resistance and characteristics of asphalt materials significantly influence the service life of asphalt pavements and consequently the maintenance and management of the pavement network. In spite of the significance, proper characterization of the fracture process and fundamental fracture properties of the asphaltic materials have not been adopted in the current pavement design-analysis procedures which are generally phenomenological.

Cracking is probably the most challenging issue to predict and control. This is because of the complex geometric characteristics and inelastic mechanical behavior of the asphalt mixtures, which are temperature sensitive and rate dependent. These characteristics make any solution to the cracking problem in asphalt mixtures almost impossible to achieve with the aid of the theory of linear elastic fracture mechanics (LEFM). LEFM is only able to predict the stress state close to the crack tips of damaged bodies if the fracture process zone (FPZ) around the crack tip is very small. The FPZ in asphaltic materials might be large, as typical quasi-brittle materials are (Bazant and Planas, 1998).

Some studies have evaluated the fracture toughness of asphalt mixtures using the J-integral concept or the stress intensity approach (Mobasher et al. 1997; Mull et al., 2002; Kim et al., 2003). Others have conducted fracture tests and numerical analyses by means of a cohesive zone model to study the fracture behavior of asphalt mixtures (Li and Marasteanu, 2005; Song et al., 2006; Kim et al., 2007; Kim et al., 2009). The cohesive zone modeling approach has recently received increased attention from the asphaltic materials and pavement mechanics community to model crack initiation and growth. This is because the cohesive zone approach can properly model both brittle and ductile fracture, which is frequently observed in asphaltic roadways due to the wide range of service temperatures and traffic speeds. Moreover, it can provide an efficient tool that can be easily implemented in various computational methods, such as finite element and discrete element methods, so that fracture events in extremely complicated mixture microstructure can also be simulated.

Most of the fracture tests have usually used conventional extensometers or clip-on gauges that are far from the actual FPZ to monitor averaged deformations or displacements of specimens for the characterization of fracture properties of asphalt mixtures. However, the true fracture properties of asphalt mixtures could be misled by as much as an order of magnitude because the material responses captured by the extensometers or clip-on gauges are limited to accurately represent material behavior at the actual FPZ. This discrepancy can become worse if the material is highly heterogeneous and inelastic (Aragão, 2011; Song et al., 2008) which is typical in asphaltic paving materials. In addition, most of the studies have adopted low-temperature testing conditions in which the type of fracture is much more brittle than it should be in order to accurately characterize fracture behavior such as fatigue cracking observed at intermediate service temperatures. However, Figure 2-2 shows test results conducted by Aragão and Kim (2011) indicating fracture behavior that is sensitive to the loading rates at intermediate temperatures.

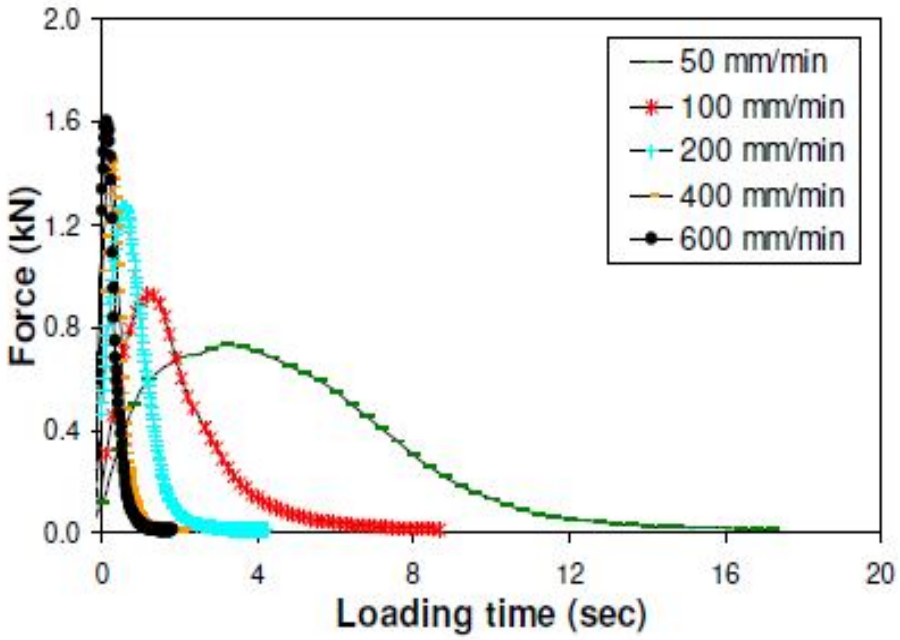

Figure 2-2. Fracture Behavior at Intermediate Service Temperatures

A better understanding of FPZ at realistic service conditions is considered a critical step to the development of mechanistic design-analysis procedures for asphaltic mixtures and pavement structures. This is because the characteristics of the FPZ represent the true material behavior related to the fracture damage, which consequently leads to the selection of proper testing methods and modeling-analysis techniques that are appropriate to address the complex local fracture process. However, such careful efforts to characterize the FPZ in asphalt concrete mixtures have not yet sufficiently been made. To the author' best knowledge, only limited attempts (Song et al., 2008; Li and Marasteanu, 2010; Seo et al., 2002; Kim et al., 2002) have been carried out due to many experimental-analytical complexities.

Most fractures occur under complex loading states and usually under a combination of opening and sliding deformation (mixed-mode). For this reason, a

number of attempts have been made to characterize mixed-mode fracture and develop test protocols in engineering materials such as rock, concrete, and ceramics (Aliha et al., 2010; Ayatollahi and Aliha, 2007; Lim et al., 1993; Lim et al., 1994). Meanwhile, in the asphalt community, much of attention has been paid to mode I fracture testing due to many difficulties involved in performing mode II fracture tests and its characterization (Kim et al., 2010; Li and Marasteanu, 2005). However, Figure 2-3 clearly shows that a combination of mode I and mode II cracking, mixed-mode cracking, occurs in asphalt concrete pavement.

Figure 2-3. Asphalt Concrete Cracking (Braham, 2008)

There are only few studies that performed mixed-mode and mode II fracture tests in asphalt pavement research community (Wagoner, 2006; Braham, 2008). They used the Single Edge Notched Beam (SEB) test for mixed-mode fracture properties using offset

notch. Braham (2008) used clip gauges to measure a combination of tensile opening and shear sliding displacements at the crack tip to capture both modes I and II fracture energies. He found that as the notch was further offset, the influence of mode II increased while the influence of mode I decreased. As they recommended, extended fracture tests should be performed to investigate the behavior of mixed-mode and mode II fracture of asphaltic materials.

CHAPTER 3

MATERIALS AND TESTING FACILITY

This chapter presents the materials and testing facility selected for this study. The asphaltic materials used are discussed in detail in two different length scales, i.e., AC mixture and FAM mixture. Also, the testing facility utilized for both the AC and FAM mixture are introduced.

3.1. Aggregates and AC Mixture

Three aggregates were selected and blended in this study: 16 mm limestone, 6.4 mm limestone, and screenings to produce the AC mixture. All three aggregates are limestone with the same mineralogical origin. The nominal maximum aggregate size (NMAS) of the final aggregate blend was 12.5 mm. Table 3-1 illustrates gradation, bulk specific gravity (G_{sb}), and consensus properties (i.e., fine aggregate angularity [FAA], coarse aggregate angularity [CAA], flat and elongated [F&E] particles) of the aggregates used in this study.

The asphalt binder used in this study was Superpave performance graded binder PG 64-28 obtained from Jebro Inc. With the limestone aggregate blend and the binder, a volumetric design of the AC mixture was developed; this resulted in a binder content of 6.0 % by weight of the total mixture to meet the 4.0 % target air voids and other necessary volumetric requirements.

Table 3-1. Gradation and Consensus Properties of Aggregates used

Sieve Analysis (Wash) for Gradation										
Aggregate Sources	19mm	12.7mm	9.5mm	#4	#8	#16	#30	#50	#100	#200
16-mm Limestone	100.0	95.0	89.0	-	-	-	-	-	-	-
6.4-mm Limestone	100.0	100.0	100.0	72.0	-	-	-	-	-	-
Screenings	100.0	100.0	100.0	100.0	36.0	21.0	14.0	10.0	7.0	3.5
Combined Gradation	100.0	95.0	89.0	72.0	36.0	21.0	14.0	10.0	7.0	3.5
Physical and Geometrical Properties										
Consensus Properties	FAA(%) = 45.0, CAA (%) = 89.0, F&E (%) = 0.0 , Gsb = 2.577									

3.2. Aggregates and FAM Mixture

The FAM mix design was developed based on the volumetric mix design of the above AC mixture containing 4 % of air voids. The FAM mixture used in this study consisted of the same PG 64-28 binder and fine aggregates smaller than 1.19 mm. The binder content used in the design of the FAM mixture was determined as 8 % by total weight of fine aggregates. Table 3-2 illustrates gradation and binder content used for the FAM mixture in this study.

Table 3-2. Gradation and Binder Content used for FAM

Sieve Analysis (Wash) for Gradation					
Sieve number and Size (mm)	#16 (1.18)	#30 (0.6)	#50 (0.3)	#100 (0.15)	#200 (0.075)
Gradation	100.0	66.7	47.6	33.3	16.7
Binder content (%)	8				

3.3. Testing Facility

UTM-25kN mechanical testing equipment was mainly used in this study. This equipment is capable of applying loads up to 25 kN static or 20 kN dynamic over a wide range of loading frequencies. As presented in Figure 3-1, an environmental chamber is incorporated with the loading frame to control testing temperatures. The chamber can control temperatures ranging from -15 ºC to 60 ºC. Better achievement of the target testing temperatures of specimens was obtained by using a dummy specimen with a thermocouple embedded in the middle of the specimen, as presented in the figure. Figure 3-1 also presents other key features and specifications of the UTM-25kN test station.

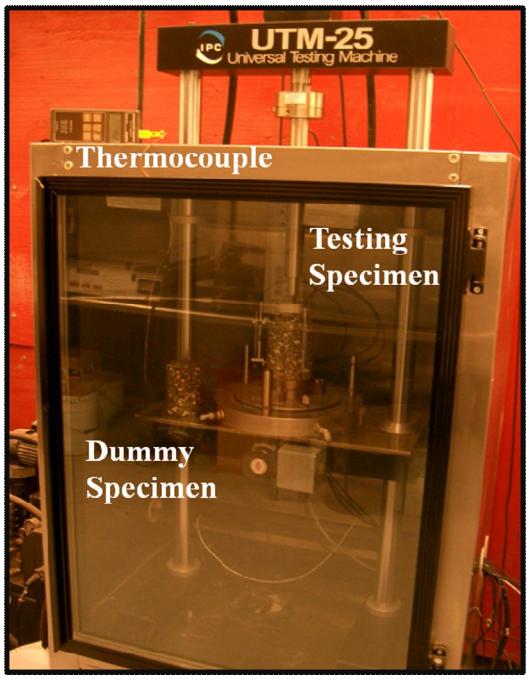

Specifications

Load Frame	
Size:	185(H) x 58(D) x 60(W) cm
Weight:	130kg
Load Capacity:	25kN static, 20kN dynamic
Between columns:	45cm
Vertical space:	80cm
Stroke:	50mm

Hydraulic Power Supply	
Size:	81(H) x 40(D) x 70(W) cm
Weight:	75kg (excluding oil)
Flow rate	5 litres/min
High pressure:	160 Bar
Low pressure:	2 to 160 Bar (adjustable)
Mains power	208V / 230V, 50 or 60Hz; 2.6kW
Noise level:	less than 70db at 2m

Figure 3-1. UTM-25kN Mechanical Test Station and Its Key Specifications

Also, an AR-2000ex Rheometer was utilized to perform the dynamic modulus test and creep and recovery test for the FAM mixture. This equipment provides not only

stable high torque output by avoiding heat issues but also superior controlled stress, controlled rate, step-strain, and direct oscillation strain control. An environmental chamber is incorporated into the loading frame, as presented in Figure 3-2, to control testing temperatures. The chamber can control temperatures ranging from -160 ºC to 600 ºC. Figure 3-2 also presents other key features and specifications of the AR-2000ex test station.

Minimum Torque Oscillation	0.1 μN.m
Minimum Torque Steady	0.1 μN.m
Maximum Torque	200 mN.m
Torque Resolution	1 nN.m
Angular Velocity Range	0 to 300 rad/s
Frequency Range	7.5E-7 to 628 rad/s
Displacement Resolution	40 nrad
Environmental Test Chamber	-160 to 600 ˚C

Figure 3-2. AR-2000ex Mechanical Test Station and Its Key Specifications

CHAPTER 4

CHARACTERIZATION OF LINEAR-VISCOELASTIC PROPERTIES

This chapter describes the dynamic modulus tests conducted for this study and presents results. Testing procedure will be described for both the AC and FAM mixture. The dynamic modulus test for the AC mixture was performed based on the standard specification AASHTO TP62 and the testing protocol for the FAM mixture was developed based on the concept of AASHTO TP62 but under the torsional shear mode. Linear viscoelastic properties (i.e., Prony series) for both the AC and FAM mixture were then characterized using test results.

4.1. Dynamic Modulus Test

The dynamic modulus test is a linear viscoelastic test for asphaltic materials. The dynamic modulus is an important input when evaluating pavement performance related to the temperature and speed of traffic loading. The loading level for the testing is carefully adjusted until the specimen deformation is between 50 and 75 microstrain, which is considered to be a level that would not cause nonlinear damage to the specimen, so that the dynamic modulus would represent the intact stiffness of asphaltic materials. Figure 4-1 presents typical test results of axial stresses and strains from the dynamic modulus test.

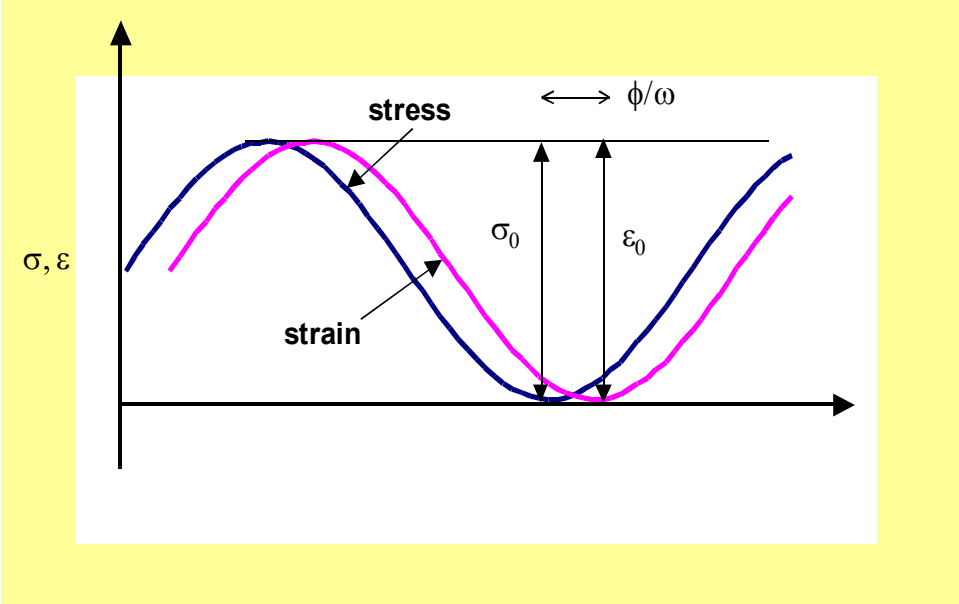

Figure 4-1.Typical Test Results of Dynamic Modulus Test

The dynamic modulus is then obtained by dividing the maximum (peak-to-peak) stress by the recoverable (peak-to-peak) axial strain, as expressed by the following equation:

$$\left|E^*\right| = \frac{\sigma_o}{\varepsilon_o} \qquad [4.1]$$

where $|E^*|$ = dynamic modulus,

σ_o = (peak-to-peak) stress magnitude, and

ε_o = (peak-to-peak) strain magnitude.

As presented in Figure 4-1, viscoelastic materials normally produce a delay between input loading (i.e., repeated stress) and output response (i.e., repeated strain)

under cyclic loading conditions. The time delay between two signals is expressed as a phase angle as follows:

$$\phi = \omega \cdot t_d = (2\pi f) \cdot t_d \quad [4.2]$$

where ϕ = phase angle (degree),

ω = angular frequency (radian/sec.),

f = loading frequency (Hz), and

t_d = time delay between stress and strain.

4.2. Linear-Viscoelastic Properties of AC Mixture

A Superpave gyratory compactor was used to produce cylindrical samples with a diameter of 150 mm and a height of 170 mm. The samples were then cored and cut to produce cylindrical specimens with a diameter of 100 mm and a height of 150 mm. The target air void of the cored and cut specimens was 4% ± 0.5%. Figure 4-2 demonstrates the specimen production process using the Superpave gyratory compactor, core, and saw machines, and the resulting cylindrical AC specimen used to conduct the dynamic modulus test.

Figure 4-2. AC Specimen Production Process for the Dynamic Modulus Testing

To measure the axial displacement of the testing specimens, mounting studs were glued to the surface of the specimens so that three linear variable differential transformers (LVDTs) could be installed on the surface of the specimens through the studs at 120^{o} radial intervals with a 100-mm gauge length. Figure 4-3 illustrates the studs affixed to the surface of a specimen. The specimen was then mounted onto the UTM-25kN equipment for testing, as shown in Figure 4-4.

Figure 4-3. Studs Fixing on the Surface of a Cylindrical Specimen

Figure 4-4. A Specimen with LVDTs Mounted in UTM-25kN Testing Station

As suggested in the AASHTO TP 62 (AASHTO TP 62-07, 2008), five temperatures (-10, 4.4, 21.1, 37.8, and 54.4 ^{o}C) and six loading frequencies (25, 10, 5, 1.0, 0.5, and 0.1 Hz) were used, and the frequency-temperature superposition concept was applied to obtain the linear viscoelastic master curves of the storage modulus in the frequency domain for a target reference temperature. The testing results of the storage modulus as a function of angular frequency were then fitted with a mathematical function (i.e., Prony series) based on the generalized Maxwell model as follows:

$$E'(\omega) = E_{\infty} + \sum_{i=1}^{n} \frac{E_i \omega^2 \rho_i^{\,2}}{\omega^2 \rho_i^{\,2} + 1} \qquad [4.1]$$

where $E'(\omega)$ = storage modulus,

ω = angular frequency,

E_{∞} = long-time equilibrium modulus,

E_i = spring constants in the generalized Maxwell model,

ρ_i = relaxation time, and

n = number of Maxwell units in the generalized Maxwell model.

Using the Prony series parameters (E_∞, E_i, and ρ_i) obtained by fitting the experimental data with storage modulus, the relaxation modulus can be expressed in the time domain as follows:

$$E(t) = E_\infty + \sum_{i=1}^{n} E_i e^{-\frac{t}{\rho_i}} \qquad [4.2]$$

where $E(t)$ = relaxation modulus in time domain, and

t = loading time.

If the relaxation moduli at a reference temperature T_o are known, the stress relaxation moduli at any given arbitrary temperature T can be obtained by using a time-temperature shift factor a_T as follows:

$$a_T = \frac{t_T}{t_{T_o}} \qquad [4.3]$$

A total of four replicates were tested and values of storage modulus at each different testing temperature over the range of loading frequencies were obtained. Figure 4-5 presents test results. The test results among the replicates at the same testing conditions were repeatable without large discrepancies.

The test results from replicates were then averaged to produce 30 individual storage moduli at all levels of temperature and frequency to produce a stiffness master curve constructed at a reference temperature. The reference temperature is -10, 0, 21, or 30 ^{o}C for this study, because they are the temperatures used to conduct the SCB fracture tests which are simulated through the finite element model to characterize local fracture properties of the mixture as discussed in later sections. The master curve represents the stiffness of the mixture in a wide range of loading frequencies (or loading times, equivalently). Master curves are constructed using the time (or frequency) - temperature superposition by shifting data at various temperatures with respect to loading frequency until the curves merge into a single smooth function. After the shifting is completed, the master curve at an arbitrary reference temperature was then fitted with the Prony series (shown in Eq. [4.1]) to determine linear viscoelastic material parameters. Table 4-1 presents Prony series parameters determined for each different reference temperature.

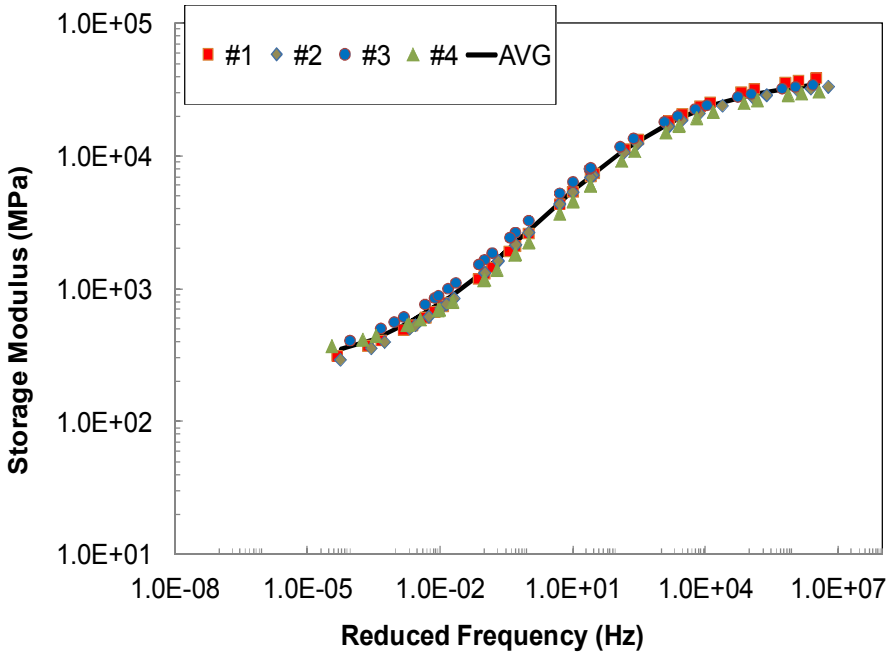

Figure 4-5. Dynamic Modulus Test results of AC mixture (storage moduli vs. loading frequencies)

Table 4-1. Linear Viscoelastic Properties of AC Mixture at Different Temperatures

Reference Temperature	-10 °C		0 °C		21 °C		30 °C	
Prony Series Parameters	E_i (MPa)	ρ_i (sec)	E_i (MPa)	ρ_i (sec)	E_i (MPa)	ρ_i (sec)	E_i (MPa)	ρ_i (sec)
1	7391.7	1.0E+00	8095.7	1.0E-05	9095.4	1.0E-05	9028.5	1.0E-05
2	5931.0	1.0E+01	5312.2	1.0E-04	6778.9	1.0E-04	4721.3	1.0E-04
3	6561.0	1.0E+02	4754.5	1.0E-03	7001.4	1.0E-03	4216.1	1.0E-03
4	4526.6	1.0E+03	2243.3	1.0E-02	4250.9	1.0E-02	1879.0	1.0E-02
5	2679.8	1.0E+04	1089.9	1.0E-01	2286.2	1.0E-01	999.9	1.0E-01
6	1238.2	1.0E+05	423.5	1.0E+00	962.4	1.0E+00	397.9	1.0E+00
7	566.9	1.0E+06	203.6	1.0E+01	430.7	1.0E+01	205.7	1.0E+01
8	252.6	1.0E+07	89.8	1.0E+02	186.8	1.0E+02	93.2	1.0E+02
9	124.1	1.0E+08	47.3	1.0E+03	92.8	1.0E+03	52.0	1.0E+03
10	61.0	1.0E+09	23.5	1.0E+04	45.3	1.0E+04	26.2	1.0E+04
11	72.6	1.0E+10	9.1	1.0E+05	53.8	1.0E+05	34.0	1.0E+05
∞	236.1	-	323.7	-	215.3	-	229.5	-

4.3. Linear-Viscoelastic Properties of FAM Mixture

As with the AC mixture, the Superpave gyratory compactor was used to produce a cylindrical FAM sample with a diameter of 150 mm and a height of 80 mm. The sample was then cut into three parts; the middle parts were 45 mm in height and 150 mm in diameter. Figure 4-6 demonstrates the specimen production process using the Superpave gyratory compactor, core, and saw machines, and the resulting cylindrical FAM specimen used to conduct the dynamic modulus test.

Figure 4-6. FAM Specimen Production Process for the Dynamic Modulus Testing

The FAM specimen was installed onto the AR-2000ex Rheometer equipment for testing (Figure 4-7). The FAM specimen was then subjected to the dynamic modulus test under the torsional shear mode as presented in Figure 4-7. A low torsional strain of 0.006 %, which is the level of strain within the linear viscoelastic range, was applied to the FAM specimen with varying frequencies from 25 Hz to 0.01 Hz at three different temperatures of 5 °C, 20 °C, and 40 °C, respectively.

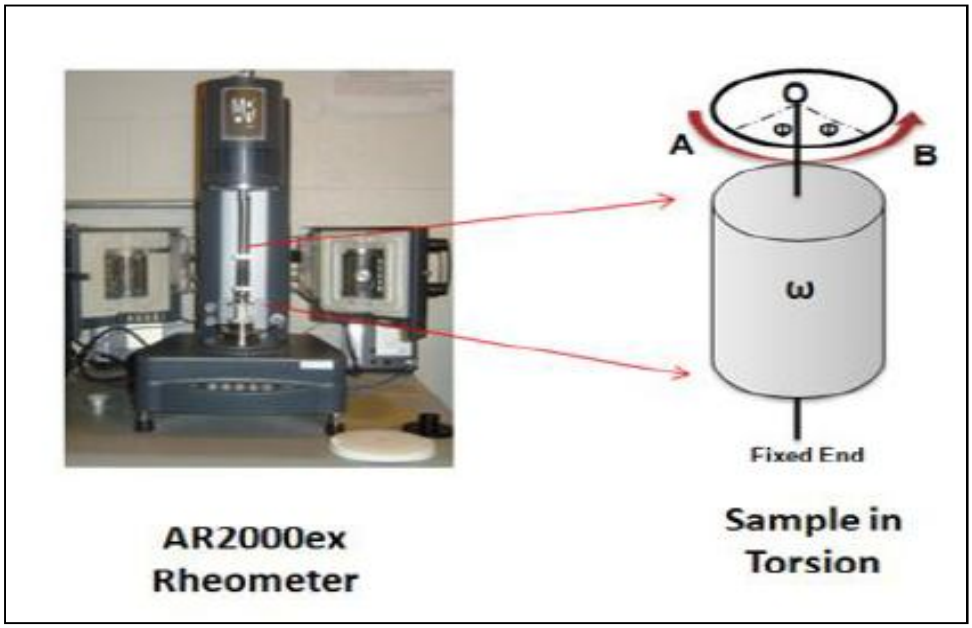

Figure 4-7. Picture of AR-2000 Testing Station and Test Methodology

A total of four replicates were tested and values of storage modulus at each different testing temperature over the range of loading frequencies were obtained. As shown in Figure 4-8, master curves at the reference temperature of 21 °C were constructed because of the simulation of the SCB fracture tests that will be described in later sections. Table 4-2 presents Prony series parameters determined for at the reference temperature of 21 °C.

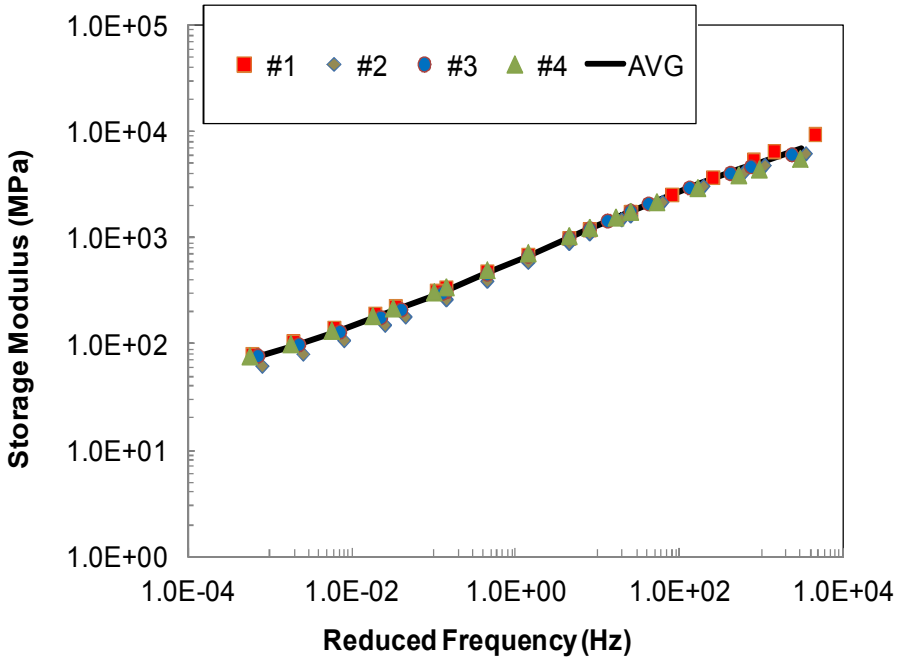

Figure 4-8. Dynamic Modulus Test results of FAM Mixture (storage moduli vs. loading frequencies)

Table 4-2. Linear Viscoelastic Properties of FAM Mixture at 21 °C

Reference Temperature	21°C	
Prony Series Parameters	E_i (MPa)	ρ_i (sec)
1	20515.3	2.00E-06
2	9010.5	2.00E-05
3	8776.6	2.00E-04
4	4062.5	2.00E-03
5	2347.2	2.00E-02
6	927.8	2.00E-01
7	455.7	2.00E+00
8	183.8	2.00E+01
9	95.1	2.00E+02
10	43.6	2.00E+03
11	57.3	2.00E+04
∞	49.5	-

CHAPTER 5

CHARACTERIZATION OF NONLINEAR-VISCOELASTIC PROPERTIES

This chapter describes the creep and recovery test conducted for this study and presents results. Testing protocol for the creep and recovery test was developed to characterize nonlinear viscoelastic material properties of both the AC and FAM mixture, respectively. Test results were then used to identify linear and nonlinear viscoelastic material properties of both the AC and FAM mixture.

5.1. Creep and Recovery Test

The creep and recovery test can be used to characterize the non-linear viscoelastic material property of asphaltic materials. The approach most often used in the literature to obtain the nonlinear viscoelastic material properties is based on Schapery's procedure using numerical fitting of laboratory test data both in the linear range and in the nonlinear range at each stress level (Lai and Bakker 1996; Zaoutsos and Papanicolaou 2010; Huang et al. 2011). Schapery's nonlinear viscoelastic single-integral model (Schapery, 1969) for one-dimensional problems can be expressed in terms of an applied stress (σ^τ) as follows:

$$\varepsilon^t = \varepsilon(t) = g_0 D_0 \sigma^t + g_1 \int_0^t \Delta D\left(\psi^t - \psi^\tau\right) \frac{d\left(g_2 \sigma^\tau\right)}{d\tau} d\tau \qquad [5.1]$$

where ψ is the reduced time given by:

$$\psi^t = \psi(t) = \int_0^t \frac{d\xi}{a_T a_\sigma} \qquad [5.2]$$

where superscript t is current time; g_0, g_1, and g_2 are the nonlinear viscoelastic parameters related to stress status; a_T is the temperature shift factor, and a_σ is the stress shift factor. In addition to the temperature and stress effects, the effects of moisture and physical aging can also be included by adding their own time-scaling functions in Equation (5.2). Only the nonlinear effect due to stresses is considered in this study.

5.2. Creep and Recovery Test of AC Mixture

To conduct the uniaxial static creep-recovery tests, AC specimens were fabricated as illustrated in Figure 4-2. The AC specimen was then mounted onto the UTM-25kN equipment for testing, as shown in Figure 4-4. The static creep-recovery test was conducted on replicate specimens of the AC mixture at 30 °C. A creep stress for 30 seconds (followed by recovery for 1,000 seconds) was applied to the specimens, and the vertical deformation (in compression) was monitored with the three LVDTs. Various stress levels were applied to characterize nonlinear behavior of the AC mixture for a large range of stress levels. Table 5-1 presents applied stress levels for the AC mixture.

Based on the preliminary test results, the threshold stress (reference stress) of nonlinear viscoelasticity was found to be 700 kPa at 30 °C. In other words, the AC mixture was considered linear viscoelastic below the reference stress level at that testing temperature of 30 °C. Figure 5-1 presents test results. As expected, the higher stress level generated larger creep strain and allowed less recovered strain.

Table 5-1. Applied Stress Levels for AC Mixture

Mix	Temp.	Stress Level (kPa)			
AC mixture	30 °C	700	1,000	1,200	1,500

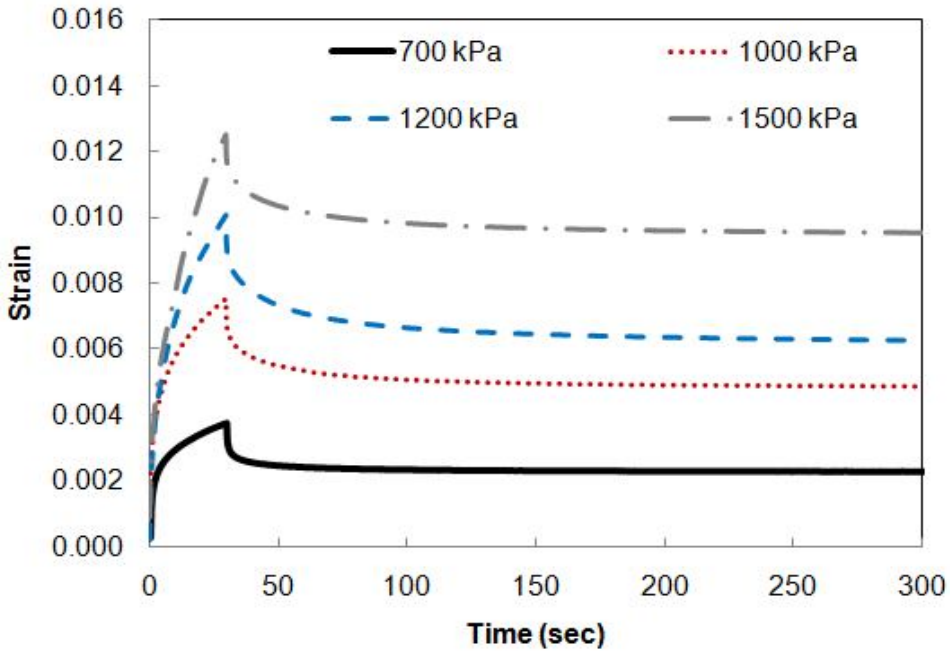

Figure 5-1. Creep and Recovery Test Results of AC Mixture

5.3. Creep and Recovery Test of FAM Mixture

The FAM specimens were prepared as presented in Figure 4-7. The FAM specimen was then mounted onto the AR-2000ex Rheometer for testing (Figure 4-8). Similarly, static creep-recovery tests were conducted on replicate specimens of the FAM mixture under the torsional shear mode at 30 °C by applying a creep stress for 30 seconds (followed by recovery for 1,000 seconds). Various stress levels were applied to determine

nonlinear behavior of the FAM mixture for a large range of stress levels. Table 5.2 presents applied stress levels for the FAM mixture.

Table 5-2. Applied Stress Levels for FAM Mixture

Temp.	Stress Level (kPa)							
30 °C	5	10	15	20	30	40	50	75

Based on the preliminary test results, the threshold stress (reference stress) of nonlinear viscoelasticity was found to be between 15 kPa and 20 kPa at 30 °C. Figure 5-2 presents creep and recovery test results of replicate specimens of the FAM mixture. As expected again, the higher stress level generated larger creep strain and allowed less recovered strain.

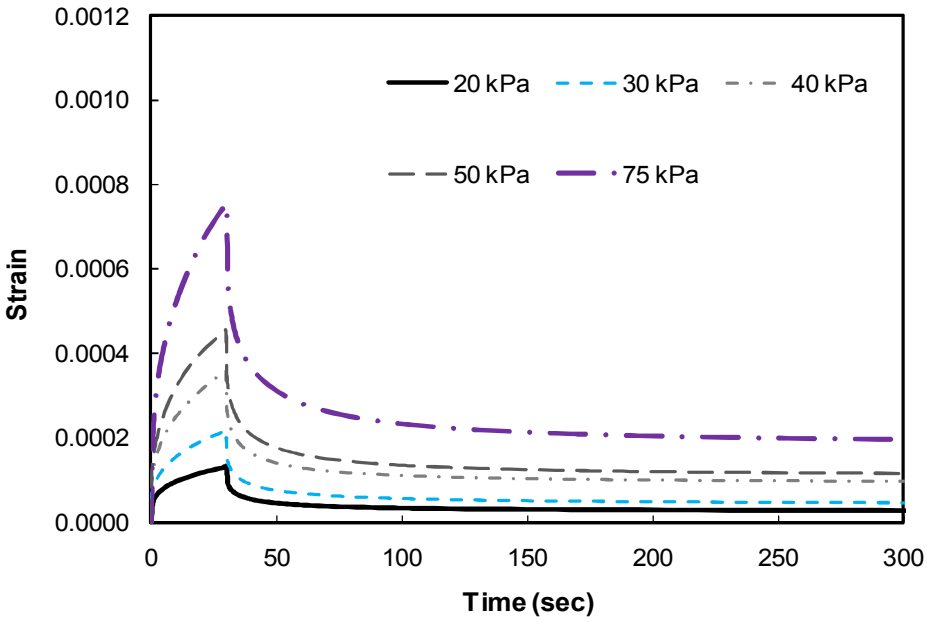

(a) FAM specimen No.1

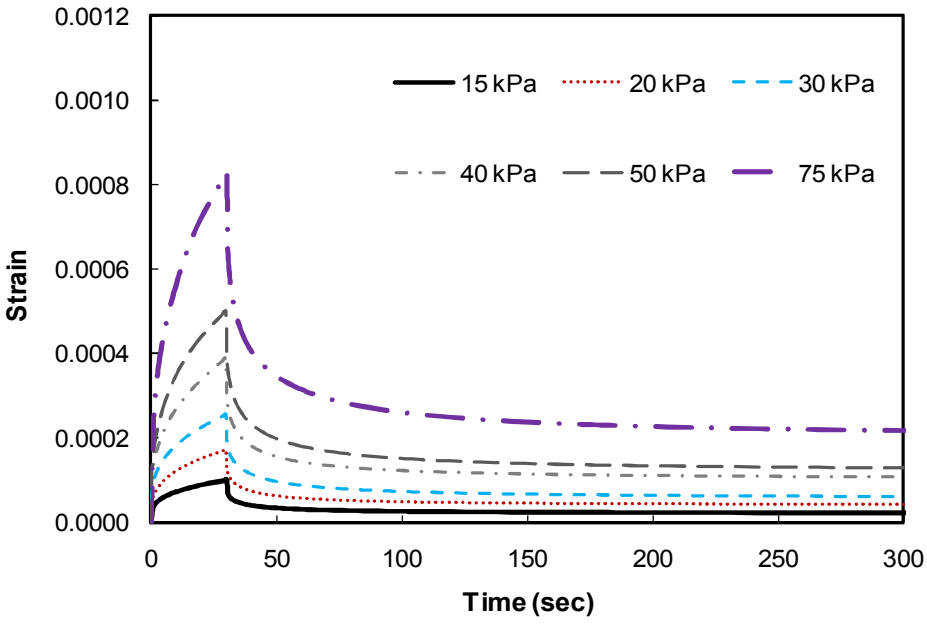

(b) FAM specimen No.2

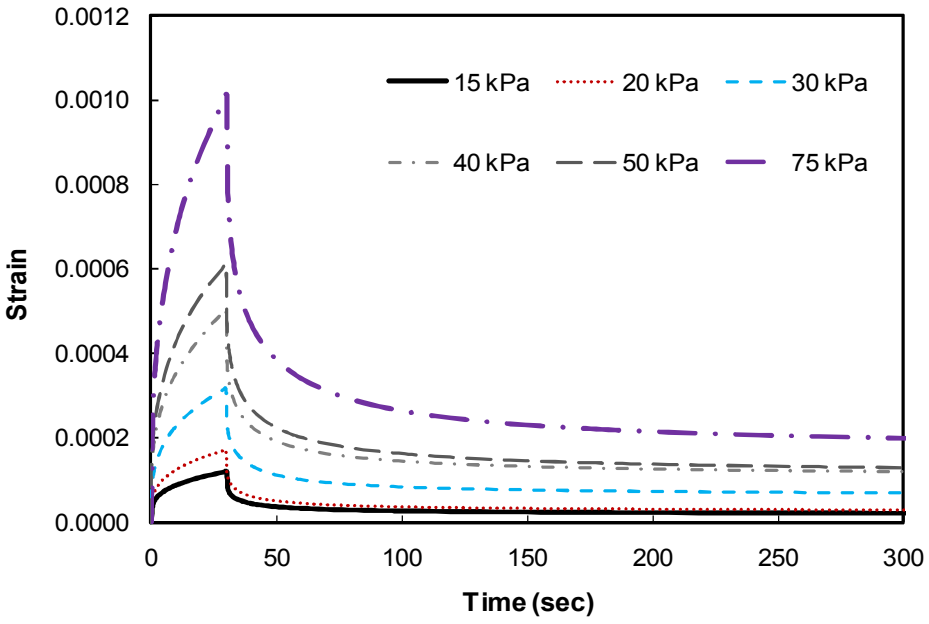

(c) FAM specimen No.3

Figure 5-2. Creep and Recovery Test Results of FAM Mixture

5.4. Characterization of Viscoelastic Properties

The creep-recovery test results presented in this chapter were used to identify viscoelastic material properties. The procedure to define nonlinear viscoelastic properties started with the identification of linear viscoelastic material properties using the test results at the threshold stress level. The linear viscoelastic properties were then used to find nonlinear viscoelastic properties by using creep-recovery test data resulting from higher stress levels than the threshold level. Finally, all viscoelastic material properties (linear and nonlinear) were found.

A schematic of a single creep-recovery test is illustrated in Figure 5-3 for a constant stress loading and unloading condition. For the loading time period, i.e., $0 < t < t_1$, Equation (5.1) can be expressed as:

$$\varepsilon_c(t) = g_0 D_0 \sigma + g_1 g_2 \sigma \Delta D\left(\frac{t}{a_\sigma}\right) \quad [5.3]$$

For the unloading time period, that is, $t > t_1$, it can be expressed as:

$$\varepsilon_r(t) = g_2 \sigma \left[\Delta D\left(\frac{t_1}{a_\sigma} + t - t_1\right) - \Delta D\left(t - t_1\right)\right] \quad [5.4]$$

$$\Delta D^{\psi^t} = D_c \psi^n \quad [5.5]$$

where D_c and n are material constants.

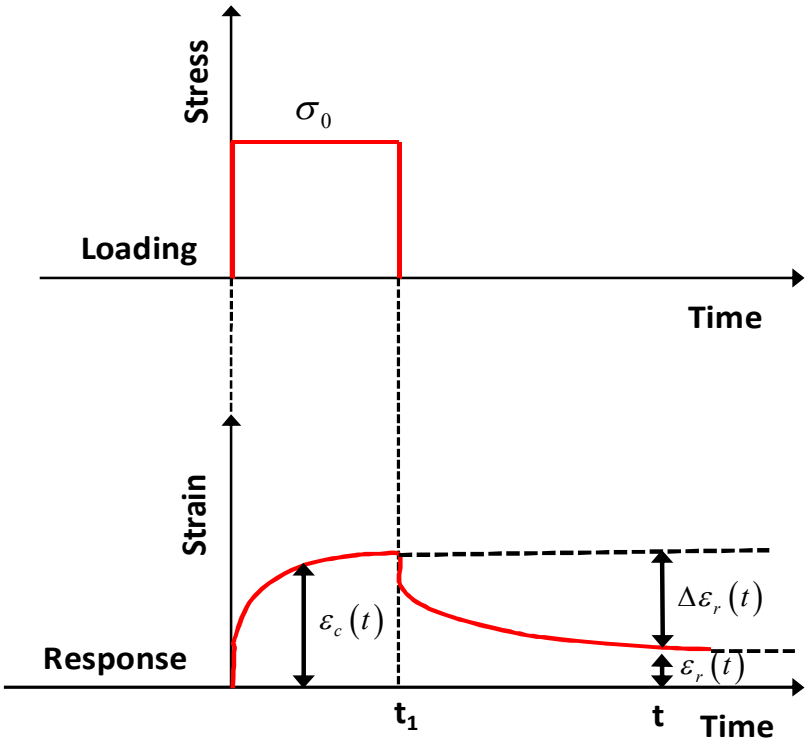

Figure 5-3. A Schematic of a Single Creep-Recovery Test

The first step is to obtain linear viscoelastic material properties (D_0, D_C, and n) at the threshold stress level. Since the recoverable response is linear viscoelastic ($g_0 = g_1 = g_2 = a_\sigma = 1$) at the threshold stress level, the recovered strain $\Delta\varepsilon_r$ shown in Figure 5-3 can be used to obtain the linear viscoelastic material properties. Substituting Equation (5.5) into Equations (5.3) and (5.4) gives:

$$\begin{aligned}\Delta\varepsilon(r) &= \varepsilon_c(t_1) - \varepsilon_r(t) \\ &= \alpha^* - \beta^*\left[(1+a_\sigma\lambda)^n - (a_\sigma\lambda)^n\right]\end{aligned} \quad [5.6]$$

where

$$\alpha^* = g_0 D_0 \sigma + g_1 g_2 D_c \sigma \left(\frac{t_1}{a_\sigma}\right)^n \quad [5.7]$$

$$\beta^* = g_2 D_c \left(\frac{t_1}{a_\sigma}\right)^n \quad [5.8]$$

$$\lambda = \frac{t - t_1}{t_1} \quad [5.9]$$

Fitting Equation (5.6) to the recovered strains $\Delta\varepsilon_r$ can determine constants: n, α^*, β^*, and a_σ. It is also noted that n is almost stress-independent and can be obtained at a low stress level; therefore, the n value is fixed as a material constant, and the values of α^*, β^* and a_σ are obtained by repeating the fitting process. Next, from Equation (5.8), g_2 is determined by minimizing errors between experimental data and Equation (5.8). Similarly, g_0 and g_1 are determined from Equation (5.7). Figure 5-4 presents all

nonlinear viscoelastic parameters of the AC mixture, which were fitted to polynomial functions so that each property can be represented as a function of stress levels. Similarly, Figure 5-5 shows all nonlinear viscoelastic parameters of replicate specimens of the FAM mixture. The figures show that parameter g_1 is not significantly related to nonlinearity, whereas other parameters such as g_0 and g_2 are affected by stress levels beyond the reference stress level. Both parameters generally increased as higher stresses were involved.

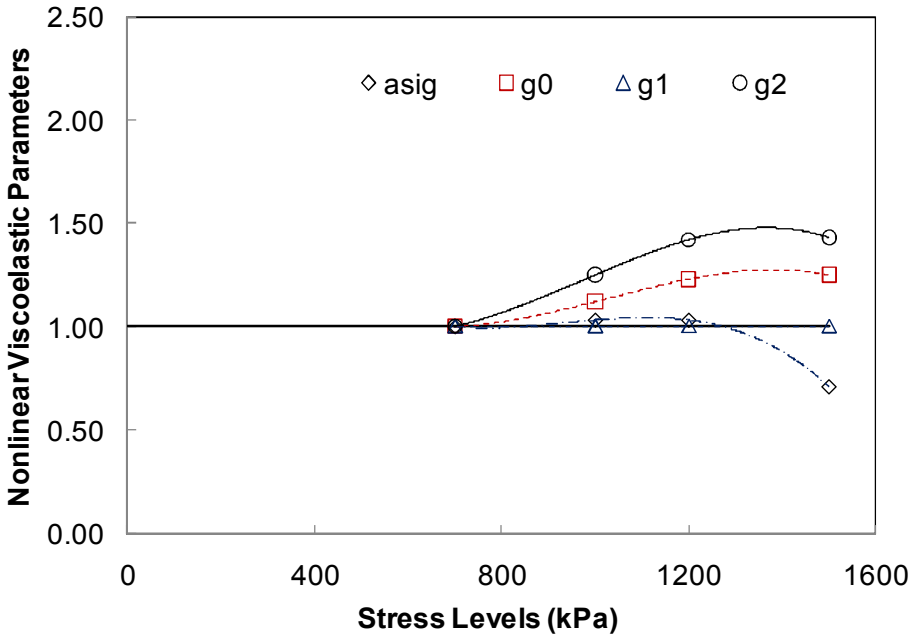

Figure 5-4. Stress-Dependent Nonlinear Viscoelastic Parameters of AC Mixture

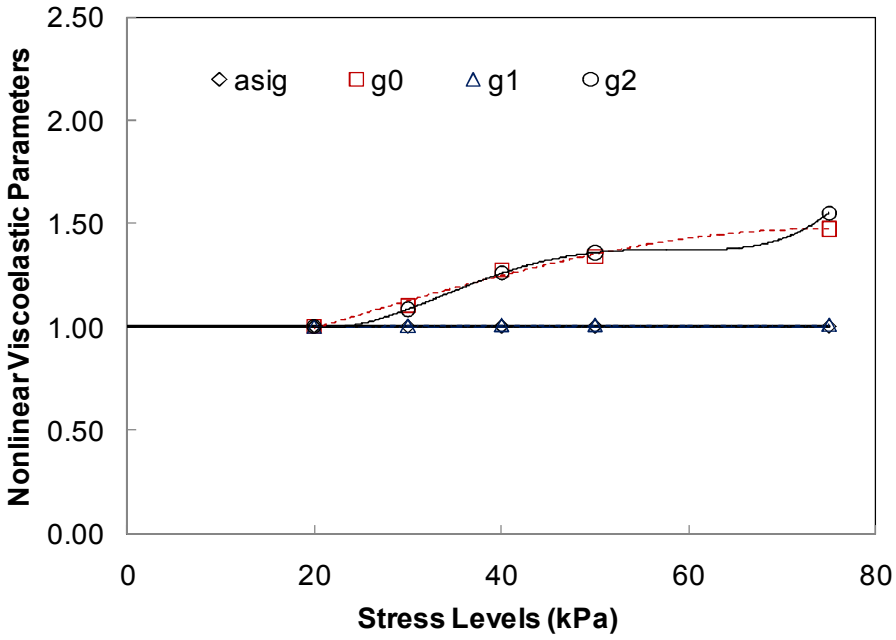

(a) FAM specimen No.1

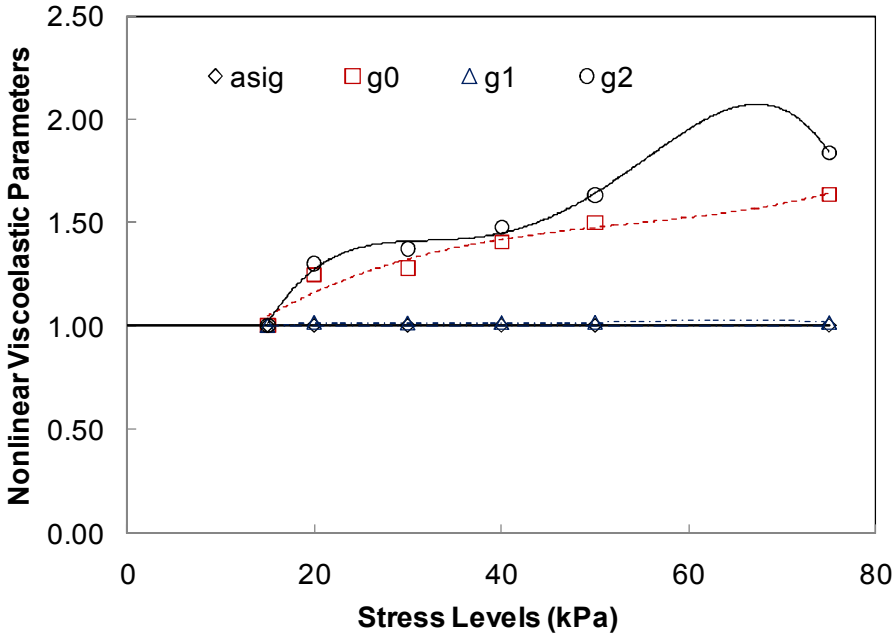

(b) FAM specimen No.2

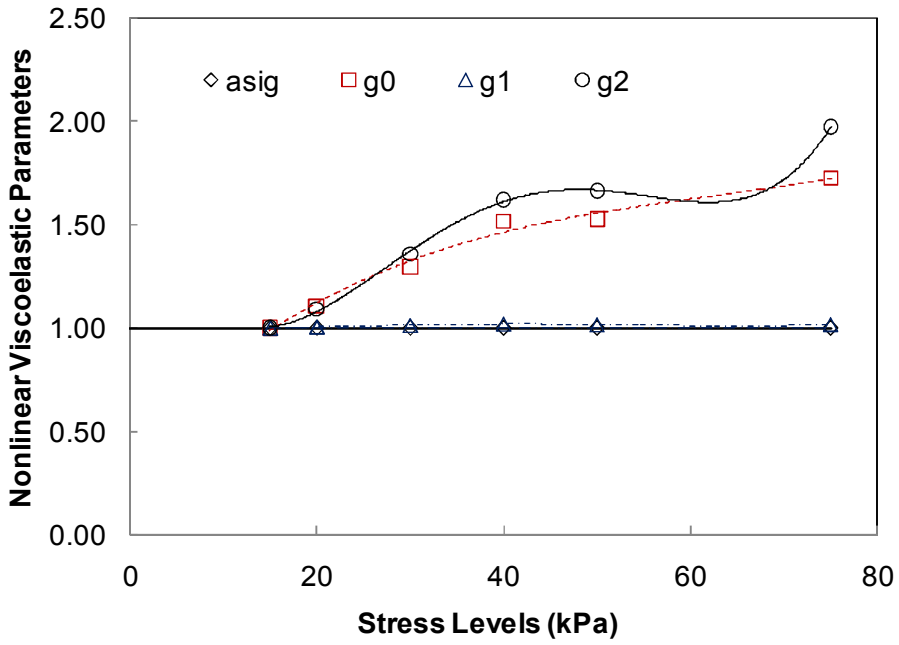

(c) FAM specimen No.3

Figure 5-5. Nonlinear Viscoelastic Parameters of FAM Mixture

5.5. Example of FE Analysis of Pavement

A typical pavement structure subjected to repeated heavy truck loads was modeled to consider the effect of material nonlinearity, the viscoelastic material properties of the AC mixture. Schapery's nonlinear viscoelastic constitutive model was implemented into the commercial finite element (FE) software ABAQUS via the user defined subroutine (user material, or UMAT), developed at the University of Nebraska-Lincoln (Kim et al. 2011).

Figure 5-6 illustrates a three-layered asphalt pavement structure selected (101.6-mm thick asphalt layer, 203.2-mm thick base, and 1270-mm subgrade) and its 3-D finite element mesh. Only a quarter of the whole domain, subject to a single axle loading in dual-tire, was modeled due to its symmetry. The right hand side of the vertical edge was

fixed in the horizontal direction; the bottom of the mesh was fixed in the vertical direction representing bedrock. In order to alleviate computational expense, infinite elements (CIN3D8 in ABAQUS) were used at the boundaries far from the loading zone. (Ban et al.,2011)

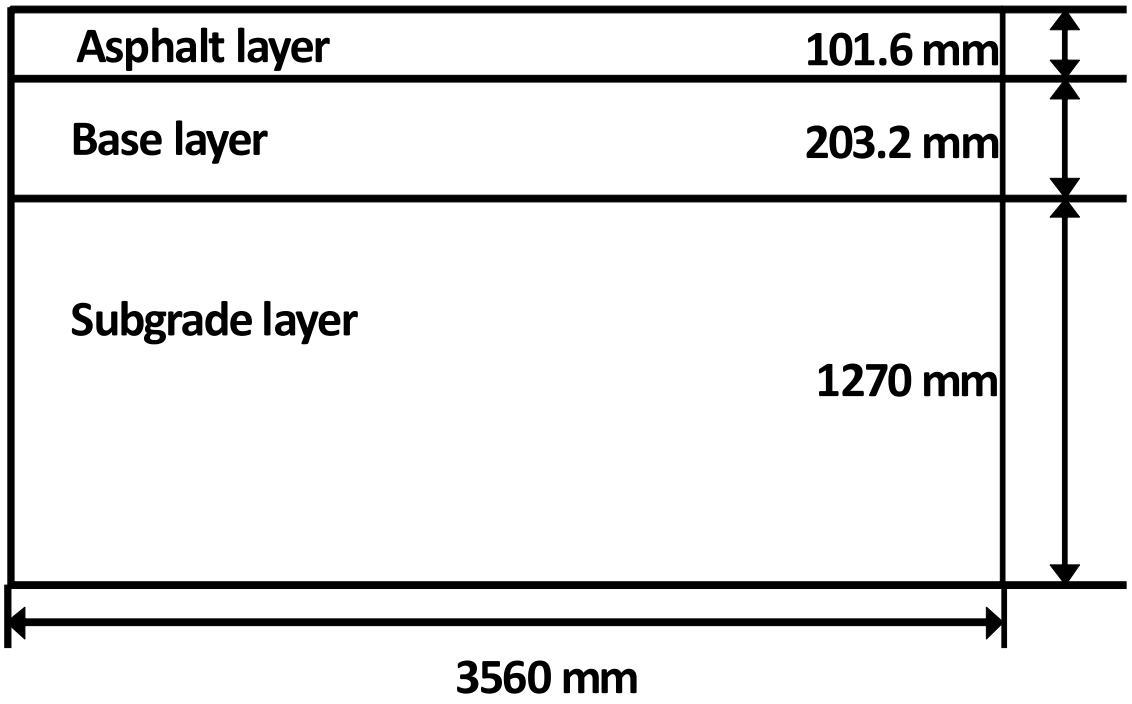

(a) A Three-Layered Asphalt Pavement Structure to be Modeled

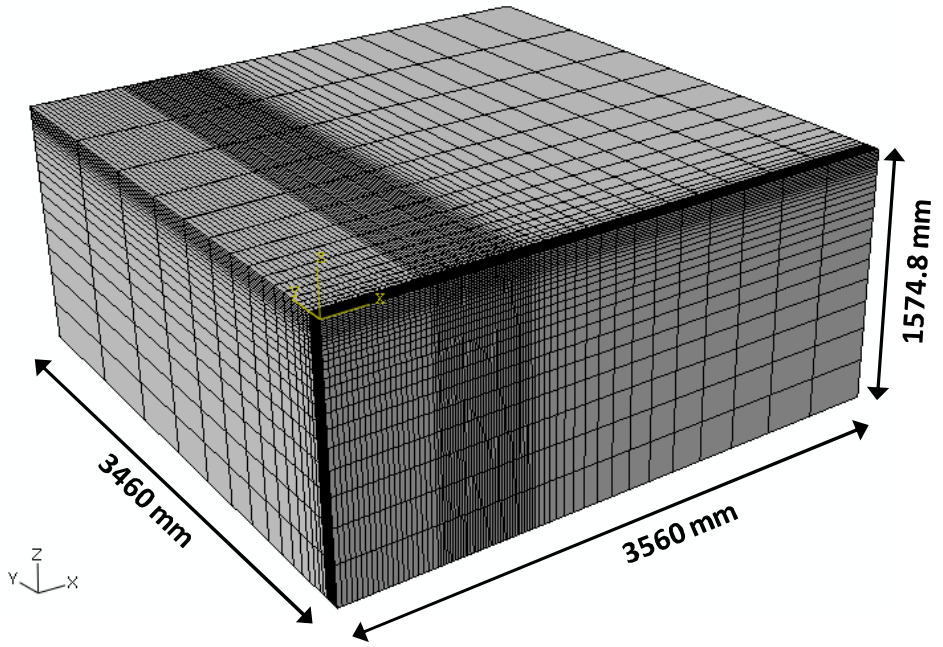

(b) Three-Dimensional Finite Element Mesh

Figure 5-6. A Pavement Geometry Selected for Finite Element Modeling

A tire pressure of 720 kPa and axial load of 35.5 kN were applied to the pavement (Yoo, 2007). Figure 5-7 illustrates the loading configuration of the Class 9 truck used in this study (Soares et al. 2008). Although the truck loading consists of a front steer axle and two tandem axles with dual tires, to reduce computational time in the analysis only the two tandem axles with dual tires were selected through use of the trapezoidal loading sequence shown in Figure 5-7. A 15.4-m Class 9 truck trailer traveling at 80 km/h takes 0.692 seconds to pass over a fixed point on the pavement. Therefore, the first truck passes the fixed point for 0.692 seconds and, after 30 seconds, a second truck passes through the same point. The passage of a total of 50 trucks was simulated.

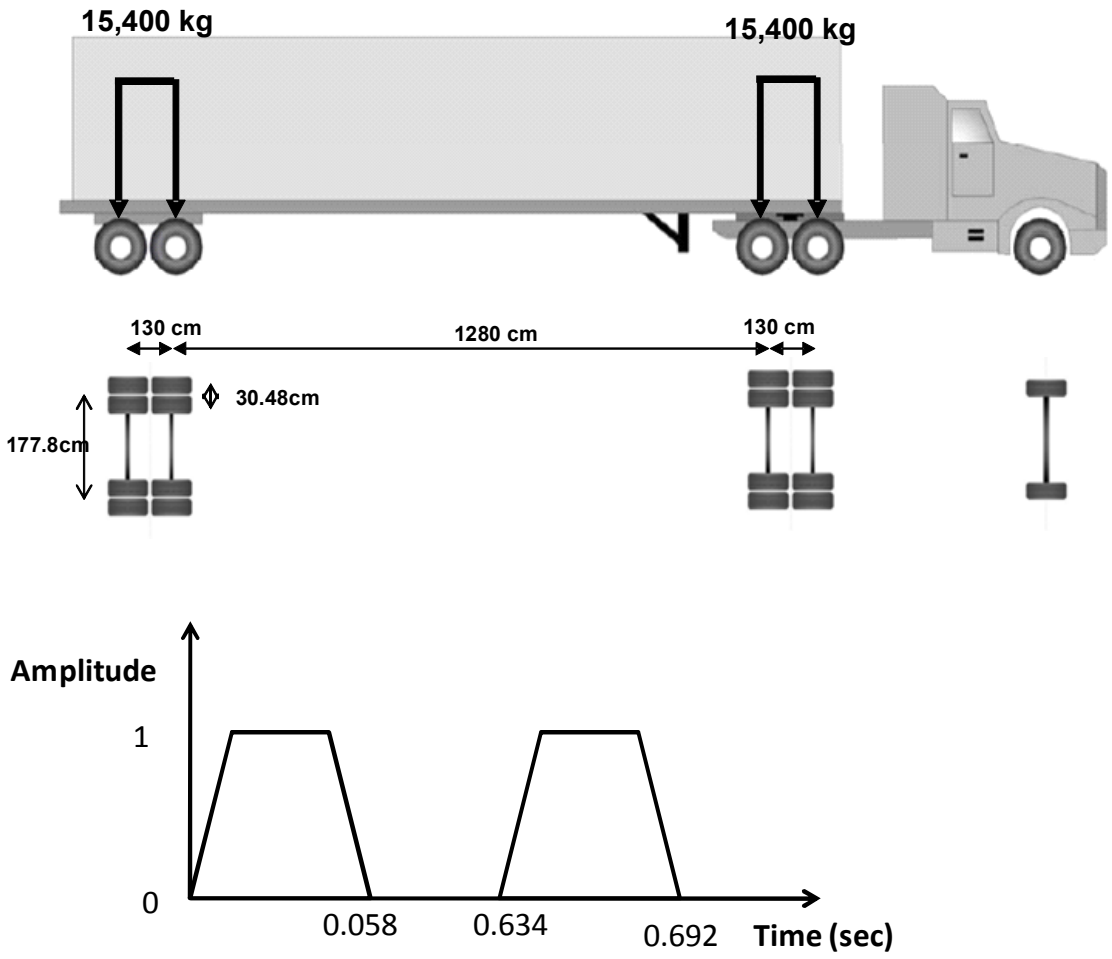

Figure 5-7. Truck Loading Configuration (Class 9) used in This Study

Material properties of individual layers can be found in the study (Kim et al., 2011). The underlying layers (i.e., base and subgrade) were modeled as isotropic linear elastic, while viscoelastic response was considered to describe the behavior of the asphalt concrete surface layer. The surface layer can dissipate energy due to its viscoelastic nature, which results in permanent deformation (rutting) of the layer. Different performance responses between the linear and nonlinear viscoelastic approaches can be

compared, and the resulting significance of the nonlinear viscoelastic nature of asphalt mixtures can be observed.

Figure 5-8 compares permanent deformation (rut depth) accumulated from each truck loading up to the 50 cycles. It clearly shows the increasing difference in the rut depth between the two models as the number of loading cycle increases. This is because the stress-dependent nonlinear viscoelastic parameters increase as stress level increases, as demonstrated. At the end of the 50-cycle simulation, the total rut depth predicted from the nonlinear viscoelastic case was around 500% more than the total rut depth predicted through use of the linear viscoelastic model. Clearly, three-dimensional finite element simulations of the pavement structure present significant differences between the linear viscoelastic approach and the nonlinear viscoelastic modeling in the prediction of pavement performance with respect to rutting. The differences between the two approaches are considered significant and should be addressed in the process of performance-based pavement design. This also implies the importance of proper and more realistic characterization of pavement materials.

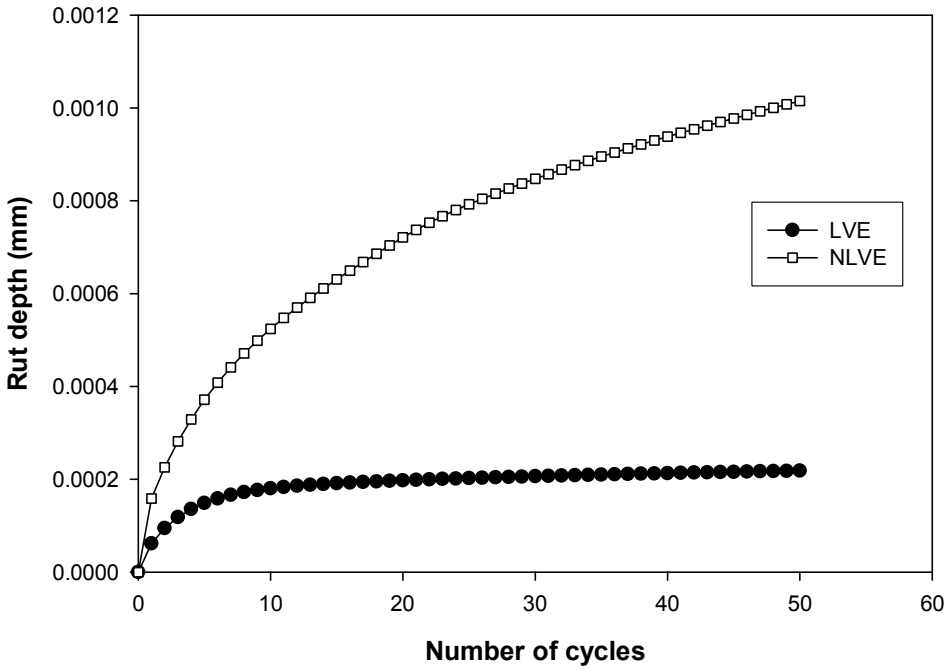

Figure 5-8. Comparison of Permanent Deformation up to 50 Loading Cycles: LVE vs. NLVE

CHAPTER 6

CHARACTERIZATION OF FRACTURE PROPERTIES

This chapter presents the fracture tests conducted for this study and testing results. Testing protocol for the SCB fracture tests using the digital image correlation system (DIC) was developed to characterize viscoelastic fracture properties at various loading rates and testing temperatures. Using test results, fracture energies were calculated based on the concept of the "critical energy release rate" for each testing condition. Also, this chapter presents cohesive zone fracture properties that were locally captured using finite element model simulations.

6.1. Test Development

Fracture tests can be used to investigate the fracture behavior of asphaltic materials. There are several fracture testing methods in the asphaltic materials and pavement mechanics community. The most popular testing methods include: the Single-edge Notched Beam (SEB) test (Mobasher et al., 1997; Hoare et al., 2000; Marasteanu et al., 2002; and Wagoner et al., 2005), the Disc-shaped Compact Tension (DCT) test (Lee et al., 1995; Wagoner et al., 2005, 2006), the Double-edged Notched Tension (DENT) test (Seo, 2003), and the Semi-circular Bend (SCB) test (Molenaar et. Al., 2002; Li and Marasteanu, 2004; Li and Marasteanu, 2006) as shown in Figure 6-1.

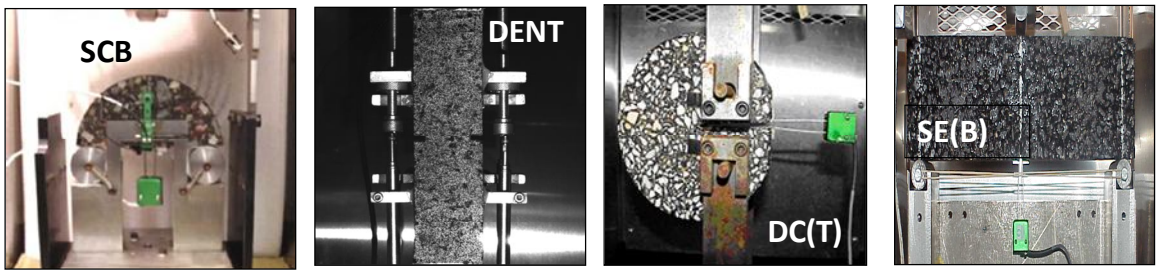

Figure 6-1. Fracture Testing Method used for Asphaltic Materials

Among the various options, SCB testing was selected in this study because it has several benefits compared to other fracture test methods. Even if it has some limitations (Wagoner et al.,2005) SCB testing is practically attractive in that it is very repeatable, simple to perform, and that multiple testing specimens can be easily prepared through a routine process of mixing and Superpave gyratory compacting of asphalt mixtures. Furthermore, the SCB geometry is even more attractive when considering mixed-mode and mode II fracture tests (Lim et al., 1994; Ayatollahi and Aliha; 2007). Based on these practical benefits, the SCB testing configuration has become a popular geometry for evaluating the fracture behavior of bituminous mixtures.

6.1.1 Specimen preparation.

Figure 6-2 briefly demonstrates the specimen production process using the Superpave gyratory compactor and saw machines. The Superpave gyratory compactor was used to produce tall compacted samples 150 mm in diameter and 175 mm in height. Then, five slices (each with a diameter of 150 mm and a height of 25 mm) were obtained by removing the top and bottom parts of the tall sample. Finally, the slice was cut into

two identical halves and then the saw machine was used to make the vertical and inclined notch with 25 mm in length and 2.5 mm in width.

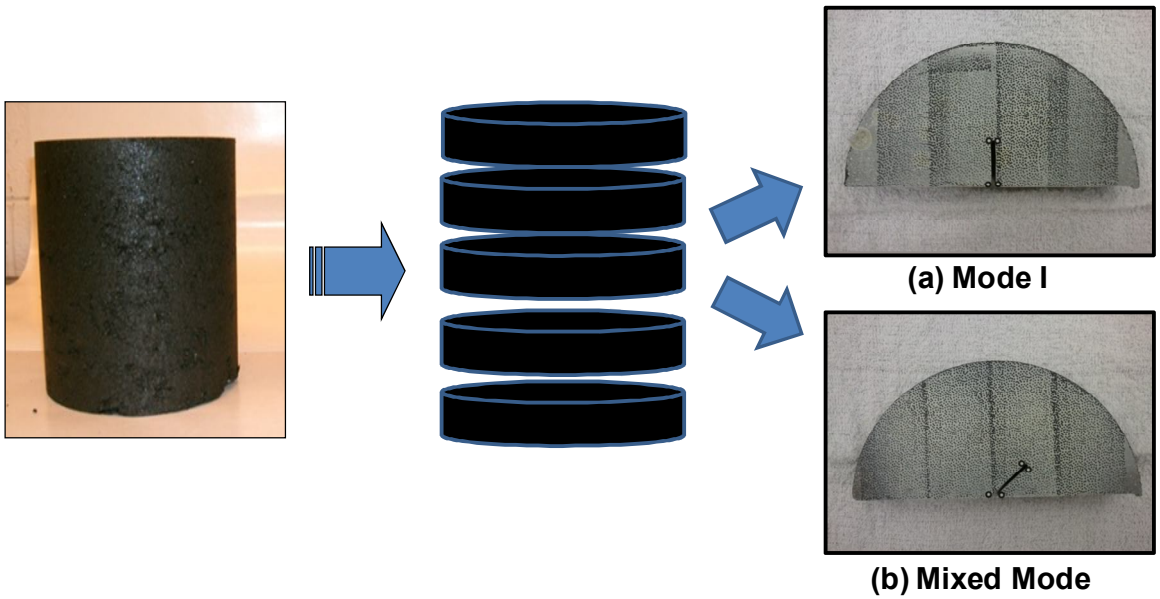

Figure 6-2. Pictures of SCB Specimen Production Process

6.1.2 Data collection and equipment.

In this study, the DIC system was incorporated with the SCB fracture test to characterize fracture properties and investigate the fracture behavior of asphaltic materials. The DIC recognizes the surface structure of the specimen in digital video images and allocates coordinates to the image pixels. The first image represents the undeformed state, and further images are recorded during the deformation of the specimen. Then, the DIC compares the digital images and calculates the displacement and deformation of the specimen. In order to facilitate the DIC process more efficiently, the specimen was painted with black and white spray until a clear contrast between the white background and numerous black dots (creating an image pattern) was achieved. A

number of black dots were used as material points for the full-field deformation characteristics such as formation and movement of the FPZ as cracks grew due to loading. Two pairs of dot gauges were additionally attached to the surface of the specimen to more accurately capture the displacements at the mouth (denoted as notch mouth opening displacements, NMOD) and at the tip (denoted as notch tip opening displacements, NTOD) of the initial notch. A clip-on gauge was also used to capture the NMOD to compare measurements from DIC. The DIC system used in this study incorporated a high-speed video camera that can accurately monitor specimen deformation in strains from 0.05% up to 500%. Figure 6-3 shows the SCB testing set-up, painted black dot image pattern and the additional two-pair gauge points attached on the specimen surface for DIC analysis, and the clip-on gauge installed at the bottom of the specimen.

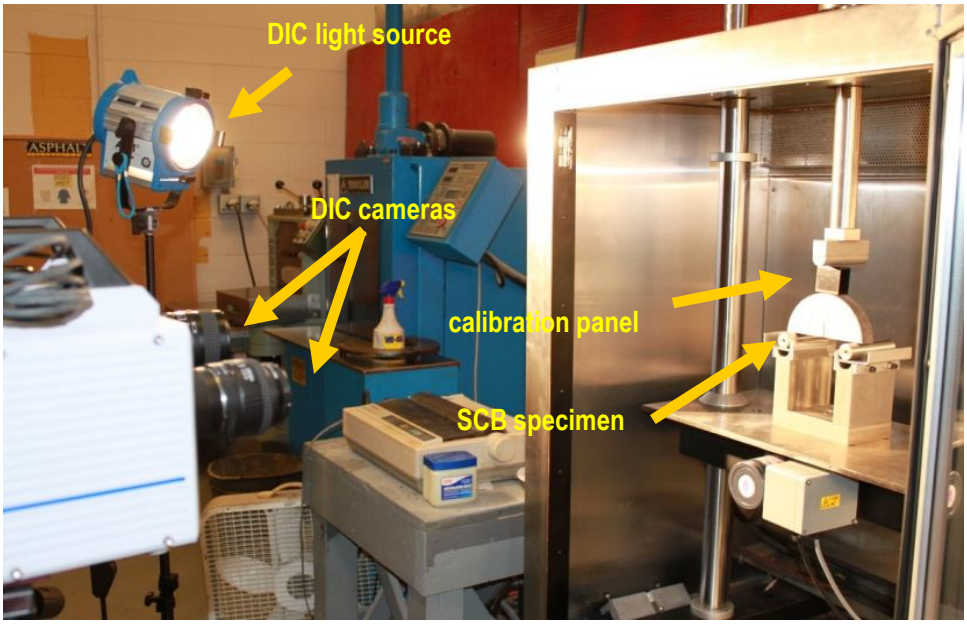

(a)

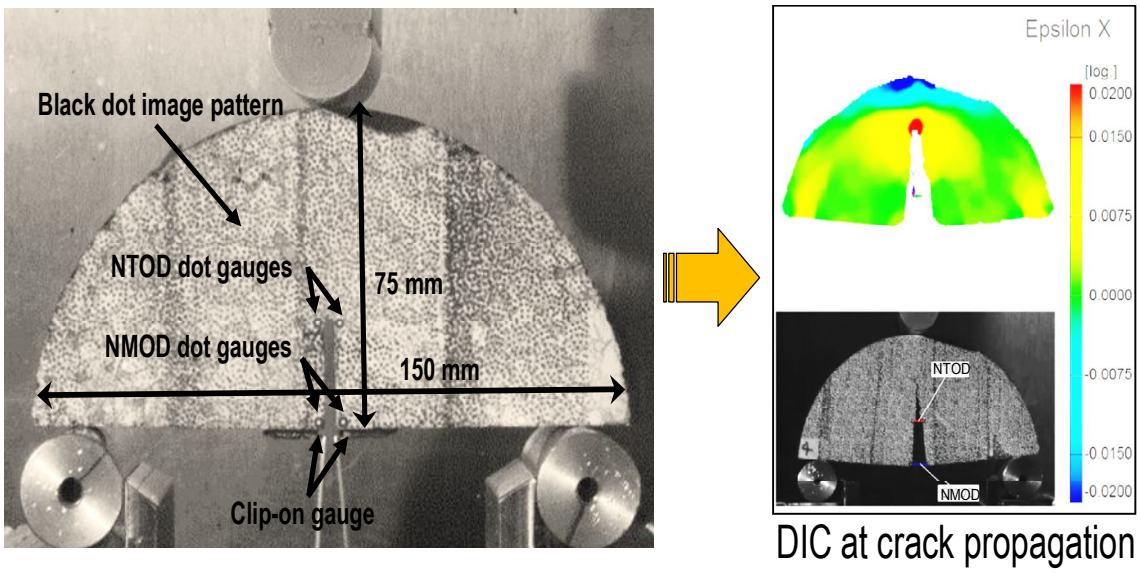

(b)

Figure 6-3. Pictures of SCB testing set-up: (a) an overview of the whole testing set-up; and (b) a closer view of a SCB specimen ready to be tested

6.2. Rate – and Temperature – Dependent Fracture Properties

In order to investigate the rate- and temperature dependent behavior of asphaltic materials, Table 6-1 presents the testing plan. A total of 48 SCB specimens from the AC mixture were prepared to complete three replicates per test case of the 16 test cases in total (four loading rates at four temperatures). Before testing, individual SCB specimens were placed inside the environmental chamber of a mechanical testing machine for temperature equilibrium targeting the four different testing temperatures (i.e., -10, 0, 21, and 30°C). Following the temperature conditioning step, specimens were subjected to a simple three-point bending configuration with four different monotonic displacement rates (i.e., 1, 5, 10, and 50 mm/min.) applied to the top center line of the SCB specimens at each testing temperature. As shown in Figure 6-3, metallic rollers separated by a

distance of 122 mm (14mm from the edges of the specimen) were used to support the specimen. Reaction force at the loading point was monitored by the data acquisition system installed in the mechanical testing machine.

Figure 6-4 exemplifies the SCB test results from a test case at 5 mm/min. and 30 °C by plotting the reaction forces at the point of load application as the opening displacements (NMOD) increased. As presented in the figures, the test results among the replicates at the same testing conditions were repeatable without large discrepancies. The coefficient of variation in the peak force from each testing case was between 2.6 % and 19.2 %.

Table 6-1. SCB Mode I Fracture Testing Plan

	AC Mixture															
Temp. (°C)	-10				0				21				30			
Rates (mm/min)	1	5	10	50	1	5	10	50	1	5	10	50	1	5	10	50
No. of Specimens	3	3	3	3	3	3	3	3	3	3	3	3	3	3	3	3

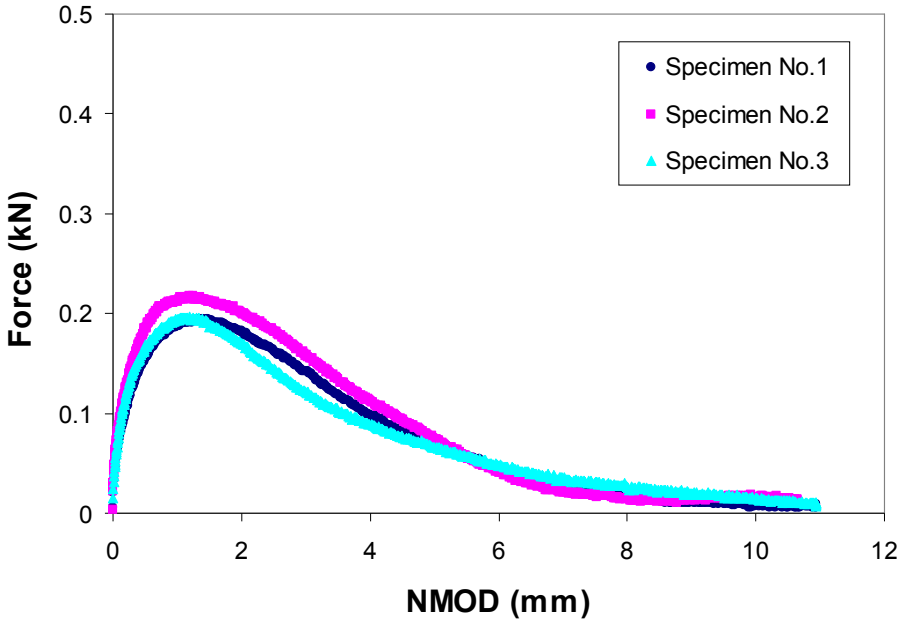

Figure 6-4. SCB Test Results (Force-NMOD) from a test case at 5 mm/min. and 30°C

In an attempt to illustrate the effects of testing conditions on the mixture's fracture behavior, Figure 6-5 presents the SCB test results by plotting the average values between the reaction forces and opening displacements at different loading rates by the different testing temperatures (i.e., 6-5(a) for -10 °C, 6-5(b) for 0 °C, 6-5(c) for 21°C, and 6-5(c) for 30 °C). As clearly seen in figures, the figures reveal the rate- and temperature-related global mechanical behavior of the AC mixture. At -10 °C, although the peak force slightly increases as the loading rate becomes higher, it appears that the fracture behavior is relatively rate-independent, which is typically observed from a linear elastic fracture state. However, the rate-dependent behavior is obvious and becomes more evident when the testing temperature is higher. Slower loading speeds produce more compliant responses than faster cases. Loading rates clearly affect both the peak force and the material softening, which is represented by the shape of the post-peak tailing. The trends

presented in figures suggest that the rate- and temperature-dependent nature of the fracture characteristics needs to be considered when modeling the mechanical performance of typical asphaltic materials and pavements with which a wide range of strain rates and service temperatures is usually associated.

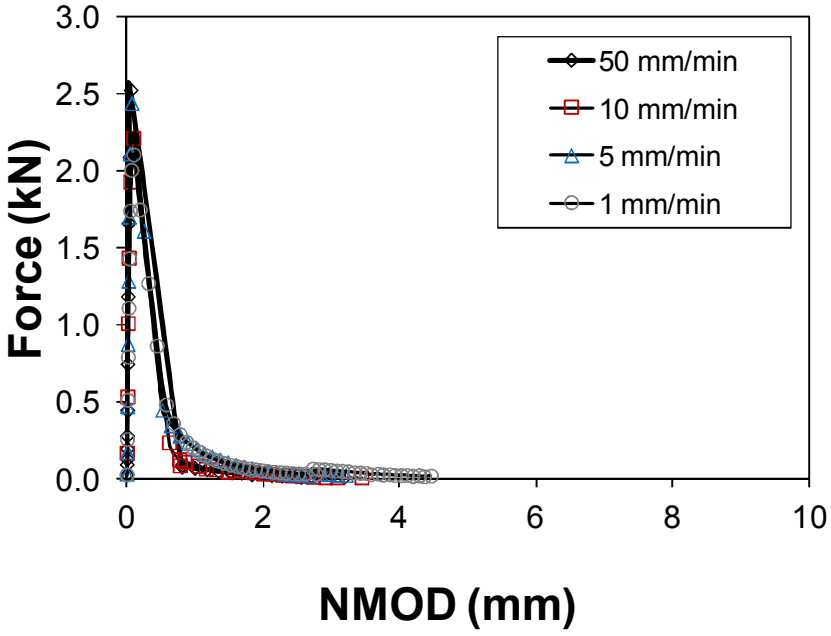

(a) at -10 °C

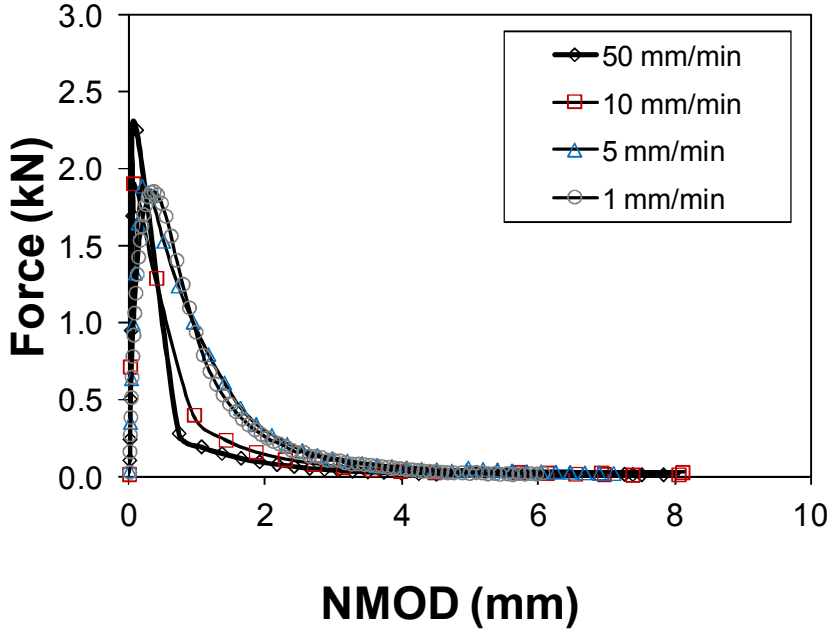

(b) at 0 °C

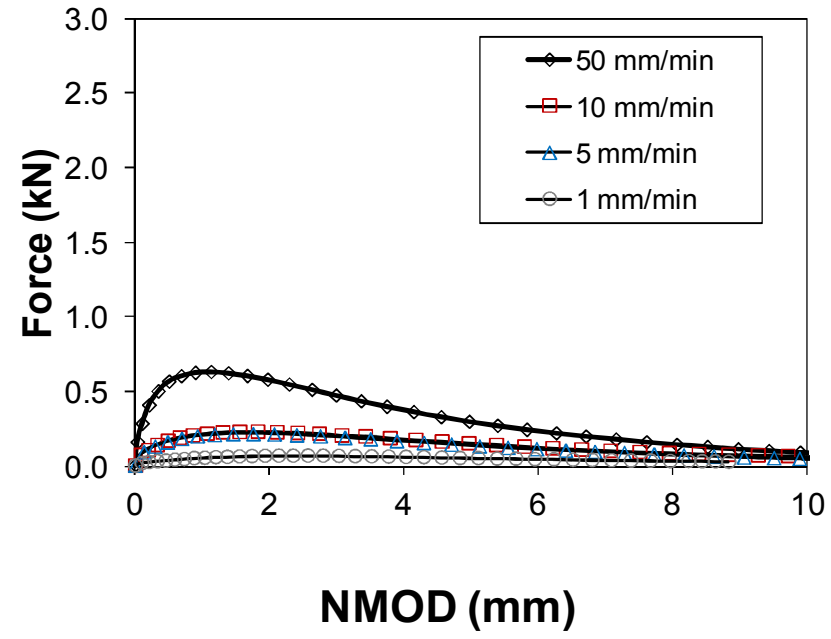

(c) at 21 °C

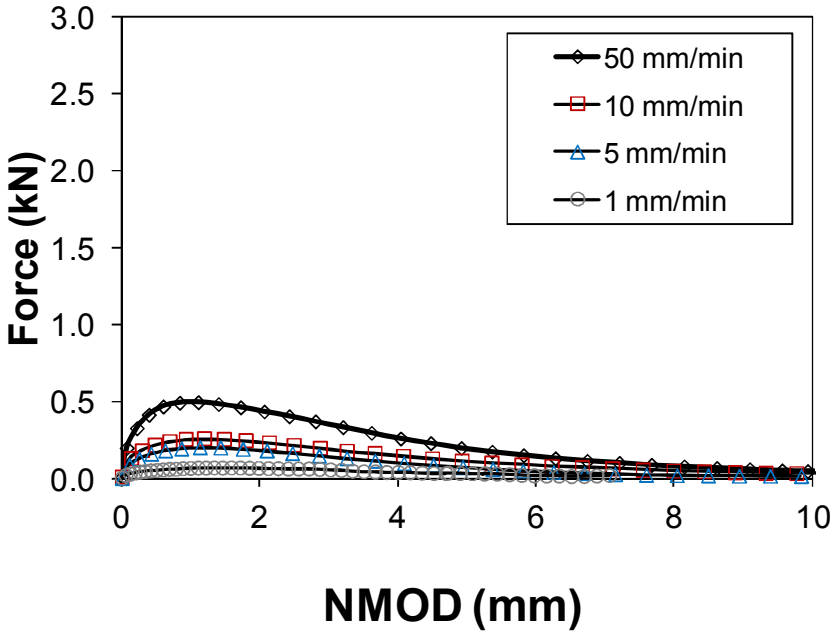

(d) at 30 °C

Figure 6-5. SCB Test Results at Different Loading Rates and Testing Temperatures

As mentioned earlier, to measure various deformation characteristics simultaneously, the DIC was incorporated in this study with two other displacements measuring methods: (i) a clip-on gauge attached to capture the NMOD and (ii) crosshead displacements to provide vertical LPD. This is to evaluate any differences and/or compatibility between the two strain-measuring approaches: the conventional gauge method and the DIC technique. Furthermore, as discussed in the later section; fracture energy characterization; fracture energy can be estimated by several different measurements and analysis approaches. Any similarities and/or compatibility between different fracture energy values estimated from different measurements and approaches can be examined.

Figure 6-6 shows the force-displacement curves of specimen No. 3 in Figure 6-4. It plots the opening displacements measured from the DIC (i.e., NMOD-DIC and NTOD-DIC), opening displacements captured by the clip-on gauge (i.e., NMOD-COG), and load point displacements measured by the DIC (i.e., LPD-DIC) and cross-head (i.e., LPD-CH). As shown, the DIC results agree well with these measurements. From the result, it can be inferred that DIC measurements (both NMOD-DIC and LPD-DIC) are quite compatible with measurements obtained from the clip-on gauge (NMOD-COG) and the cross-head (LPD-CH) throughout the SCB fracture test. This seems to be an attractive finding for practical reasons, since the DIC process is time-consuming, expensive, and requires additional techniques for data analysis compared to the use of the conventional displacement measuring systems. In contrast, it is also obvious that DIC is preferred to investigate the deformation characteristics of time-dependent, heterogeneous media such as asphalt mixtures, because it is versatile in terms of providing detailed information on

both full-field surface displacements and local material behavior. This feature is particularly important for fracture investigation, because fracture is local behavior that needs to be characterized with local measurements such as the NTOD.

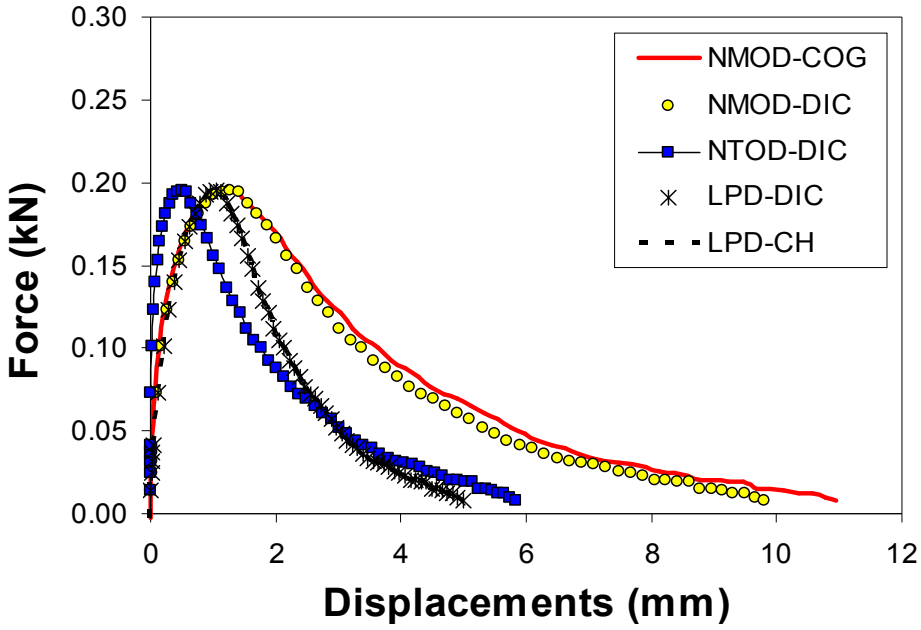

Figure 6-6. Force vs. Displacements Measured using Different Methods

Figure 6-7 presents visual observation of SCB specimens after testing at the three different temperatures. The cracking pattern is presented in Figure 6-7 (a), and the fracture surfaces of individual specimens are shown in Figure 6-7 (b). It appears that cracks propagated straight from the crack tip and travelled through aggregates at low temperatures, while the crack trajectory was significantly affected by the mixture microstructure ambient temperatures (21 ºC and 30 ºC). As expected, the fracture process at ambient temperatures without moisture damage occurred within the black matrix phase,

which resulted in a deflected crack path around coarse aggregates and the black fracture surface, as demonstrated in the figure.

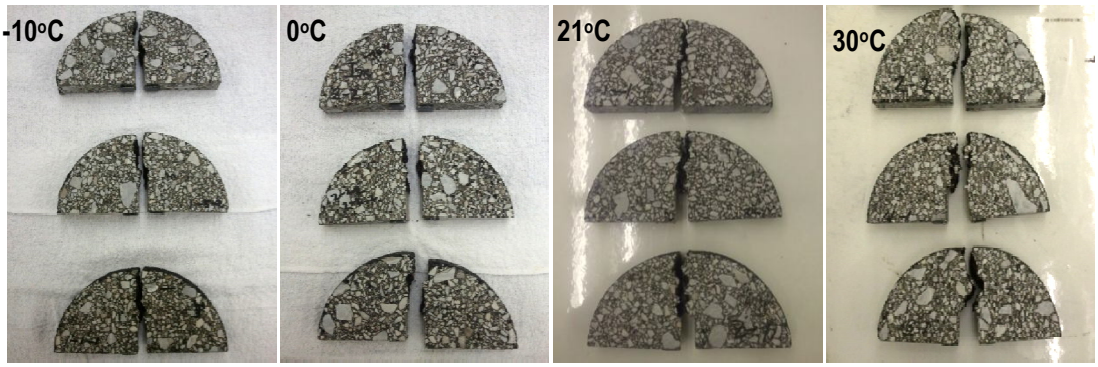

(a) Cracking pattern

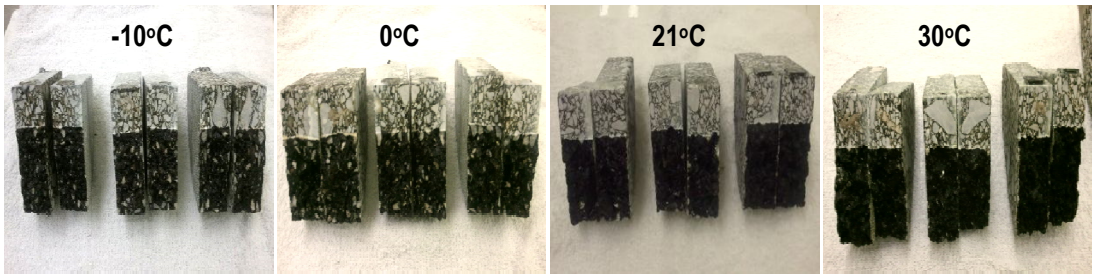

(b) Fractured surfaces

Figure 6-7. Visual Observation of SCB Specimens After Testing

6.2.1. Fracture energy characterization.

Using SCB test results, the average fracture energy was obtained for each test case. There were several methods (Song et al. 2008; Wagoner et al. 2005; Aragão 2011; Wagoner et al. 2005; Marasteanu et al. 2007) found in the open literature to calculate the fracture energy. Among them, this study attempted two approaches: one is based on the concept of the critical energy release rate and the other is by modeling the SCB fracture tests with cohesive zone elements. The first approach is relatively simple to characterize the fracture energy by merely calculating an area under the load-displacement curve

normalized by the area of the fractured surface, i.e., the initial ligament length multiplied by the specimen thickness. However, the fracture energies obtained from the first approach may mislead true fracture characteristics of the material, because the force-displacement curves are global measurements that are dependent on the choice of displacement measurements, testing specimen geometry and applied boundary conditions.

Furthermore, the viscoelastic nature of the asphaltic material creates a further complication in identifying fracture properties. Some parts of the total energy monitored by calculating the area below the force-displacement curves are related to the energy dissipated due to material viscoelasticity. Fracture characteristics along the fracture process zone should be examined locally, not by the global force-displacement test results. Based on this fact, the second approach, finite element simulations of the SCB tests with cohesive zone model, was conducted to determine the fracture properties that are locally associated to initiate and propagate cracks through the specimens.

6.2.2. Fracture energy from force-displacement curve.

For comparison purposes, the fracture energy was calculated using the five different sets of load-displacement data: force-NMOD-DIC, force-NTOD-DIC, force-LPD-DIC, force-NMOD-COG, and force-LPD-CH. Table 6-2 summarizes the average fracture energy and its sample-to-sample variation, which is represented by the coefficient of variation (COV), of each test case from the five different displacement measurements.

Table 6-2. Summary of Average Fracture Energy (J/m^2) and COV (%)

Temp. (°C)	Rates (mm /min.)	From Clip-on gage		From Crosshead		From DIC					
		Force-NMOD		Force-LPD		Force-NTOD		Force-NMOD		Force-LPD	
		Mean (J/m^2)	COV (%)	Mean (J/m^2)	COV (%)	Mean (J/m^2)	COV (%)	Mean (J/m^2)	COV (%)	Mean (J/m^2)	COV (%)
-10	1	787.1	25.6	453.5	26.4	DIC was not used.					
	5	808.6	2.8	406.8	19.6	564.8	0.5	813.2	0.8	390.7	0.1
	10	767.0	15.3	393.2	26.2	DIC was not used.					
	50	770.7	16.7	370.7	7.3	DIC was not used.					
0	1	1750.2	15.6	1076.7	12.0	DIC was not used.					
	5	1789.4	30.8	1080.5	30.2	1117.2	32.4	1779.2	34.0	N/A	
	10	1169.4	5.4	690.4	7.3	DIC was not used.					
	50	980.4	8.1	531.4	4.4	DIC was not used.					
21	1	395.9	17.4	186.2	16.6	240.7	25.4	413.1	24.6	190.5	20.3
	5	1082.2	11.1	539.5	9.2	551.8	7.7	1043.1	14.5	525.5	11.3
	10	1200.6	8.4	636.4	10.6	555.6	10.1	1112.0	1.5	618.3	5.0
	50	2670.5	4.1	1462.3	4.0	1468.4	6.7	2624.1	2.4	1421.5	2.8
30	1	216.6	13.3	111.8	15.5	114.0	15.9	209.6	14.4	113.4	18.4
	5	664.5	4.8	335.4	4.0	379.1	10.3	651.1	5.7	357.3	4.0
	10	1025.7	19.5	536.4	20.2	574.7	26.4	1021.8	21.6	521.6	13.5
	50	1851.3	11.8	967.9	17.0	1081.3	13.8	1798.5	15.8	927.0	14.6

Most test cases showed low COV values, usually less than 20 %, from three replicates; exceptions were some cases where relatively high COV values up to 30 % were determined. The COV values obtained in this study were in a similar range, between 15 % and 34 %, to those found in a recent study that investigated the low-temperature fracture characteristics of asphalt concrete mixtures using the SCB geometry (Marasteanu et al. 2007).

As exemplified in Figure 6-6 and Table 6-2 confirms, fracture energies obtained from DIC data (NMOD-DIC and LPD-DIC) are very similar to the fracture energies estimated respectively by the clip-on gauge measurements (NMOD-COG) and the cross-head displacements (LPD-CH), regardless of loading rates and testing temperatures.

Moreover, as previously observed in Figure 6-6, the fracture energy values obtained from force-NMOD curves were always greater than those from the force-NTOD curves. This is because the tip opening displacements are naturally smaller than the mouth opening displacements when the specimen is subjected to a bending mode fracture such as SCB. Since the fracture process is locally initiated at the notch tip, the fracture energy characterized using NTOD data is more representative than the value obtained from the NMOD measurements. The fracture energy estimated from NMOD data clearly overestimates the true material fracture toughness, and the deviation in the fracture energy between the NTOD and NMOD measurements becomes greater as temperature increases. At -10 ^{o}C, the fracture energy from force-NTOD curves was about 30 % less than that from force-NMOD curves, while the level of deviation increased to 37 % at 0 ^{o}C and up to 50 % at 21 ^{o}C and 30 ^{o}C depending on the loading rate. A similar finding was also observed in other studies (Song et al. 2008; Aragão 2011). This clearly indicates that, although it has been widely adopted due to its simple and practical aspects, the use of NMOD measurements in the fracture characterization of asphaltic materials needs great care and is even more cautious at elevated temperatures when the materials present several sources of energy dissipation such as material viscoelasticity/plasticity and crack growth.

Another interesting observation from the table is that average fracture energies calculated from the LPD data are smaller than, but similar to the fracture energy values estimated from the NTOD data, although the LPD measurements have nothing to do with the local fracture process. This seems to be an attractive observation for practical purposes, since the LPD measurements from the SCB test are easy to take by simply

monitoring vertical displacements (for instance the cross-head movements), whereas the NTOD data are relatively hard to obtain because it needs special measuring devices such as the video cameras and DIC system as pursued in this study.

6.2.3. Fracture energy from finite element modeling with cohesive zone.

The FPZ is a nonlinear zone characterized by progressive softening, for which the stress decreases at increasing deformation. The nonlinear softening zone is surrounded by a non-softening nonlinear zone, which represents material inelasticity. Bazant and Planas (1998) skillfully classified the fracture process behavior in certain materials into three types: brittle, ductile, and quasi-brittle. Each type presents different relative sizes of those two nonlinear zones (i.e., softening and non-softening nonlinear zones). Figure 6-8 presents the third type of behavior, so-called quasi-brittle fracture. It includes situations in which a major part of the nonlinear zone undergoes progressive damage with material softening due to microcracking, void formation, interface breakages, frictional slips, and others. The softening zone is then surrounded by the inelastic material yielding zone, which is much smaller than the softening zone. This behavior includes a relatively large FPZ, as shown in the figure. Asphaltic paving mixtures are usually classified as quasi-brittle materials (Bazant and Planas 1998; Duan et al. 2006; Kim et al. 2008).

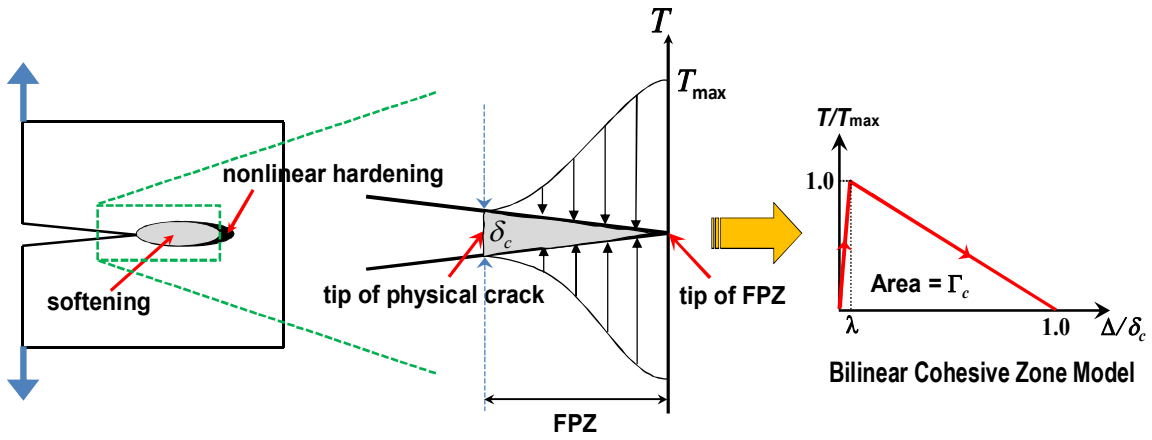

Figure 6-8. Schematic Illustration of FPZ of Typical Quasi-brittle Materials

The FPZ can be modeled in many different ways, and one of the well-known approaches is to use a cohesive zone. At the crack tip, the cohesive zone constitutive behavior reflects the change in the cohesive zone material properties due to microscopic damage accumulation ahead of the crack tip. This behavior can be expressed by the general traction-displacement cohesive zone relationship as follows:

$$T_i(x_m,t) = T_i\{\Delta_i(x_m,\tau)\} \qquad [6.1]$$

where T_i = cohesive zone traction (T_n for normal and T_t for tangential traction),

Δ_i = cohesive zone displacement (Δ_n for normal and Δ_t for tangential displacement),

x_m = spatial coordinates, and

t = time of interest.

Cohesive zone models regard fracture as a gradual phenomenon in which separation (Δ) takes place across an extended crack tip (or cohesive zone) and where fracture is resisted by cohesive tractions (T). The cohesive zone effectively describes the material resistance when material elements are being displaced. Equations relating normal and tangential displacement jumps across the cohesive surfaces with the proper tractions define a cohesive zone model. Among numerous cohesive zone models developed for different specific purposes, this study used an intrinsic bilinear cohesive zone model (Song et al. 2006; Geubelle and Baylor 1998; Espinosa and Zavattieri 2003). As shown in Figure 6-8, the model assumes that there is a recoverable linear elastic behavior until the traction (T) reaches a peak value, or cohesive strength ($T_{\max}$) at a corresponding separation in the traction-separation curve. At that point, a non-dimensional displacement (λ) can be identified and used to adjust the initial slope in the recoverable linear elastic part of the cohesive law. This capability of the bilinear model to adjust the initial slope is significant because it can alleviate the artificial compliance inherent to intrinsic cohesive zone models. The λ value has been determined through a convergence study designed to find a sufficiently small value to guarantee a level of initial stiffness that renders insignificant artificial compliance of the cohesive zone model. It was observed that a numerical convergence can be met when the effective displacement is smaller than 0.0005, which has been used for simulations in this study. Upon damage initiation, T varies from $T_{\max}$ to 0, when a critical displacement (δ_c) is reached and the faces of the cohesive element are fully and irreversibly separated. The cohesive zone fracture energy (Γ_c), which is the locally estimated fracture toughness, can then be calculated by computing the area below the bilinear traction-separation curve

with peak traction ($T_{\max}$) and critical displacement (δ_c) as follows:

$$\Gamma_c = \frac{1}{2}\delta_c T_{\max} \qquad [6.2]$$

Figure 6-9 presents a finite element mesh which was finally chosen after conducting a mesh convergence study. The specimen was discretized using two-dimensional, three-node triangular linear prism elements for the bulk specimen and zero-thickness cohesive zone elements were inserted along the center of the mesh to permit mode I crack growth in the simulation of SCB testing. The Prony series parameters (shown in Table 4-1) determined from the uniaxial compressive cyclic tests were used for the viscoelastic elements, and the bilinear cohesive zone model illustrated in Figure 6-8 was used to simulate fracture in the middle of the SCB specimen as the opening displacements increased. It should be noted that the simulation conducted herein involves several limitations at this stage by assuming the mixture as homogeneous and isotropic with only mode I crack growth, which may not represent the true fracture process of specimens particularly tested at the ambient temperatures where mixture heterogeneity (i.e., microstructural characteristics) and mixed-mode fracture is not trivial as demonstrated in Figure 6-7.

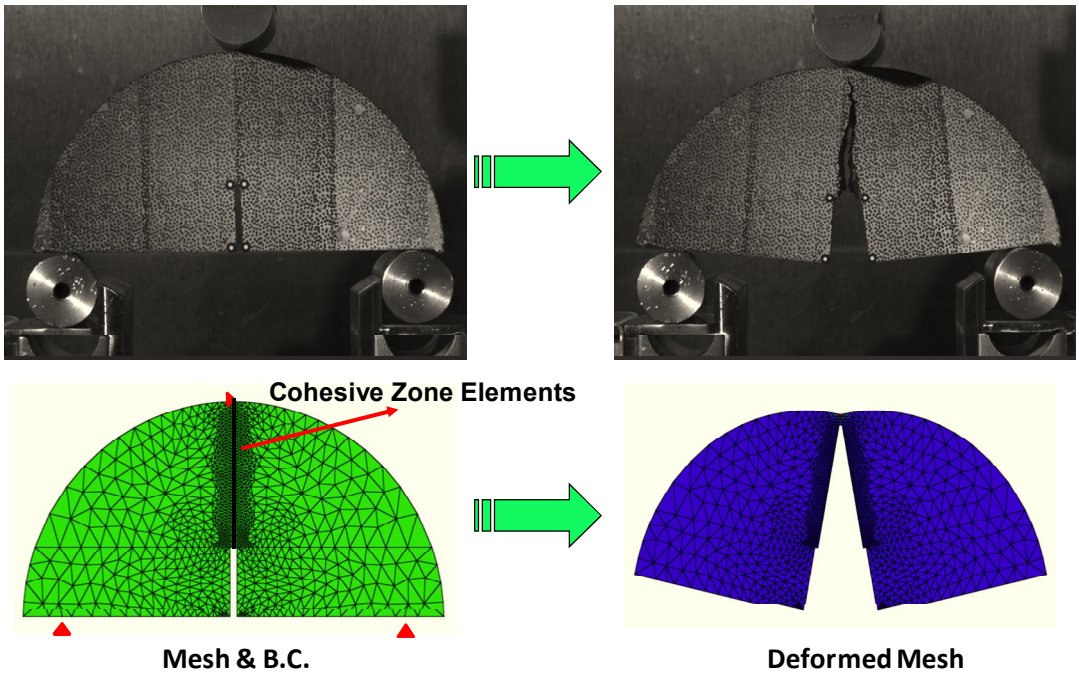

Figure 6-9. A Finite Element Mesh Constructed after Convergence Study to Model the SCB Testing

The cohesive zone fracture properties (two independent values of the three: T_{max}, δ_c, and Γ_c) in the bilinear model were determined for each case through the calibration process until a good match between test results and numerical simulations was observed. Figure 6-10 presents a strong agreement between the test results (average of the three SCB specimens) and finite element simulations. Resulting fracture properties (T_{max} and Γ_c) at each different loading rate and testing temperature are presented in Table 6-3. The good agreement between tests and model simulations indicates that the local fracture properties were properly defined through the integrated experimental-numerical approach.

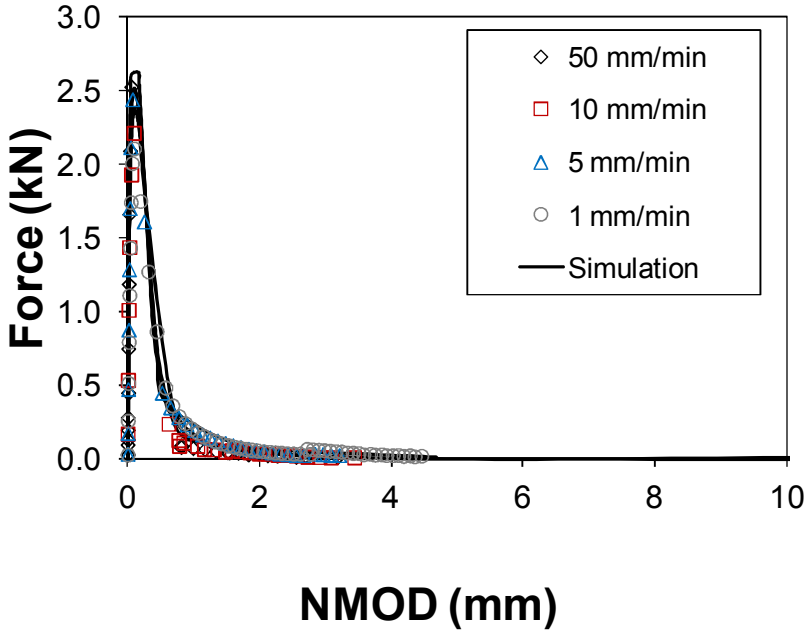

(a) at -10 °C

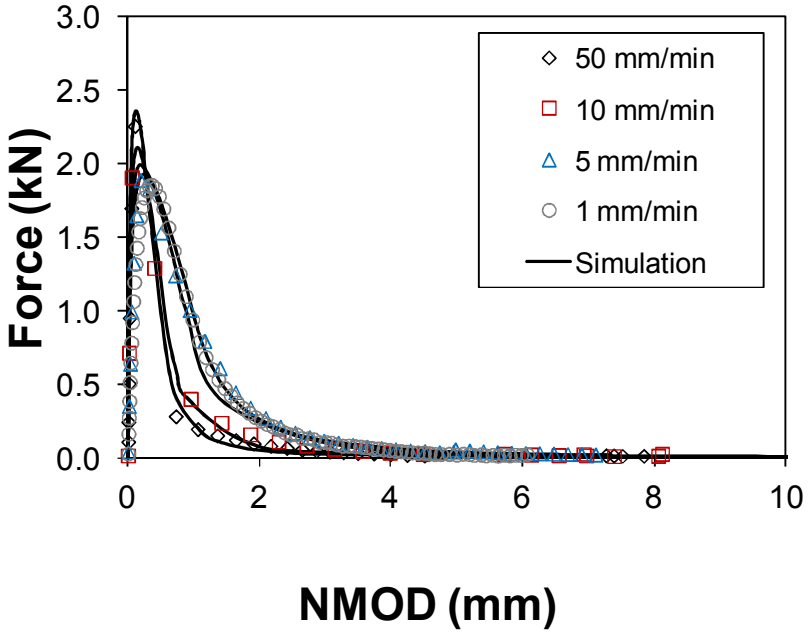

(b) at 0 °C

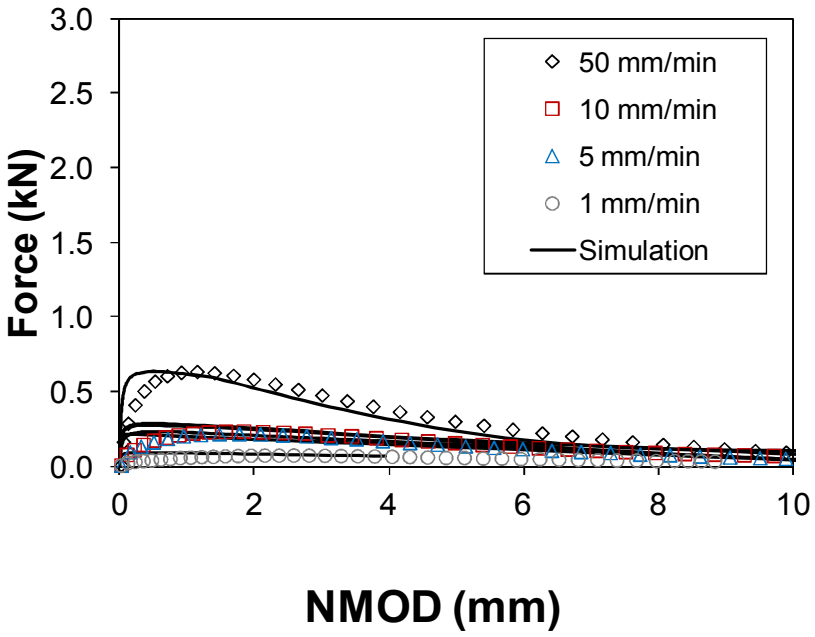

(c) at 21 °C

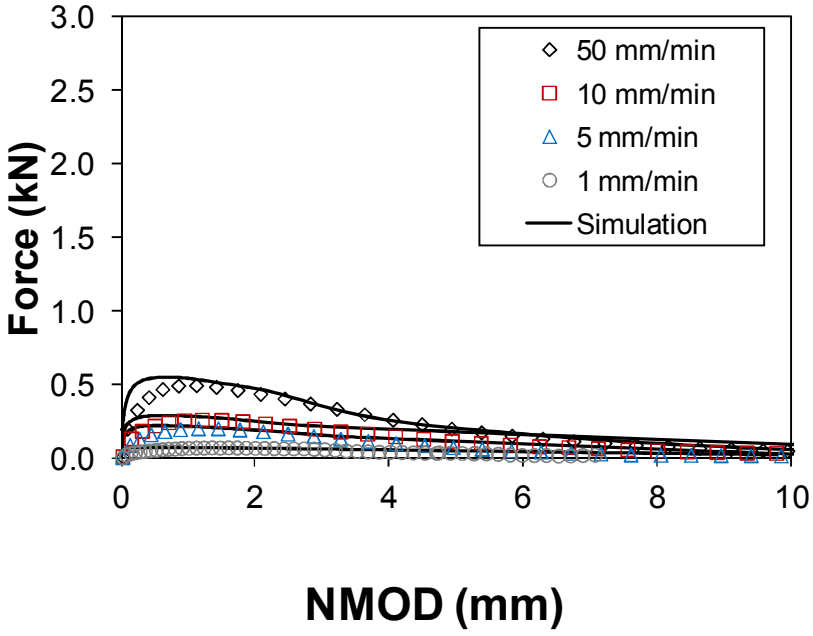

(d) at 30 °C

Figure 6-10. SCB Test Results vs. Cohesive Zone Model Simulation Results

Table 6-3. Cohesive Zone Fracture Parameters Determined

Temperature (°C)	Loading Rate (mm/min.)	Cohesive Zone Fracture Parameters	
		T_{max} (kPa)	Γ_c (J/m^2)
-10	1	3.2E+03	350
	5	3.4E+03	350
	10	3.6E+03	350
	50	4.0E+03	350
0	1	2.7E+03	750
	5	2.7E+03	700
	10	3.2E+03	450
	50	3.6E+03	400
21	1	9.0E+01	250
	5	2.5E+02	500
	10	3.0E+02	700
	50	7.0E+02	1200
30	1	8.0E+01	220
	5	2.5E+02	400
	10	3.2E+02	550
	50	6.5E+02	900

6.2.4. Discussion of test-analysis results.

In an attempt to further investigate the fracture characteristics of asphalt mixtures when they are subjected to different loading rates, different temperatures, and analysis methods, Figure 6-11 was produced using fracture energy values from the force-NMOD-COG curves, force-NTOD-DIC curves, and cohesive zone modeling at different loading rates and temperatures. The fracture energy obtained at -10 °C does not seem to be affected by the loading rate, while the fracture energies at 0 °C to 30 °C clearly change as the loading rates vary. The negligible rate-dependency at -10 °C is considered reasonable because the mixture at low temperature conditions such as -10 °C is in the linear elastic fracture domain, where the rate-dependent fracture characteristics of viscoelastic materials usually disappear. As temperature increases to 0 °C, the mixture becomes viscoelastic so that it can dissipate more energy to fracture. Therefore, the magnitude of

fracture energy at 0 ^{o}C is greater than the fracture energy at -10 ^{o}C over all the loading rates applied in this study. Regarding the trend of fracture energy to the loading rate, it decreases as the loading speed is faster, which agrees with observations in other studies (Wagoner et al. 2005; Marasteanu et al. 2007). At ambient temperatures (21 ^{o}C and 30 ^{o}C), the rate-dependent fracture behavior is obvious, and the fracture energy increases as the loading rates become higher. The trend is in accordance with what has been reported in several studies that have attempted to characterize the rate-related fracture behavior of adhesive and polymeric materials (Rahul-Kumar et al. 1999; Nguyen et al. 2004; Marzi et al. 2009). In those studies, fracture energy tends to be constant when cracks propagate at lower speeds, while it increases with crack velocity for an intermediate level of crack velocity.

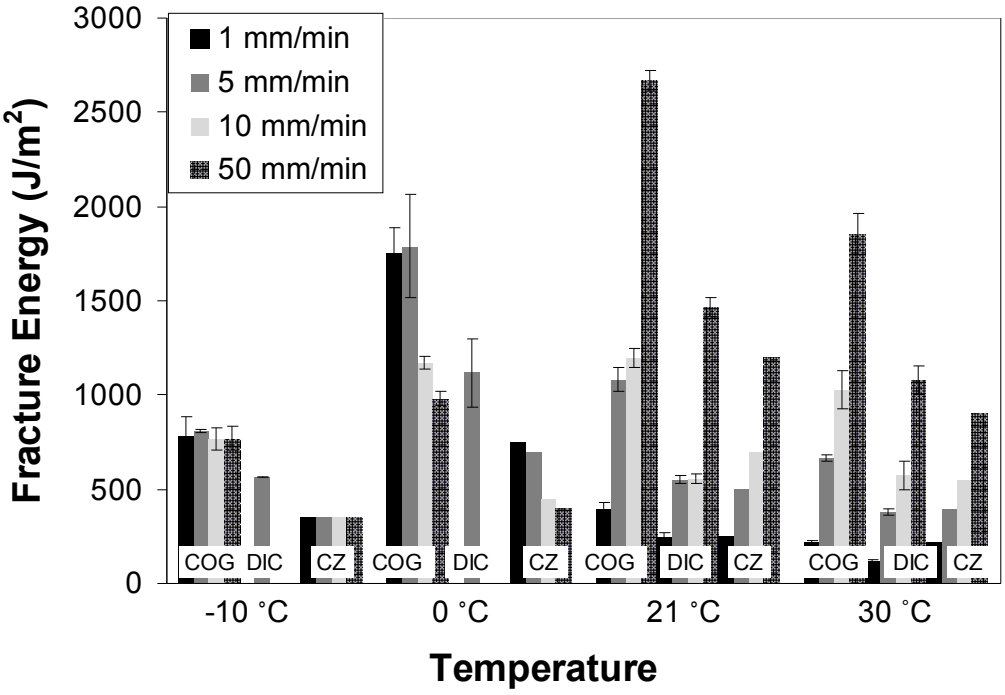

Figure 6-11. Comparison of Fracture Energies

Regarding the fracture characteristics by different approaches, Figure 6-11 shows that the fracture energies obtained from the area under the force-NMOD (or force-NTOD) curve are always larger than the fracture energy identified from the cohesive zone modeling, and the deviation between the two approaches usually decreases as the loading rates are higher. Furthermore, it is clear that fracture energy values obtained from the force-NTOD curve are closer to the values characterized at the local FPZ through the cohesive zone modeling than those obtained from the force-NMOD curve. This observation was expected since, as noted previously, the energy obtained from NMOD measurements overestimates the true fracture toughness.

6.3. Mixed-mode Fracture Properties

In contrast to mode I testing, mixed-mode fracture testing of asphaltic materials has not yet been attempted or developed. Lim et al. (1993, 1994) examined the appropriate SCB geometry, calculating stress intensity based on LEFM, to study mode II behavior. They reported that the SCB geometries for pure mode II have a span ratio (s/r) of 0.5 and a normalized notch length (a/r) of 0.35±0.04 with an α at less than 60°. Ayatollahi and Aliha (2007) also investigated the SCB geometries that represent the mixed-mode as well as pure mode II. Table 6-4 summarizes the maximum span ratio findings for a given crack length ratio that can provide pure mode II with an α at less than 60°.

Table 6-4. Maximum Allowable Range of a/r and s/r for Pure Mode II (Ayatollahi and Aliha, 2007)

a/r	0.3	0.4	0.5	0.6
s/r	≤ 0.47	≤ 0.565	≤ 0.65	≤ 0.725

Based on these findings, in this study, a span ratio of 0.4 and a normalized notch length of 0.33 with α = 45° and 50° were selected to prove the pure mode II fracture condition for the asphaltic materials. The mixed-mode was achieved by changing the span ratio to 0.5, 0.6, and 0.8. Furthermore, Lim et al. (1994) pointed out that the specimen thickness had no significant effect on the fracture toughness of various rocks. Therefore, it seems reasonable to assume that the specimen thickness will not affect the measured mixed-mode fracture properties.

6.3.1. Specimen preparation and testing set-up.

As shown in Figure 6-12, SCB specimens including inclined notches were prepared to investigate the mixed-mode behavior of asphaltic materials using the FAM mixture. The SCB specimens were then tested using a fixture designed to load the specimen to induce three-point bending, minimizing the frictional effects by allowing the support rollers to rotate and travel apart slightly when the specimen is loaded. The two supporting legs of the fixture were also designed to move freely horizontally, to adjust the different span ratios. In addition, the DIC system was incorporated to investigate the mixed-mode behaviors.

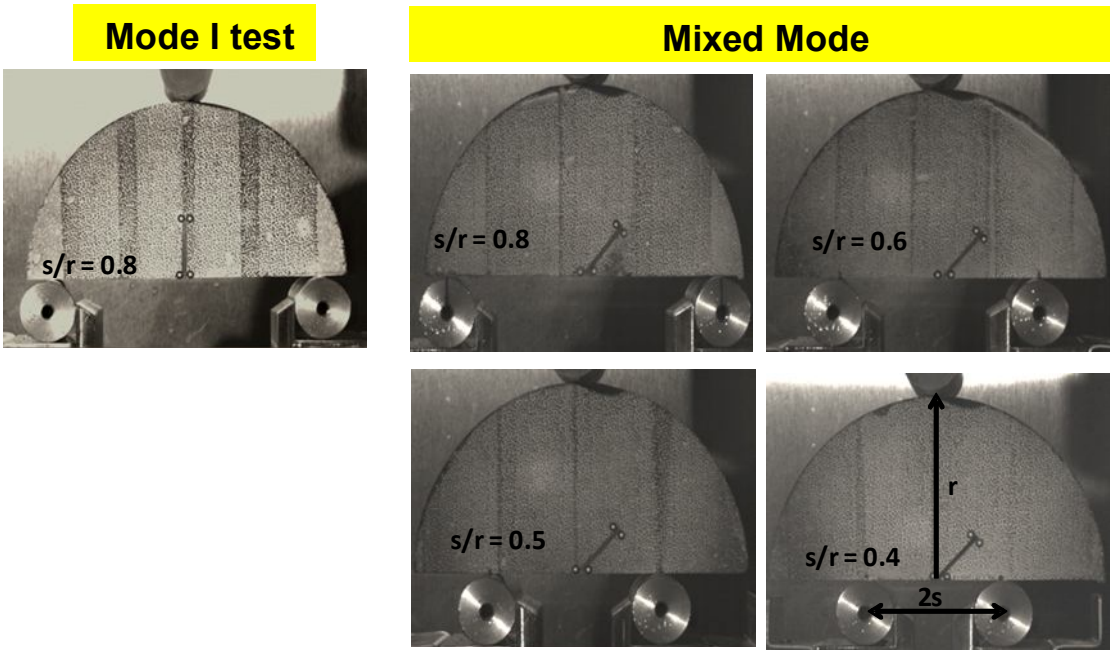

Figure 6-12. Mode I and Mixed-mode SCB Testing Configurations

6.3.2. Mixed-mode fracture testing and results.

Table 6-5 presents the testing plan. Based on the literature, two different inclined notch angles, 45° and 50°, were chosen to induce mixed-mode fracture conditions. Before testing, FAM SCB specimens were placed inside the environmental chamber of a mechanical testing machine for temperature equilibrium targeting the reference temperature of 21 °C. Following the temperature conditioning step, the specimens were subjected to a monotonic displacement rate of 10 mm/min applied to the top center line of the SCB specimens.

Table 6-5. Number of SCB Specimens used

Inclined notch angle (°)	s/r ratio				
	Mode I (0.8)	0.8	0.6	0.5	0.4
45	-	3	3	3	3
50	-	2	3	3	2
90	2	-	-	-	-

Figure 6-13 presents the test results by plotting the reaction force as the loading time increased at different loading configurations. In Figure 6-13 (a), the results of the vertical notch with the span ratio of 0.8 representing pure mode I are illustrated, and Figure 6-13 (b) shows the results of the 45^o inclined notch with various span ratios representing mixed-mode (s/r =0.4, 0.5, 0.6, and 0.8). Similarly, Figure 6-13 (c) presents the results of the 50^o inclined notch with various span ratios (i.e., s/r = 0.4, 0.5, 0.6, and 0.8). As seen in the figures, the test results among the replicates were repeatable without any significant deviations. As shown in Figure 6-13 (b) and Figure 6-13 (c), as the span ratio increased, the maximum resistance decreased, and the post-peak softened slowly because of the mixed-mode effects. Pictures of the SCB specimens after testing can be found in the appendix. These pictures show the cracking patterns for each testing condition.

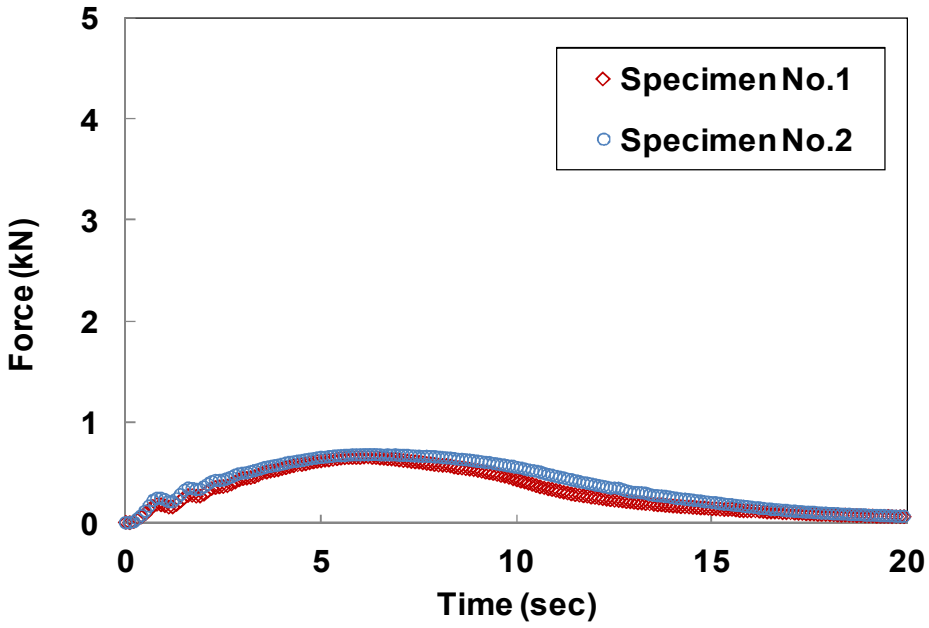
Specimen No.1
Specimen No.2
Force (kN)
Time (sec)
0
1
2
3
4
5
0
5
10
15
20

(a)

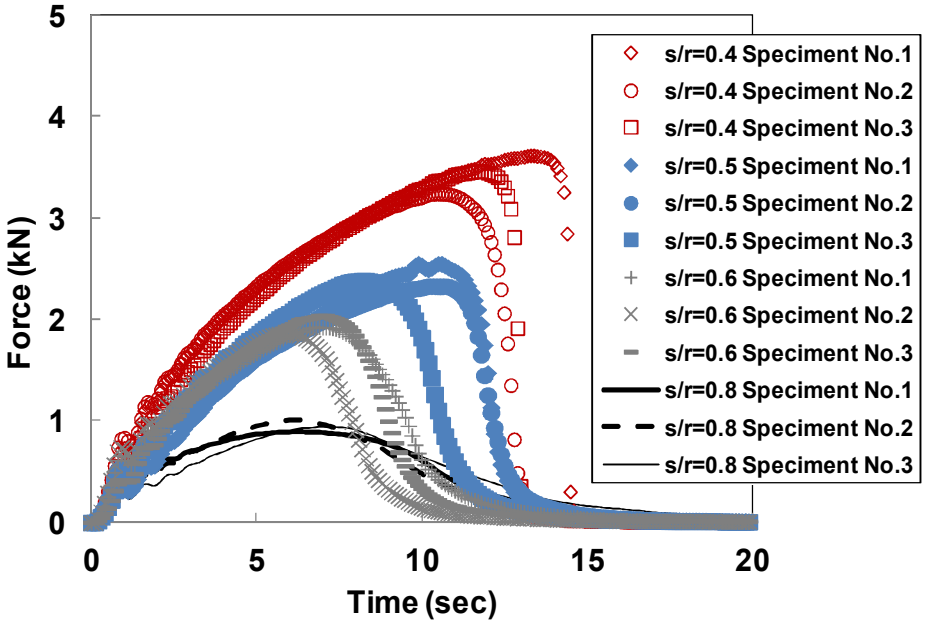
s/r=0.4 Speciment No.1
s/r=0.4 Speciment No.2
s/r=0.4 Speciment No.3
s/r=0.5 Speciment No.1
s/r=0.5 Speciment No.2
s/r=0.5 Speciment No.3
s/r=0.6 Speciment No.1
s/r=0.6 Speciment No.2
s/r=0.6 Speciment No.3
s/r=0.8 Speciment No.1
s/r=0.8 Speciment No.2
s/r=0.8 Speciment No.3
Force (kN)
Time (sec)
0
1
2
3
4
5
0
5
10
15
20

(b)

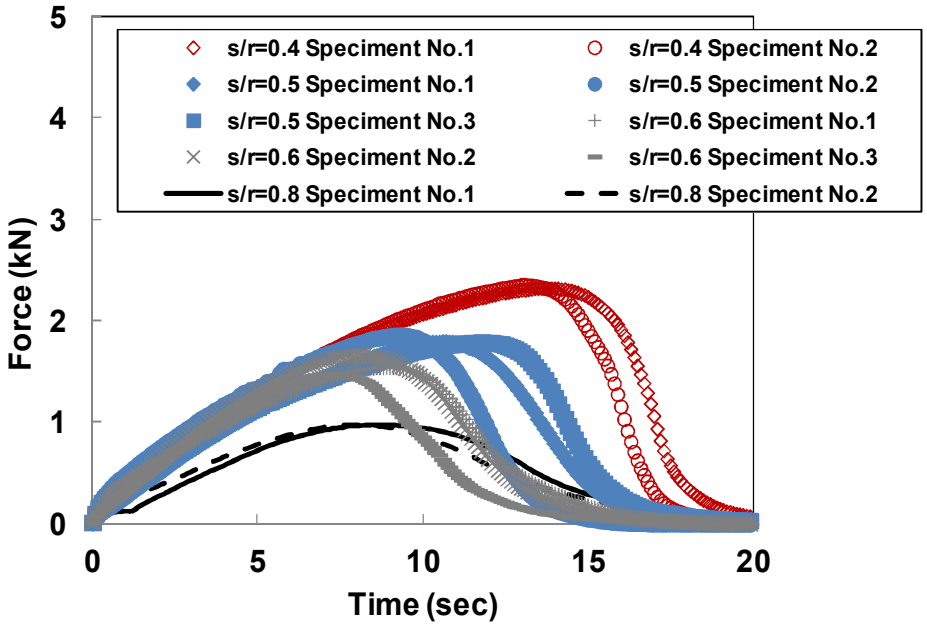

(c)

Figure 6-13. Test Results from SCB Fracture: (a) pure mode I; (b) mixed-mode with 45° inclined notch: (c) mixed-mode with 50° inclined notch

6.3.3. DIC analysis.

As previously mentioned, the SCB fracture test was performed using the DIC system. The DIC can analyze images captured at each loading stage and create any strains (i.e., ε_{xx} and ε_{yy}) and displacements. Using the DIC test results, the behavior of the mode I and mixed-mode fractures were carefully investigated at the crack tip, as shown in Figure 6-14. The strains (i.e., ε_{xx}, ε_{yy}, and ε_{xy}) were then calculated based on the displacements of each loading stage. Figure 6-15 presents the strains obtained from each testing configuration. The figures clearly show the tensile stress (in X direction in Figure 6-14 (a)) at the crack tip dominated the mode I test as expected, while a combination of stresses occurred in the mixed-mode test cases. These results imply the

mixed-mode fracture occurred due to the tensile stress (in X direction in Figure 6-14 (b)) and the shear stress (in Y direction in Figure 6-14 (b)). This confirms that the SCB testing configuration with inclined notches is appropriate for the mixed-mode loading condition in the testing geometry.

One important observation can be confirmed from these figures. As the span ratio decreased, the influence of ε_{yy} increased, and that of ε_{xx} decreased (Figure 6-15). This indicates that as the span ratio decreased, the fracture pattern showed more characteristics of mode II and fewer of mode I. Based on this result, two important fracture parameters, notch tip opening displacement (NTOD) and notch tip sliding displacement (NTSD), as shown in Figure 6-16, were defined to obtain the fracture energy of the mixed-mode testing.

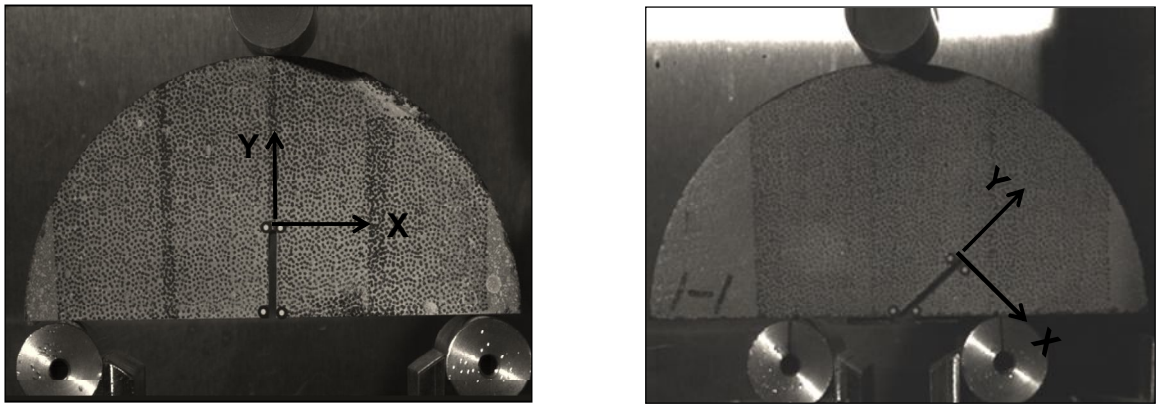

(a) Mode I (b) Mixed Mode

Figure 6-14. Strain Analysis at the Crack Tip

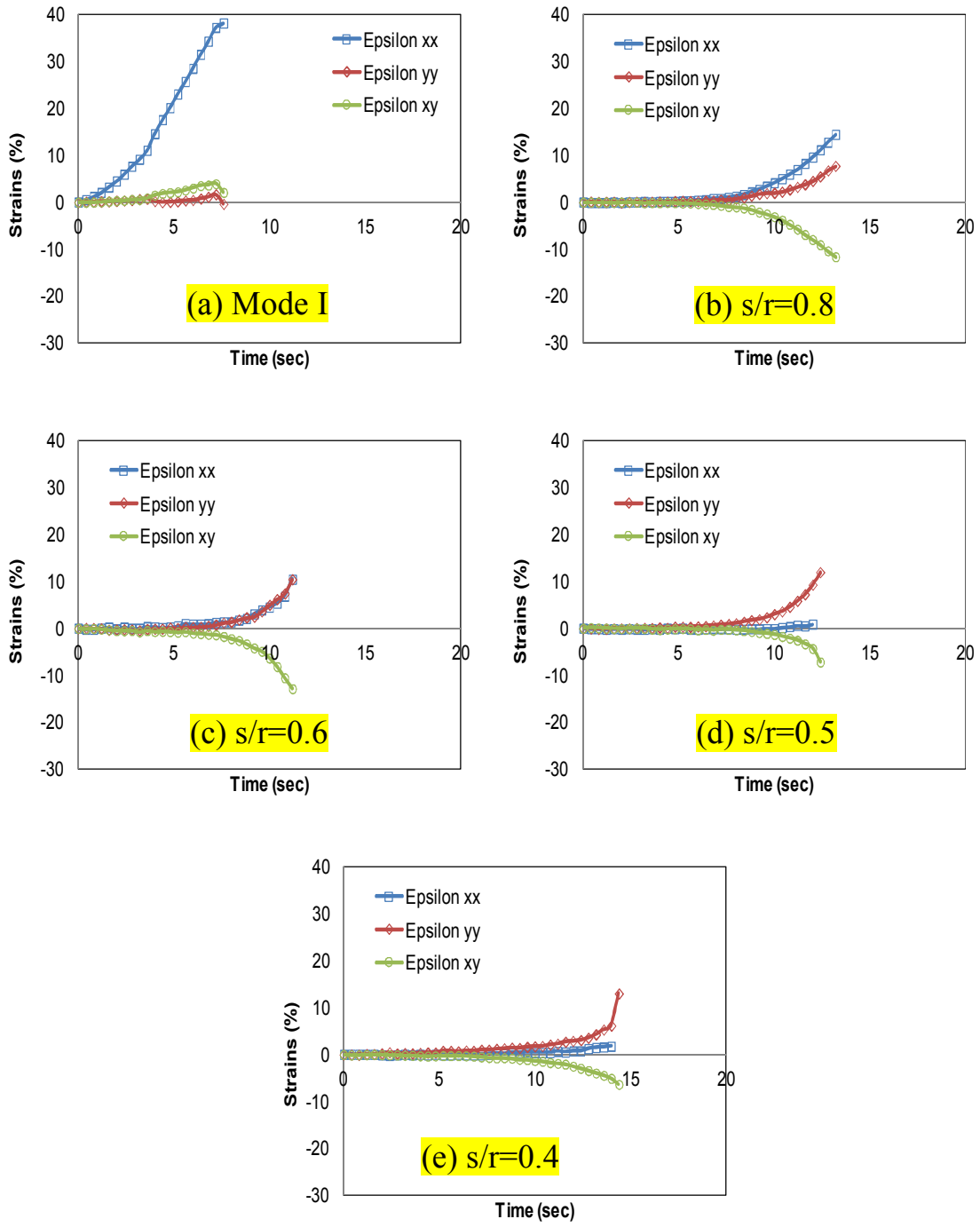

Figure 6-15. Strain Analysis Results (50° inclined notch)

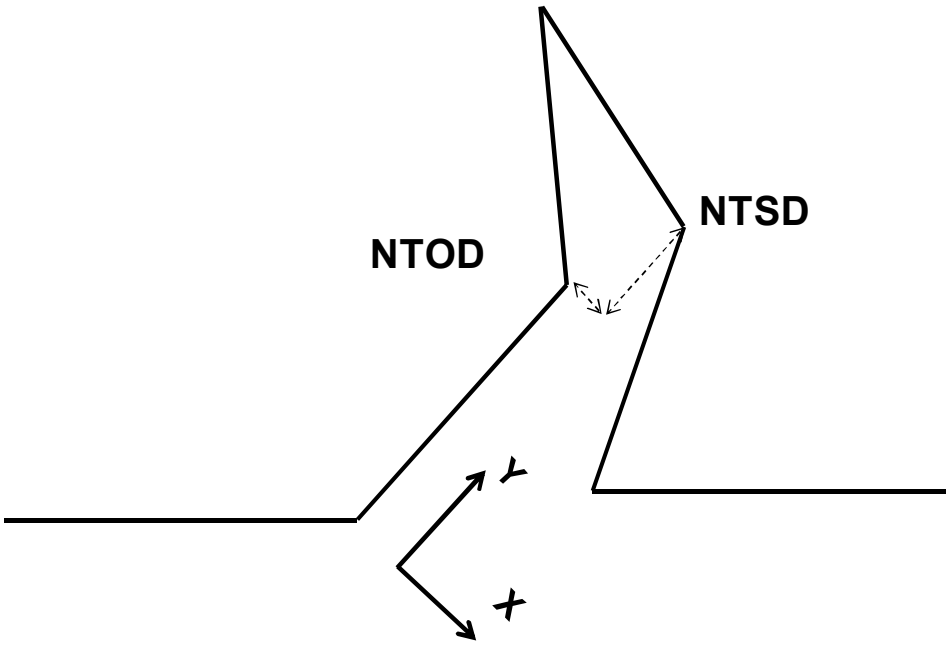

Figure 6-16. Fracture Parameters Determined: (NTOD and NTSD)

6.3.4. Mixed-mode fracture energy from force-displacement curve.

Two fracture parameters, NTOD and NTSD, and the reaction force are plotted against the loading time in Figure 6-17. Figure 6-17 (e) confirms that the testing configuration, s/r =0.4, used in this study created a pure shear mode condition, or very close to a pure shear mode condition, because the component of mode I, the opening displacement, was negligible during the testing. However, the test results from the mixed-mode testing configurations clearly presented mode I (opening displacement) and mode II (sliding displacement) characteristics during the testing, shown in Figure 6-17 (b) through (d).

Figure 6-18 and Figure 6-19 show the SCB mixed-mode test results with the average values between the reaction forces and the opening/sliding displacements plotted at different inclined notch angles of 45° and 50°. The figure clearly reveals the mixed-

mode-related behavior of the asphaltic materials. As the span ratio decreased, the resistance of the shear influences increased. From the figures, the peak forces of the SCB specimens with the 45° inclined notch were higher than those of the SCB specimens with the 50° inclined notch, while the SCB specimens with the 50° inclined notch produced longer softening curves than those of the SCB specimens with the 45° inclined notch.

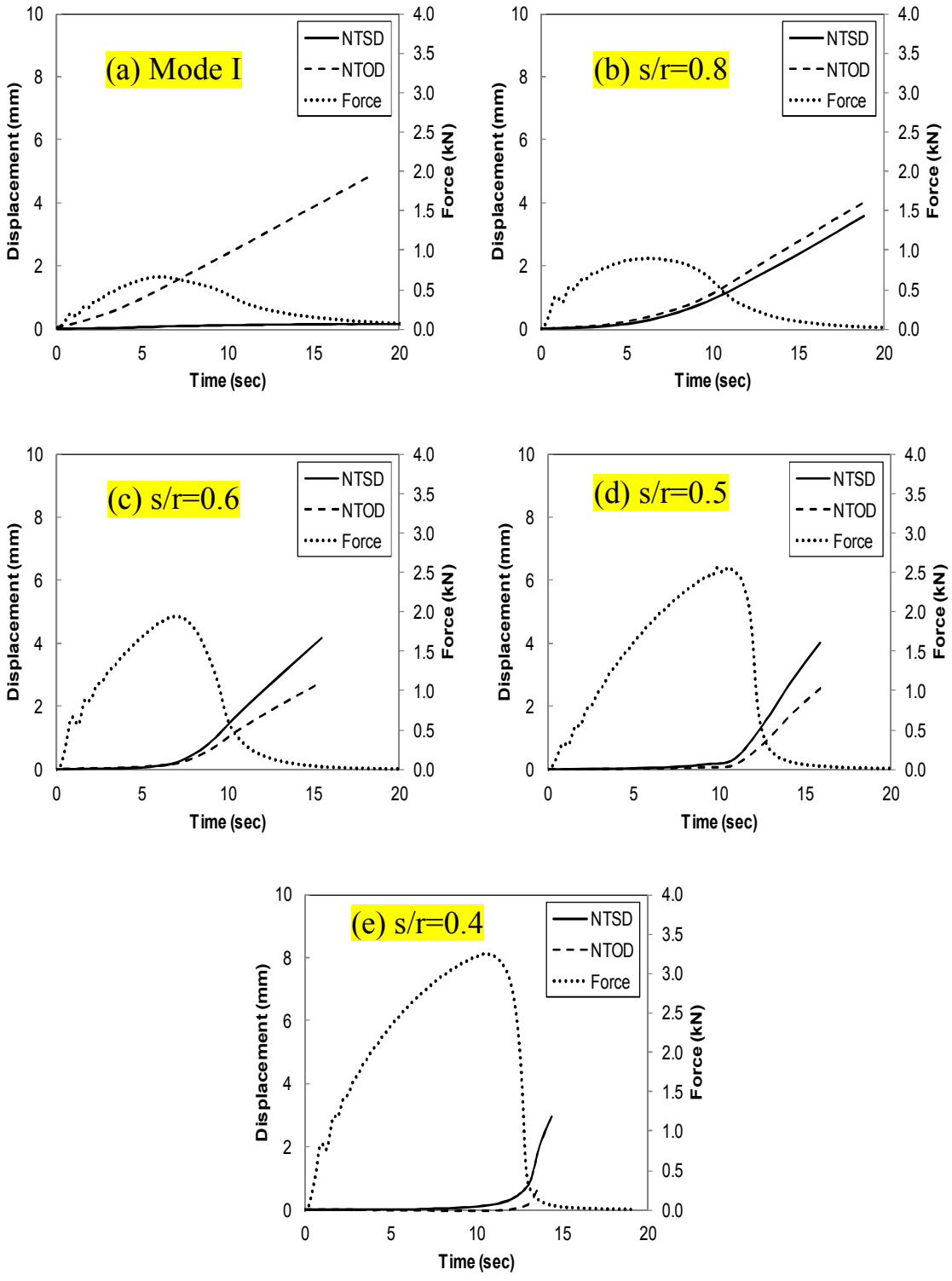

Figure 6-17. NTOD and NTSD from Each Testing Configuration (45° inclined notch)

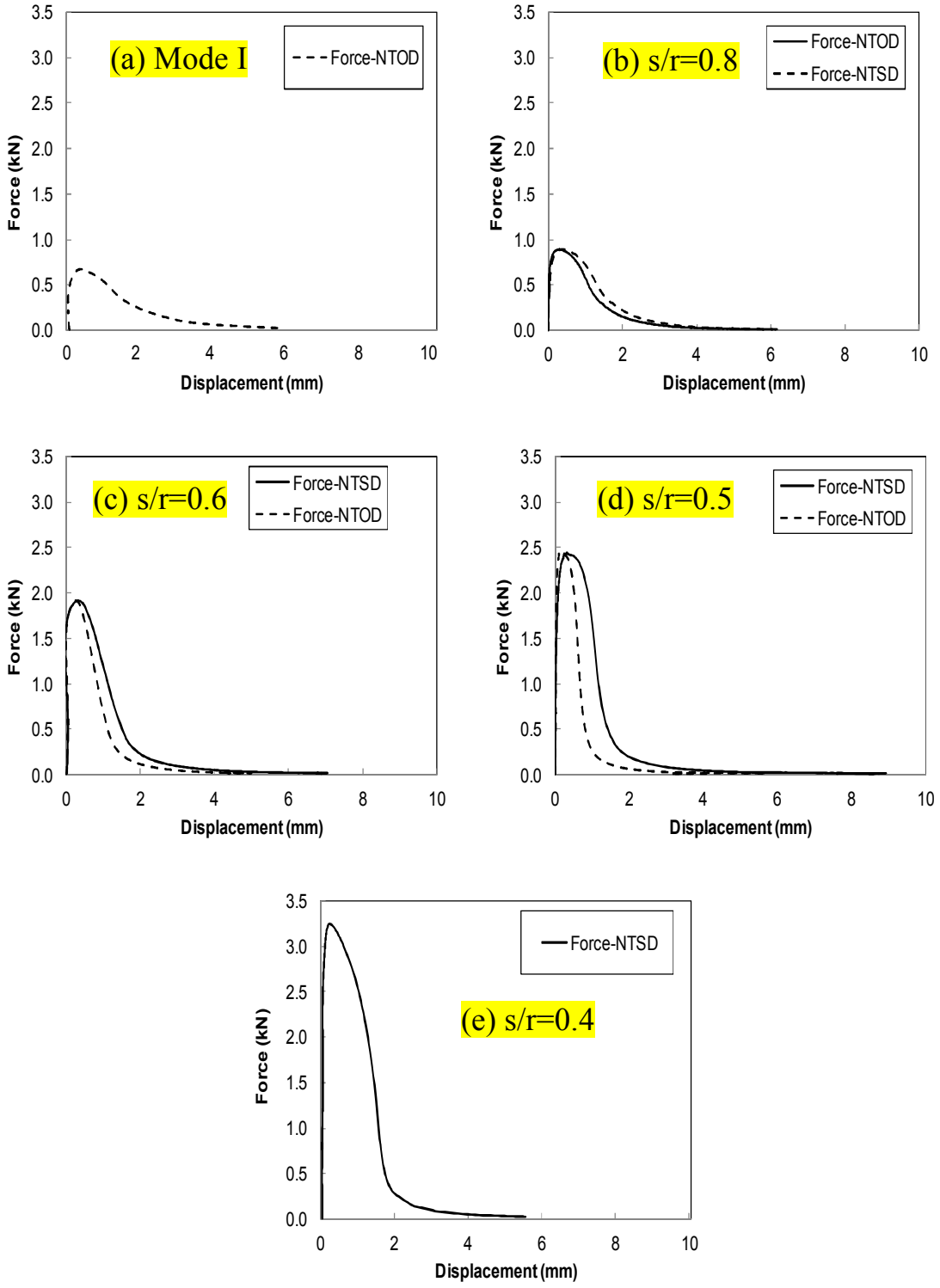

Figure 6-18. Force-NTOD and Force-NTSD Curves (45° inclined notch)

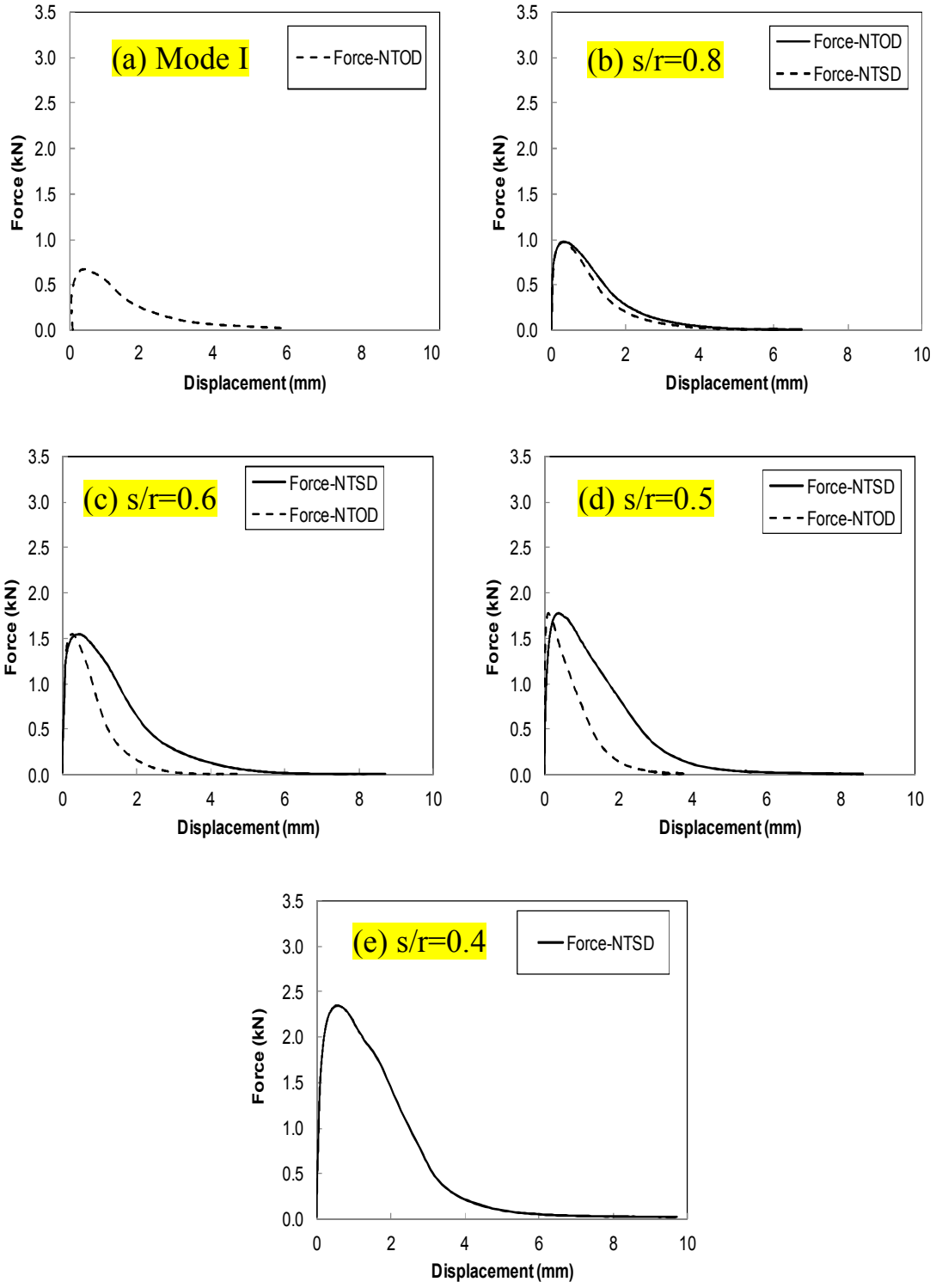

Figure 6-19. Force-NTOD and Force-NTSD Curves (50° inclined notch)

Table 6-6 summarizes the average fracture energy of each testing case. As described in section 6.2, the fracture energy was obtained by calculating the area under the force-NTOD curve and the force-NTSD curve normalized by the area of the fractured surface. The fracture energy, G_I, in this study, indicates the mode I fracture energy obtained from the area under the force-NTOD curve, while the fracture energy, G_{II}, indicates the mode II fracture energy obtained from the area under the force-NTSD curve. The fracture energy values obtained from the force-NTSD curves increased as the span ratio decreased, while the fracture energy values obtained from force-NTOD curves did not vary. The fracture energy values from s/r=0.4 fracture condition (mode II) were approximately 3.7-3.8 times greater than those for mode I.

G_{Total} was defined as the sum of G_I and G_{II} in this study, according to Bui (2011). One observation in the table illustrates that the G_{Total} from the 45° inclined notch case and the 50° inclined notch case were very similar to each other. Based on the limited test results, this implies that the notch angle affected the fracture behavior of the asphaltic materials, including peak force and softening, as mentioned above, but did not affect the total fracture energy. To confirm this result, however, extended tests at different notch angles should be performed in the future.

Table 6-6. Summary of Mixed-mode Fracture Energy (J/m^2)

	Inclined notch of 45°			Inclined notch of 50°		
	G_I	G_{II}	G_{Total}	G_I	G_{II}	G_{Total}
Mode I	1024.7	-	1024.7	1024.7	-	1024.7
s/r=0.8	1122.4	957.9	2080.3	1036.4	1217.8	2254.2
s/r=0.6	1280.8	1746.1	3026.8	1116.6	2156.6	3273.2
s/r=0.5	1236.2	2146.6	3382.9	1102.6	2400.4	3503.0
s/r=0.4	-	3682.8	3682.8	-	3782.1	3782.1

6.3.5. Mixed-mode fracture criterion.

Based on the test results, the mixed-mode criterion was proposed to account for the variation in fracture energy in the asphaltic materials in this study. Figure 6-20 presents the criterion fracture energy values ($G_c=G_{Total}$) that were experimentally obtained from the testing case where the inclined notch angle was 45° as a function of the mixed-mode ratio (G_{II}/G_{Total}) and fitted to a curve using sigmoidal functions as presented in Equation (6.3).

As illustrated in the figure, the critical fracture energy at either zero or the unity mixed-mode ratio (G_{II}/G_{Total}) represents pure mode I and II, respectively. As can be seen in the figure, the mode I fracture dominated between the mixed-mode ratio of 0 and 0.3, while the mode II fracture dominated between 0.7 and 1. However, the fracture energy increased somewhat linearly as the mixed-mode ratio increased from 0.3 to 0.7. This finding is very useful for the mixed-mode relation of asphaltic materials testing, especially regarding the SCB geometry condition. Even though several studies have used the SCB geometry with asphaltic materials, the mixed-mode relation has not yet been revealed.

In addition, one notable thing is associated with pavement design and analysis methods based on this result: As previously mentioned, most studies have considered the characteristics of mode I testing in pavement design and analysis methods; however, as shown in this study, the fracture energy values for mode II were approximately 3.7-3.8 times greater than those for mode I. This clearly indicates that the design and analysis of pavement structures should be based on proper characterization of asphaltic materials that is as realistic as possible.

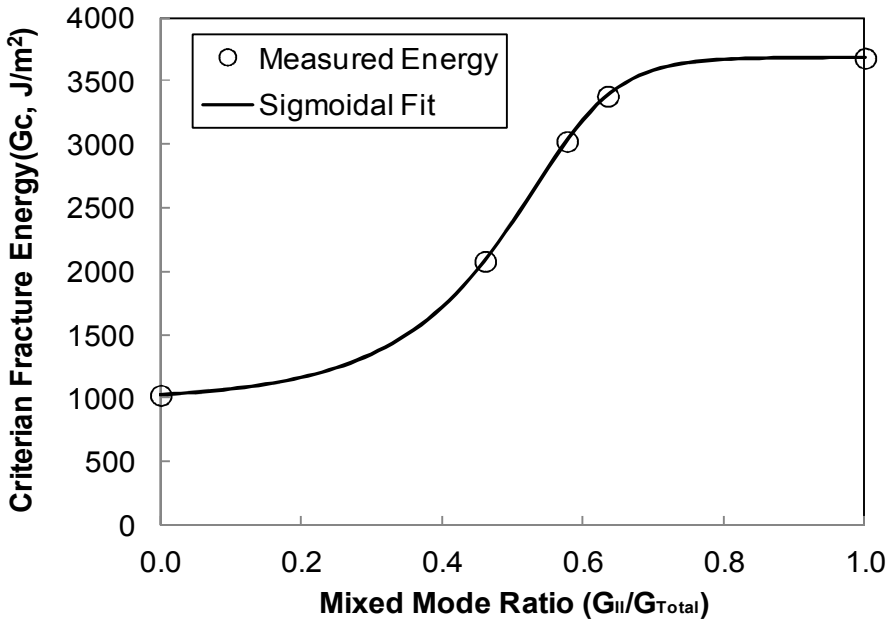

Figure 6-20. Mixed-mode Fracture Criterion for Asphalt Mixture: 45° inclined notch

$$G_c(J/m^2) = 982.220 + \frac{2700.971}{\left[1 + e^{-\left[\frac{(G_{II}/G_{Total})-0.581}{0.053}\right]}\right]^{0.378}} \quad \text{(for 45° inclined notch)} \qquad [6.3]$$

To see the validity of the mixed-mode criterion developed in this study, the predicted fracture energy values from the mixed-mode criterion were compared to those obtained from the SCB fracture testing case in which the inclined notch angle was 50°. Overall, Figure 6-21 shows a good match between the measured and predicted fracture energies except at the mixed-mode ratio of 0.55. This plot shows the mixed-mode criterion works well in predicting the fracture energy of asphaltic materials in the mixed-mode fracture. However, a set of limited mixed-mode testing program under a single monotonic displacement rate of 10 mm/min and a temperature of 21 °C was attempted to

account for the variation in fracture energy in the asphaltic materials in this study. In the future, extended fracture tests at various loading rates and temperatures should be performed since the asphaltic materials are rate- and temperature- dependent media.

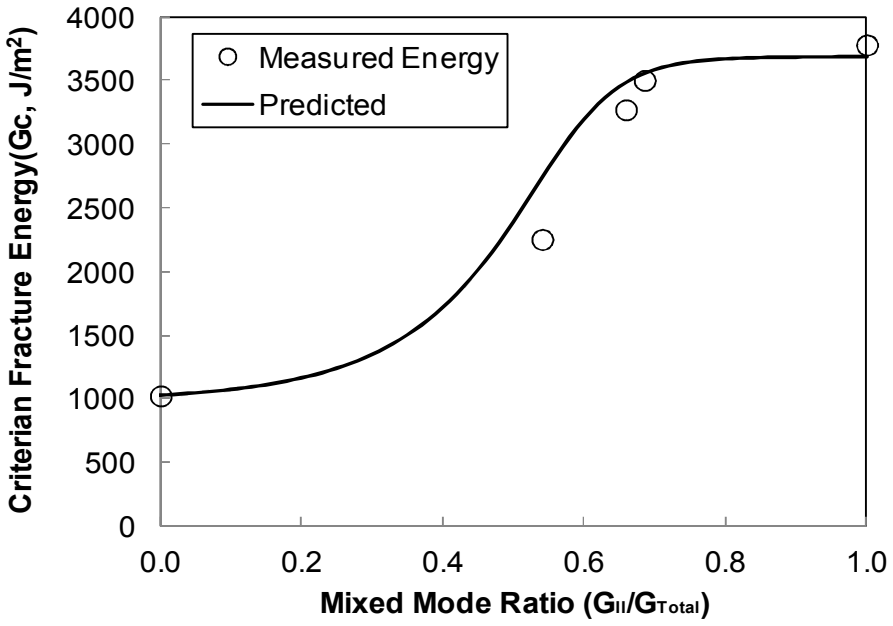

Figure 6-21. Measured (50° inclined notch) vs. Predicted Fracture Energy

6.4. Rate – and Mode – Dependent Fracture Properties

Most studies considered only pure mode I testing due to many difficulties involved in performing mode II testing. However, SCB geometry can create the mode II fracture condition as well as the mode I fracture. Thus, the SCB fracture testing was extended to investigate the rate-dependent fracture behavior of the asphaltic materials under the mode II fracture condition compared to that of the mode I fracture. This chapter

also presents the extended finite element method (XFEM) to find cohesive zone fracture properties of the mode II fracture as well as the mode I fracture.

6.4.1. Test results and fracture energy from force-displacement curve.

A total of 22 SCB specimens from the FAM mixture were prepared. Table 6-7 shows the testing plan. Before testing, the FAM SCB specimens were placed inside the environmental chamber of a mechanical testing machine for temperature equilibrium, targeting the reference temperature of 21 °C. Following the temperature conditioning step, presented in the table, mode I fracture testing was performed with six different monotonic displacement rates (i.e., 1, 5, 10, 50, 200, and 600 mm/min). After mode I fracture testing, four different monotonic displacement rates (i.e., 5, 10, 50, and 200 mm/min) were applied to the SCB specimens, the 50° inclined notch, to determine mode II fracture properties using the DIC.

Table 6-7. SCB Mode I Fracture Testing Plan

FAM Mixture at 21 (°C)							
Mode I	Rates (mm/min)	1	5	10	50	200	600
	No. of Specimens	2	2	2	2	2	2
Mode II	Rates (mm/min)	-	5	10	50	200	-
	No. of Specimens	-	2	2	3	3	-

Figure 6-22 presents the SCB test results of the mode I and mode II tests by plotting the average values of the reaction forces as the loading time increased at different loading rates. Figure 6-23 presents the average values of the reaction forces against the displacements (i.e., Force-NTOD for mode I and Force-NTSD for mode II) obtained from the DIC. As is clearly illustrated in the figures, the rate- dependent behavior of modes I and II was revealed at the testing temperature of 21 °C. Slower loading rates produced more compliant responses than faster loading cases, and as the loading rate increased, the peak force increased. The peak forces of the mode II tests were approximately four times (3.5-4.7) greater than those of the mode I tests at the same loading rates. The mode II fracture of the asphaltic materials may need more energy than the mode I fracture. Pictures of the SCB specimens after testing can be found in the appendix.

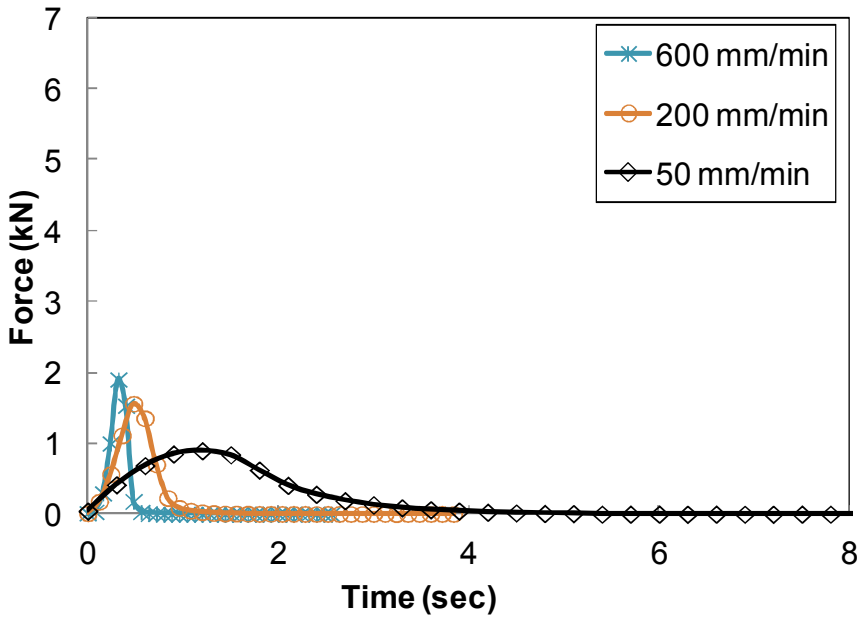

(a)

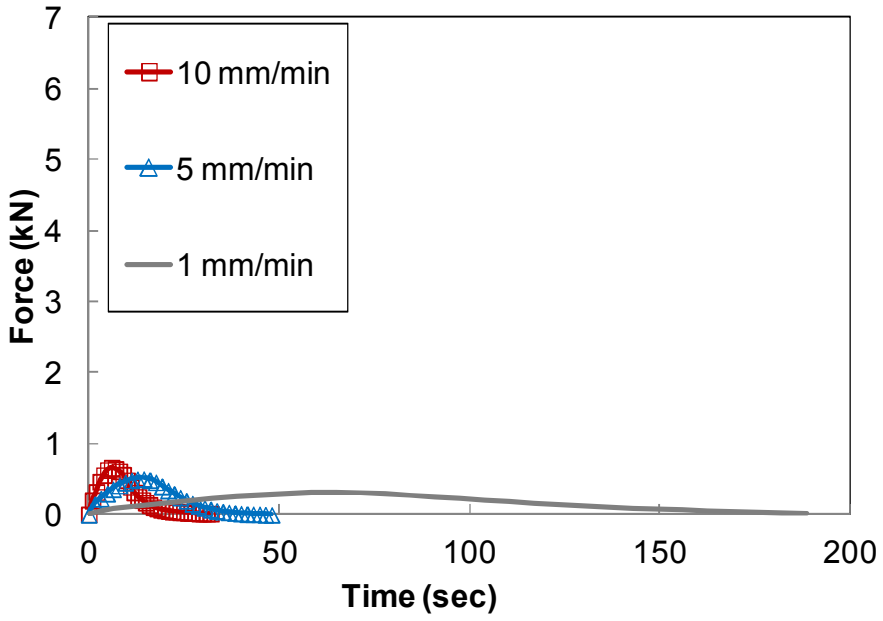

(b)

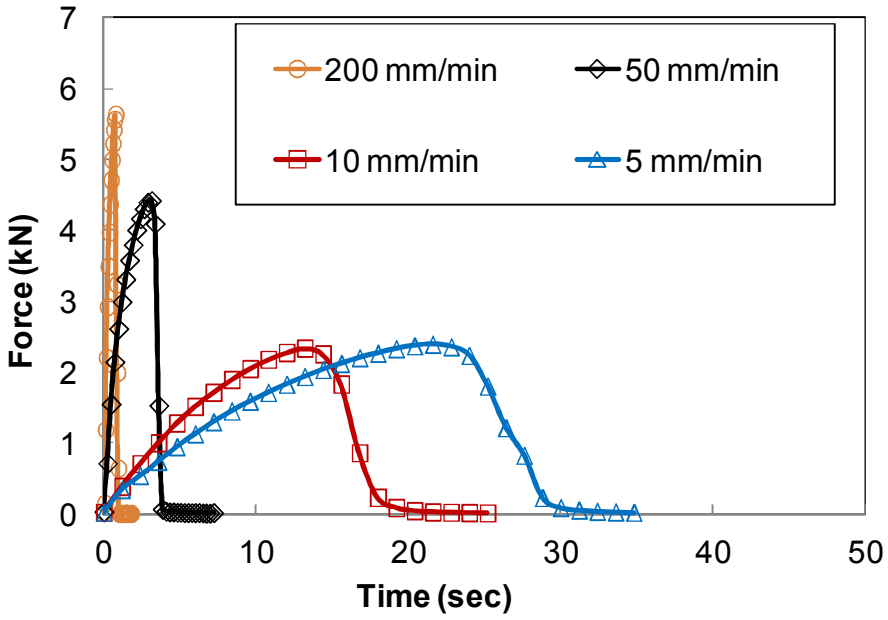

(c)

Figure 6-22. SCB Test Results at Different Loading Rates: (a) mode I (600, 200, 50 mm/min) (b) mode I (10, 5, 1 mm/min) (c) mode II

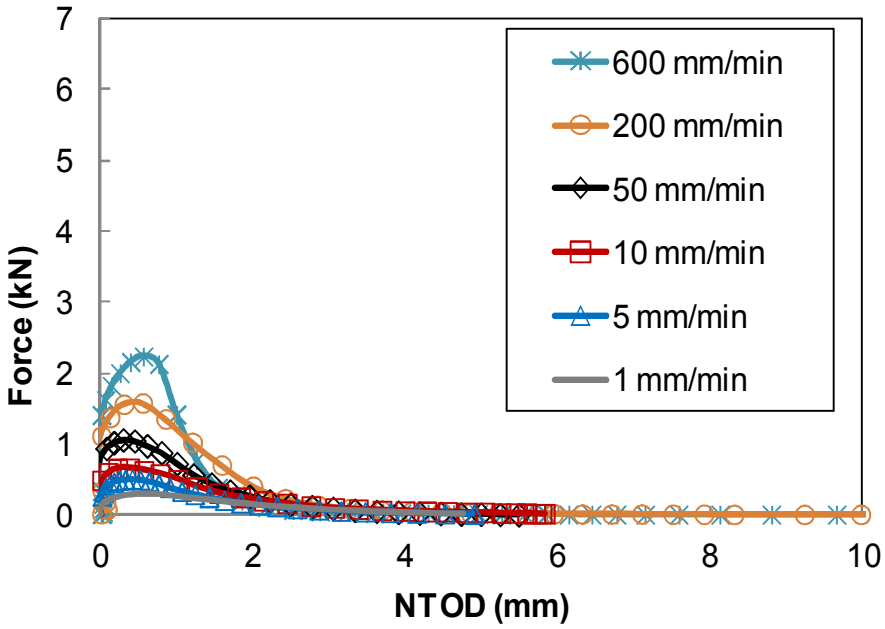

(a)

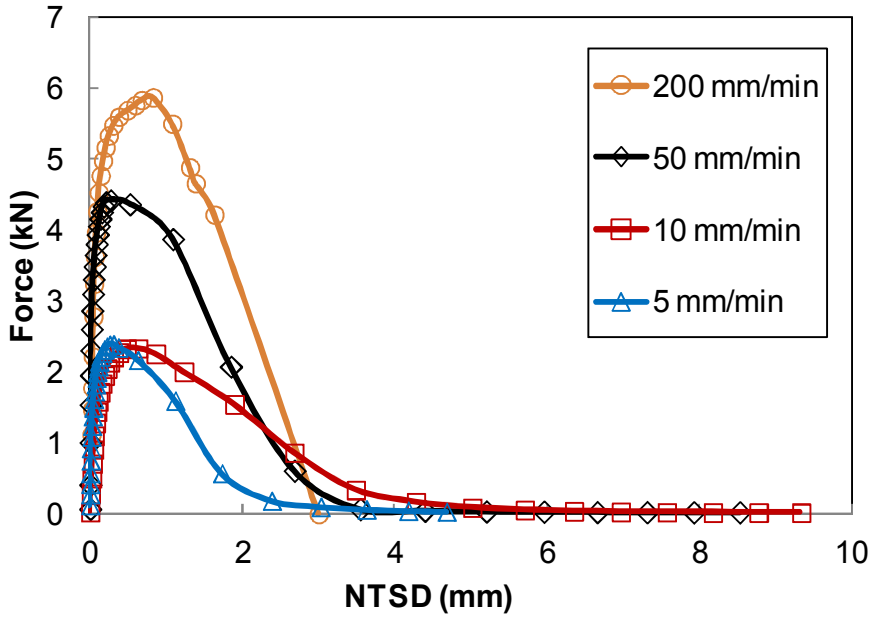

(b)

Figure 6-23. SCB Test Results: (a) Force-NTOD (b) Force-NTSD Curves (50° inclined notch)

Using the DIC test results, the fracture energies of mode I (G_I) and mode II (G_{II}) were calculated: G_I was calculated using the force-NTOD-DIC curve, and G_{II} was calculated using the force-NTSD-DIC curve, respectively. Table 6-8 summarizes the average fracture energies of mode I and mode II at different loading rates. As described earlier, this study estimated the fracture energy by calculating the area under the force-NTOD curve and the force-NTSD curve normalized by the area of the fractured surface.

The table clearly confirms that the fracture energy of modes I and II increased as the loading rates increased at the testing temperature of 21 °C. In addition, the fracture energies of the mode II tests were approximately 3.1–4.9 times greater than those of the mode I tests at the same loading rates. This clearly indicates the importance of proper material characterization in the asphalt pavement design and analysis methods because the fracture resistance and characteristics of asphaltic materials significantly influence the service life of asphalt pavements and consequently the maintenance costs.

Table 6-8. Summary of Fracture Energy of Mode I and Mode II (J/m^2)

Loading Rates (mm/min)	G_I (J/m^2)	G_{II} (J/m^2)	G_{II}/G_I
1	532.8	-	-
5	706.0	2184.0	3.1
10	1024.7	3782.1	3.7
50	1226.5	5982.4	4.9
200	2131.6	7631.7	3.6
600	2147.6	-	-

6.5. Fracture Energy from Extended Finite Element Modeling

Finite element modeling with the cohesive zone model was used to simulate the mode I fracture of the AC mixture, as described earlier. However, this conventional finite element method has an inherent drawback in predicting crack growth, such as the mode II fracture, because the crack can grow only along a predefined path of the mesh boundary. To overcome this limitation, Belytschko and Black (1999) introduced the extended finite element method (XFEM) as an extension of the conventional FEM to model arbitrary cracks in meshes under the assumption of LEFM. The XFEM adds enrichment functions to the approximation that contains a discontinuous displacement based on the local partition of unity (Babuska and Melenk, 1997). Therefore, the XFEM was used to simulate the mode II fracture as well as the mode I fracture of the FAM mixture.

Figure 6-24 presents a finite element mesh for mode I and mode II analysis. The specimen was discretized, and four-node bilinear plane stress element (CPS4 in ABAQUS) was used. As seen, the graded mesh was constructed to reduce computational time. The graded mesh was refined only around the potential crack path region, whereas in the area of low stress gradients, large elements were used. However, the crack potential region for the cohesive zone model was defined at the entire specimen.

As mentioned earlier, the cohesive zone fracture properties can be determined via a calibration process until a good agreement is observed between the experimental results and the numerical simulations of SCB testing performed at an appropriate loading configuration. Since the mixture was modeled as an isotropic and elastic material subjected to fracture, the two linear elastic properties (i.e. Young's modulus, E and Poisson's ratio, υ) and the fracture properties represented by cohesive properties (T_{max}

and Γ_c) for different fracture modes (mode I or II) were necessary as model inputs. In this study, it was reasonably assumed that, among the listed mechanical properties, Poisson's ratio was not affected by fracture modes with a constant value of 0.3 and the cohesive zone fracture properties ($T_{\max}$ and Γ_c) varied with loading rates and fracture modes.

Figure 6-25 presents the good agreement between the test results and the finite element simulations. The fracture properties resulting ($T_{\max}$ and Γ_c) at each loading rate and mode are presented in Table 6-9 (Ban et al., 2012). The cohesive zone fracture properties ($T_{\max}$ and Γ_c) of modes I and II increased as the loading rates increased. The cohesive zone fracture energies (Γ_c) of mode II simulations were approximately 3.1-3.2 times greater than those of mode I simulations at the same loading rates. However, the cohesive strength ($T_{\max}$) did not change between the mode I and mode II simulations. The cohesive strength ($T_{\max}$) may not be a mode- dependent property. This trend should be confirmed by simulating at various mixed-mode fracture conditions in the future.

The simulation using the XFEM herein also involved some limitations by assuming the mixture was isotropic and elastic material, which cannot consider viscoelastic behavior at this current stage. However, the modeling technique presented herein can identify the fracture modes of asphaltic materials and predict the crack path at each loading configuration.

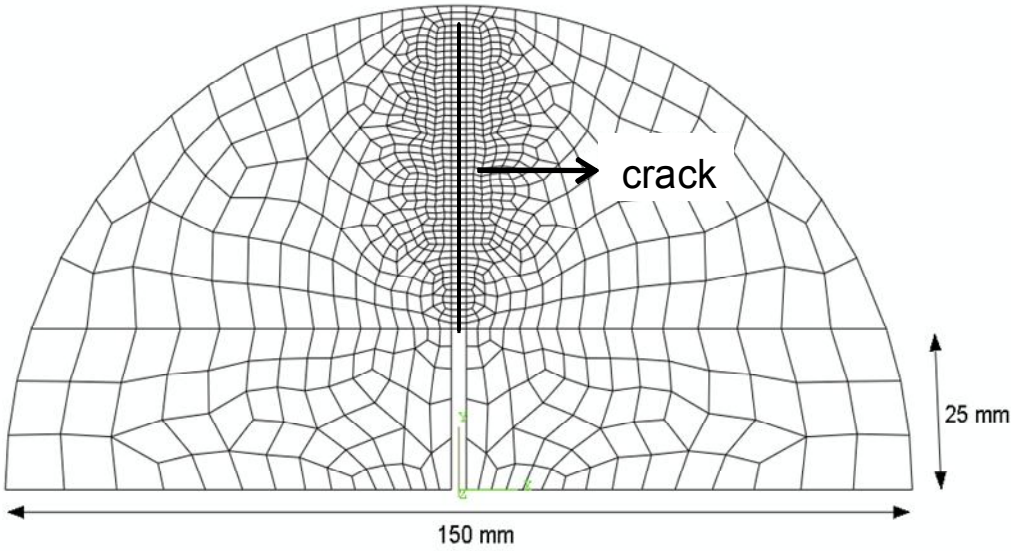

(a)

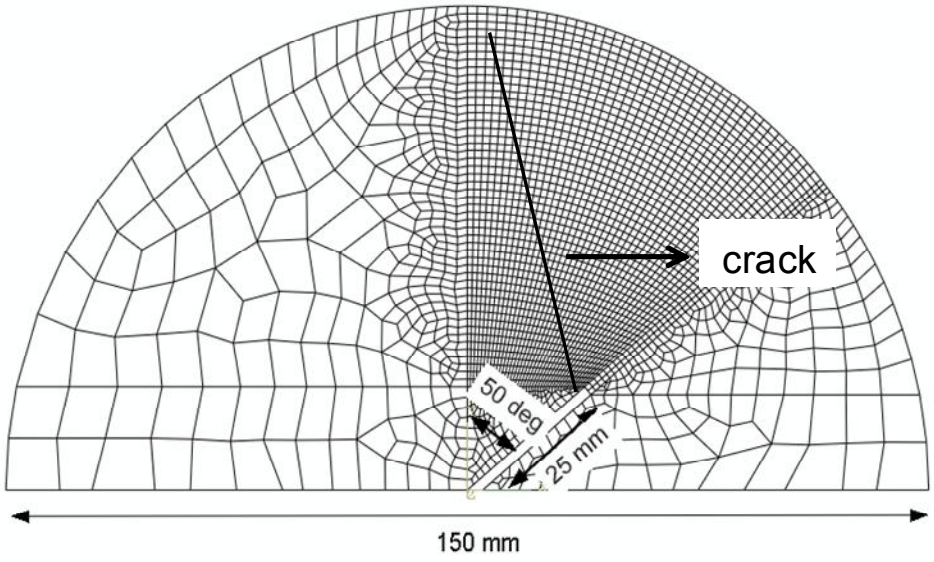

(b)

Figure 6-24. Finite element mesh: (a) mesh for pure mode I; (b) mesh for pure mode II (50°)

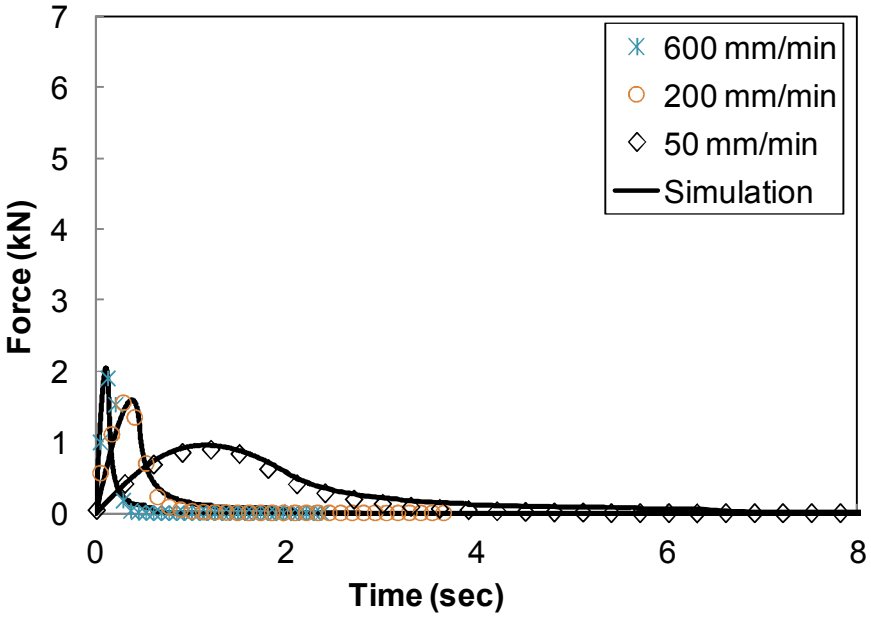
600 mm/min
200 mm/min
50 mm/min
Simulation
Force (kN)
Time (sec)
0
1
2
3
4
5
6
7
0
2
4
6
8

(a)

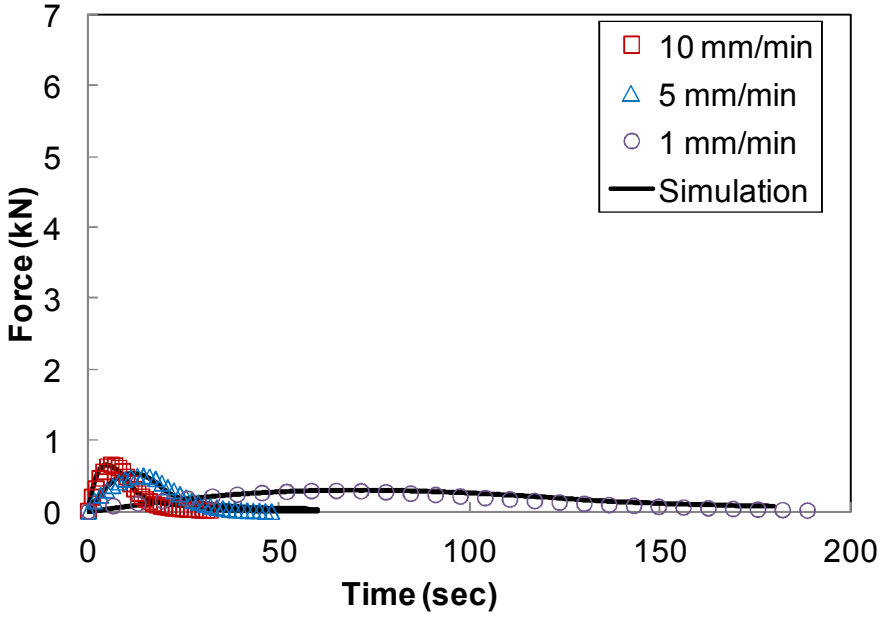
10 mm/min
5 mm/min
1 mm/min
Simulation
Force (kN)
Time (sec)
0
1
2
3
4
5
6
7
0
50
100
150
200

(b)

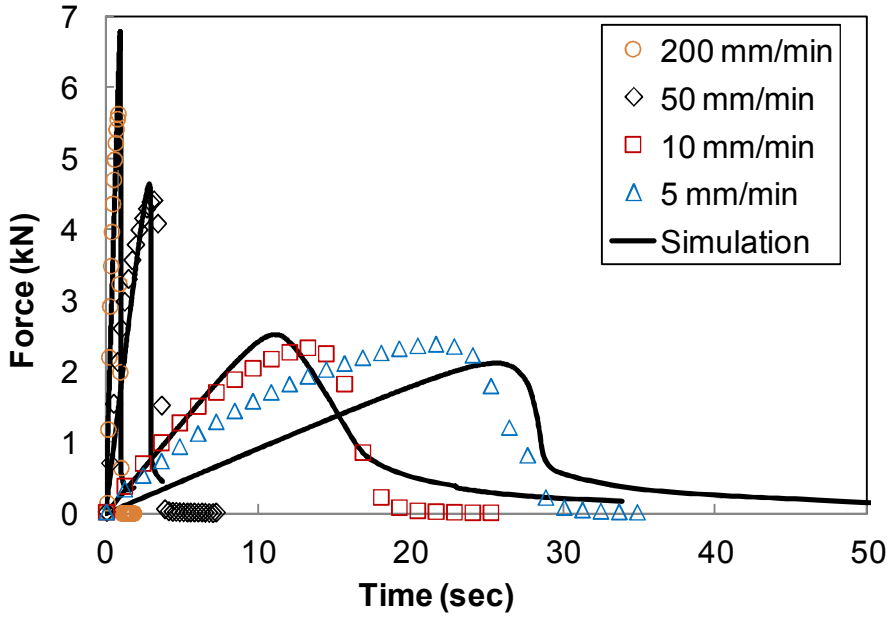

(c)

Figure 6-25. SCB test results vs. cohesive zone model simulation results: (a) mode I (600, 200, 50 mm/min) (b) mode I (10, 5, 1 mm/min) (c) mode II

Table 6-9. Cohesive Zone Fracture Parameters Determined

Loading Rates (mm/min)	Cohesive Zone Fracture Parameters				
	Γ_{IC} (J/m^2)	Γ_{IIC} (J/m^2)	Γ_{IC} / Γ_{IIC}	$T_{I\max}$ (kPa)	$T_{II\max}$ (kPa)
1	600	-	-	4.0E+02	-
5	800	2500	3.13	7.2E+02	7.2E+02
10	1200	3800	3.17	8.0E+02	8.0E+02
50	1500	4800	3.20	1.3E+03	1.3E+03
200	2000	6200	3.10	2.7E+03	2.7E+03
600	2500	-	-	3.2E+03	-

CHAPTER 7

CONCLUSIONS

This study intended to identify some of key relevant mechanical characteristics such as linear viscoelastic, non-linear viscoelastic, and fracture properties of asphaltic materials in two different length scales, e.g., mixture scale and component scale. More specifically, this study developed testing-analysis methods to rigorously define the stress-dependent nonlinear viscoelastic material characteristics at various stress levels and the viscoelastic mixed-mode fracture properties at different loading rates and testing temperatures. Based on the results and findings, the following conclusions can be made.

- Creep-recovery tests at varying stress levels were conducted using the AC and FAM mixture to identify nonlinear viscoelastic properties. Test results clearly demonstrated stress level-dependent mixture characteristics.
- Also, this study presented experimental-numerical efforts. Three-dimensional finite element simulations of the pavement structure presented significant differences between the linear viscoelastic approach and the nonlinear viscoelastic modeling in the prediction of pavement performance with respect to rutting. This implies that differences between the two approaches are considered significant and should be addressed in the process of performance-based pavement design.
- The SCB fracture test presented reasonable and repeatable results. The coefficient of variation between replicates was acceptable, and the test was successfully

suited to various strain measuring systems. Fracture behavior at the process zone presented sensitive responses to the loading rates and testing temperatures.

- The DIC results (NMOD and LPD) were quite compatible with conventional measurements obtained from the clip-on gauge and the cross-head. The DIC could also provide full-field surface displacements and local fracture process. This feature was not quite intensively used for this study at this time, but can be used to more accurately characterize the time-varying local FPZ of the mixture as some recent studies (Shen and Paulino 2011; Gain et al. 2011) attempted for different materials.
- The fracture energies obtained from force-NMOD (or force-NTOD) curves were always greater than those from the cohesive zone modeling. The deviation in the fracture energy between the two approaches was greater as the temperature increased and loading rates were lower. This indicates that fracture process is a local phenomenon that needs to be identified at the tip of FPZ. The fracture characteristics obtained from NMOD measurements overestimate the true fracture toughness, as it includes other sources of energy dissipation such as material viscoelasticity, which is not related to the fracture process.
- At low temperatures such as -10 ^{o}C, the fracture process was not rate-dependent, whereas the fracture energy at 0 ^{o}C to 30 ^{o}C clearly presented rate-related behavior. Fracture energy dropped as the loading speed became faster at 0 ^{o}C; however, the trend was the opposite at ambient temperatures. The findings from this study are generally in good agreement with other observations but remains further investigation to explain related mechanisms.

- The behavior of the SCB mixed-mode fracture as well as mode II fracture was investigated and fracture energies were calculated using the DIC results in this study. Even though the DIC process was time-consuming, expensive, and required additional techniques for data analysis, it enabled to understand the behavior of both modes I and II by providing detailed information on both opening/sliding displacements and local material behavior.
- The mixed-mode fracture criterion was developed to account for the variation in fracture energy in the asphaltic materials. The criterion was validated and showed a good prediction in the mixed-mode fracture condition. The findings clearly indicate that the design and analysis of pavement structures should be based on proper characterization of asphaltic materials that is as realistic as possible.
- The test and analysis results in this study suggest that the rate-, temperature-, mode- dependent fracture properties are necessary in the structural design of asphaltic pavements with which a wide range of strain rates and service temperatures is usually associated.

7.1. Significance and Contributions

Findings from this study can provide better insights into the more accurate and scientific design and analysis of pavement structures. Significant benefits and potential impact of this study can be listed as follows:

a) Appropriate test protocols that were developed in this study can be used for researchers and practitioners to characterize core material properties in the design and analysis of pavement mixtures and structures.

b) Cracking in asphalt pavements is a very complicated phenomenon due to combined effects. The fracture behavior studied herein included mixed-mode, rate- and temperature-dependency, which are known as key phenomena in the process of asphalt cracking but has not carefully been studied yet. This study will enhance the understanding of the fracture process and mechanisms in the asphaltic materials.

c) The material properties characterized from this study can be used for computational micromechanics models and multiscale models to evaluate the effects of individual components and their interactions on overall performance behavior of mixtures and structures. This can eventually lead to better selection of materials and more optimized design of mixtures and structures.

REFERENCES

1. AASHTO, (2008). “Mechanistic-Empirical Pavement Design Guide”, A Manual of Practice, Interim Edition.

2. AASHTO TP 62-07. (2008). “Determining dynamic modulus of hot-mix asphalt concrete mixtures. Standard Specifications for Transportation and Methods of Sampling and Testing.” 28th Edition, and Provisional Standards. America Association of State Transportation and Highway Engineering.

3. Airey, G., Rahimzadeh, B., Collop, A.C. (2004). “Linear Rheological Behavior of Bituminous Paving Material.” *Journal of Materials in Civil Engineering*, 16, 212–220.

4. Ayatollahi, M.R. and Aliha, M.R.M. (2007). “A wide range data for crack tip parameters in two disc-type specimens under mixed mode loading.” *Composite Materials Science*, 38:131-50.

5. Aliha, M.R.M., Ayatollahi, M.R., Smith, D.J., and Pavier, M.J. (2010). “Geometry and size effects on fracture trajectory in a limestone rock under mixed-mode loading.” *Engineering Fracture Mechanics*, 77:2200-12.

6. Al-Qadi, I.L., Loulizi, A., Janajreh, I., and Freeman, T.E. (2002). "Pavement response to dual and new wide base tires at the same tire pressure" *Transportation Research Record* 1806, 38-47.

7. Al-Qadi, I.L., Elseifi, M.A., and Yoo, P.J. (2004). "In-situ validation of mechanistic pavement finite element modeling" Proceedings, 2nd Int. Conference on Accelerated Pavement Testing, Minneapolis.

8. Al-Qadi, I.L., Yoo, P. J., and Elseifi, M. A., (2005). "Characterization of Pavement Damage Due to Different Tire Configurations", *Journal of the Association of Asphalt Paving Technologists*, No 74, 921-962.

9. Aragão, F.T.S. and Kim, Y.R., (2011). "Characterization of Fracture Properties of Asphalt Mixtures Based on Cohesive Zone Modeling and Digital Image Correlation Technique" TRB 2011 Annual Meeting.

10. Aragão, F.T.S. (2011). "Computational microstructure modeling of asphalt mixtures subjected to rate-dependent fracture." Ph.D. Dissertation, University of Nebraska, Lincoln, Nebraska.

11. Aragão, F.T.S., Kim, Y., Lee, J., and Allen, D.H. (2011). "Micromechanical model for heterogeneous asphalt concrete mixtures subjected to fracture failure." *Journal of Materials in Civil Engineering*, 23(1), 30-38.

12. Ayatollahi, M.R., and Aliha, M.R.M. (2007). "A wide range data for crack tip parameters in two disc-type specimens under mixed-mode loading." *Composite Materials Science,*; 38:131-50.

13. Ban, H., Im, S., and Kim, Y.R. (2011). "Nonlinear Viscoelastic Modeling of Asphaltic Mixture and Pavement Structure." Unpublished manuscript.

14. Ban, H., Im, S., and Kim, Y.R. (2012). "Characterization of Fracture Properties of Asphalt Mixture under Mixed-Mode Loading Configuration." Unpublished manuscript.

15. Babuska, I. and Melenk, J. (1997). "The partition of unity method." *International Journal for Numerical Methods in Engineering,* 40:727-58.

16. Bazant, Z.P. and Planas J. (1998). "Fracture and size effect in concrete and other quasibrittle materials." CRC Press.

17. Belytschko, T. and Black, T. (1999). "Elastic crack growth in finite elements with minimal remeshing." *International Journal for Numerical Methods in Engineering*, 45:601-20.

18. Blab, R., and Harvey, J.T. (2002). "Modeling measured 3D tire contact stresses in a viscoelastic FE pavement model." *International Journal of Geomechanics* 2(3) 271-290.

19. Braham, A.F. (2008). "Fracture Characteristics of Asphalt Concrete in Mode I, Mode II, and Mixed-Mode", Ph.D. Dissertation, University of Illinois, Urbana, Illinois

20. Bui, Q.V., (2011). "A Modified Benzeggagh-Kenane Fracture Criterion for Mixed-mode Delamination", *Journal of Composite Materials,*; Vol. 45, No. 4, 389-413.

21. Collop, A.C., Scarpas, A., Kasbergen Cor, Bondt, A., (2003). "Development and Finite Element Implementation of Stress-Dependent Elastoviscoplastic Constitutive Model with Damage for Asphalt", *Transportation Research Record*, Vol. 1832, 96-104.

22. Duan, K., Hu, X., and Wittmann F.H. (2006). "Scaling of quasi-brittle fracture: boundary and size effect." *Mechanics of Materials*, 38, 128-141.

23. Elseifi, M.A., Al-Qadi, I.L., and P.J. Yoo., (2006). "Viscoelastic Modeling and Field Validation of Flexible Pavements", *Journal of Engineering Mechanics*, ASCE, Vol. 132, No. 2, 172-178.

24. Elseifi, M.A. and Al-Qadi, I.L. (2006). "Modeling of strain energy absorbers for rehabilitated cracked flexible pavements, *Journal of Transportation Engineering*, 131(9), 653-661.

25. Espinosa, H.D. and Zavattieri, P.D. (2003). “A grain level model for the study of failure initiation and evolution in polycrystalline brittle materials, part I: theory and numerical implementation.” *Mechanics of Materials*, 35, 2003, 333-364.

26. Gain, A.L., Carroll, J., Paulino, G.H., and Lambros, J., (2011) “A hybrid experimental/numerical technique to extract cohesive fracture properties for mode-I fracture of quasi-brittle materials.” *International Journal of Fracture*, 169, 113-131.

27. Geubelle, P. and Baylor, J. (1998). “Impact-induced delamination of laminated composites: a 2D simulation.” *Composites Part B – Engineering*, 29(5), 589-602.

28. Hoare, T.R., Hesp, S.A.M. (2000). “Low-temperature fracture testing of asphalt binders: regular and modified systems.” *Transportation Research Record,* 1728:36–42

29. Huang, C.W., Abu Al-Rub, R.K., Masad E.A., and Little, D.N., (2011). “Three-Dimensional Simulations of Asphalt Pavement Permanent Deformation using a Nonlinear Viscoelastic and Viscoplastic Model”, *Journal of Materials in Civil Engineering*, ASCE, Vol. 23, No.1, pp.56-68.

30. Kim, H. and Buttlar, W.G. (2009). “Discrete Fracture Modeling of Asphalt Concrete. *International Journal of Solids and Structures*, 46, 2593-2604.

31. Kim, K.W., Kweon S.J., Doh, Y.S., and Park, T.S. (2003). "Fracture toughness of polymer-modified asphalt concrete at low temperatures." *Canadian Journal of Civil Engineering*, 30, 406-413.

32. Kim, H., Wagoner, M.P., and Buttlar W.G., (2008). "Simulation of Fracture Behavior in Asphalt Concrete Using a Heterogeneous Cohesive Zone Discrete Element Model", *Journal of Materials in Civil Engineering*, ASCE, Vol. 20, No.8, pp.552-563.

33. Kim, J., Roque, R., and Byron, T., (2009). "Viscoelastic Analysis of Flexible Pavements and its Effects on Top-Down Cracking.", *Journal of Materials in Civil Engineering*, Vol. 27, No.7, pp. 324-332.

34. Kim, J., Byron, T., Sholar, G.A. and Kim, S. (2008). "Comparison of a Three-Dimensional Visco-Elastic Modeling and Field Validation of Flexible Pavements", TRB 2008 Annual Meeting CD-ROM.

35. Kim, Y.R., Allen, D.H., and Little, D.N., (2005). "Damage-Induced Modeling of Asphalt Mixtures through Computational Micromechanics and Cohesive Zone Fracture", *Journal of Materials in Civil Engineering*, Vol. 17, No.5, pp. 477-484.

36. Kim, Y.R., Allen, D.H., and Little, D.N., (2007). "Computational constitutive model for predicting nonlinear viscoelastic damage and fracture failure of asphalt concrete mixtures." *International Journal of Geomechanics*, 7(2), 102-110.

37. Kim, Y.R., Allen, D.H., and Seidel, G.D. (2006). "Damage-induced modeling of elastic-viscoelastic randomly oriented particulate composites" *Journal of Engineering Materials and Technology*, 126, 18-27.

38. Kim, Y.R., Aragao, F.T., Allen, D.H., and Little, D.N. (2010). "Damage modeling of bituminous mixtures through computational micromechanics and cohesive zone fracture." *Canadian Journal of Civil Engineering*,. 2010:37(8):1125-1136.

39. Kim, Y.R., Daniel, J.S., and Wen, H. (2002). "Fatigue performance evaluation of WestTrack asphalt mixtures using viscoelastic continuum damage approach." Final Report No. FHWA/NC/2002-004, North Carolina State University.

40. Kim, Y.R., Ban, H., and Im, S. (2011). "Impact of Truck Loading on Design and Analysis of Asphaltic Pavement Structures-Phase II." Final Report No. MATC-UNL:321, Mid-America Transportation Center.

41. Lee, N.K, Morrison, G.R., and Hesp S.A.M. (1995). "Low temperature fracture of poluethylene-modified asphalt binders and asphalt concrete mixes." *Journal of the Association of Asphalt Paving Technologists,* 64:534–574

42. Lai, J. and Bakker, A. (1996). "3-D Schapery representation for non-linear viscoelasticity and finite element implementation" *Computational Mechanics*, 18, 182-191

43. Li, X. and Marasteanu, M.O. (2004). "Evaluation of the low temperature fracture resistance of asphalt mixtures using the semi circular bend test." *Journal of the Association of Asphalt Paving Technologists,* 73:401–426

44. Li, X. and Marasteanu, M.O. (2005). "Cohesive modeling of fracture in asphalt mixtures at low temperatures." *International Journal of Fracture*, 136, 285-308.

45. Li, X-J., and Marasteanu, M.O. (2006). "Investigation of low temperature cracking in asphalt mixtures by acoustic emission." *International Journal of Road Materials and Pavement Design*, 7(4):491–512

46. Li, X. and Marasteanu, M.O. (2010). "The fracture process zone in asphalt mixture at low temperature." *Engineering Fracture Mechanics*, 77, 1175-1190.

47. Lim, I.L., Johnston, I.W., and Choi, S.K. (1993). "Stress intensity factors for semi-circular specimens under three-point bending." *Engineering Fracture Mechanics*, 43:363-82.

48. Lim, I.L., Johnston, I.W., Choi, S.K., and Boland, J.N. (1994). "Fracture Testing of Soft Rock with Semicircular Specimens under Three-Point Bending, Part 2 – Mixed-Mode. *International Journal of Rock Mechanics and Mining Science*, 31(3), 199-212.

49. Marasteanu, M.O., Dai, S.T., Labuz, J.F., and Li, X. (2002). "Determining the low-temperature fracture toughness of asphalt mixtures." *Transportation Research Record* 1789, 191-199.

50. Marasteanu, M.O., Zofka, A., Turos, M., Li, X., Velasques, R., Li, X., Buttlar, W., Paulino, G., Braham, A., Dave, E., Ojo, J., Bahia, H., Williams, C., Bausano, J., Gallistel, A., and McGraw, L. (2007). "Investigation of low temperature cracking in asphalt pavements: national pooled fund study 776." Final Report No. MN/RC 2007-43, Minnesota Department of Transportation.

51. Marzi, S., Hesebeck, O., Brede, M., and Kleiner, F. (2009). "A rate-dependent cohesive zone model for adhesively bonded joints loaded in mode I. *Journal of Adhesion Science and Technology*, 23, 881-898.

52. Masad, E., and Somadevan, N. (2002). "Microstructural Finite-Element Analysis of Influence of Localized Strain Distribution of Asphalt Mix Properties." *Journal of Engineering Mechanics*, 128, 1105–1114.

53. Mobasher, B., Mamlouk, M., and Lin, H. (1997). "Evaluation of crack propagation properties of asphalt mixtures." *Journal of Transportation Engineering*, 123 (5):405–413.

54. Molenaar, A.A.A., Scarpas, A., Liu, X., Erkens, SMJG. (2002). "Semicircular bending test: simple but useful?" *Journal of the Association of Asphalt Paving Technologists,* 71:795–815.

55. Mull, M.A., Stuart, K., and Yehia, A. (2002). "Fracture resistance characterization of chemically modified crumb rubber asphalt pavement." *Journal of Materials Science*, 37, 557-566.

56. Mun, S., Guddati, M., and Kim, Y.R. (2004). "Fatigue cracking mechanisms in asphalt pavements with viscoelastic continuum damage finite-element program" *Transportation Research Record*, 1896, 96-106.

57. Nguyen, T.D., S. Govindjee, P. A. Klein, and H. Gao., (2004). "A rate-dependent cohesive continuum model for the study of crack dynamics." *Computer Methods in Applied Mechanics and Engineering*, 193, 3239-3265.

58. Rahul-Kumar, P., Jagota, A., Benninson, S.J., and Saigal, S. (1999). "Muralidhar. Polymer interfacial fracture simulations using cohesive elements." *Acta Materialia*, 47(15), 4161-4169.

59. Schapery, R.A. (1969). "On the Characterization of Nonlinear Viscoelastic Materials" *Polymer Engineering and Science*, Vol. 9, No. 4.

60. Seo, Y., Kim, Y.R., and Witczak, M.W. (2002). "Application of the digital image correlation method to mechanical testing of asphalt-aggregate mixtures." *Transportation Research Record* 1789, 162-172.

61. Seo, Y.G. (2003). "A Comprehensive Study of Crack Growth in Asphalt Concrete using Fracture Mechanics." Doctoral Dissertation, Civil Engineering, North Carolina State University

62. Shen, B. and Paulino, G.H. (2011). "Direct extraction of cohesive fracture properties from digital image correlation: a hybrid inverse technique." *Experimental Mechanics*, 51, 143-163.

63. Song, S.H., Paulino, G.H., and Buttlar, W.G. (2006)., "A bilinear cohesive zone model tailored for fracture of asphalt concrete considering viscoelastic bulk material." *Engineering Fracture Mechanics*, 2829-2847.

64. Song, S.H., Wagoner, M.P., and Paulino, G.H. (2008). "δ_{25} crack opening displacement parameter in cohesive zone models: experiments and simulations in asphalt concrete." *Fatigue and Fracture of Engineering Materials and Structures*, 31, 850-856.

65. Soares, R.F., Allen, D.H., Kim, Y., Berthelot, C., Soares, J.B., and Rentschler, M.E. (2008). "A Computational Model for Predicting the Effect of Tire Configuration on Asphaltic Pavement Life". *International Journal on Road Materials and Pavement Design*, 9(2), 271-289

66. Wagoner, M.P., Buttlar, W.G., Paulino, G.H. (2005). "Development of a single-edge notched beam test for asphalt concrete mixtures." *Journal of Testing Evaluation*, 33(6):452–460

67. Wagoner, M.P., Buttlar, W.G., Paulino, G.H. (2005). "Disk-shaped compact tension test for asphalt concrete fracture." *Society for Experimental Mechanics* 45(3):270–277

68. Wagoner, M.P., Buttlar, W.G., Paulino, G.H., Blankenship, P. (2006). "Laboratory testing suite for characterization of asphalt concrete mixtures obtained from field cores." *Journal of the Association of Asphalt Paving Technologists,* 75:815–852

69. Wagoner, M.P. (2006). "Fracture Tests for Bituminous-Aggregates Mixtures: Laboratory and Field Investigations." Ph.D. Dissertation, University of Illinois, Urbana, Illinois

70. Yoo, P.J., (2007). "Flexible Pavement Dynamic Responses Analysis and Validation for Various Tire Configurations" Ph.D. Dissertation, Civil Engineering, University of Illinois at Urbana-Champaign.

71. Zaoutsos, S.P. and Papanicolaou, G.C. (2010). "On the influence of preloading in the nonlinear viscoelastic-viscoplastic response of carbon-epoxy composites" *Composites Science and Technology*, 70, 922-929

APPENDIX

Pictures after Testing

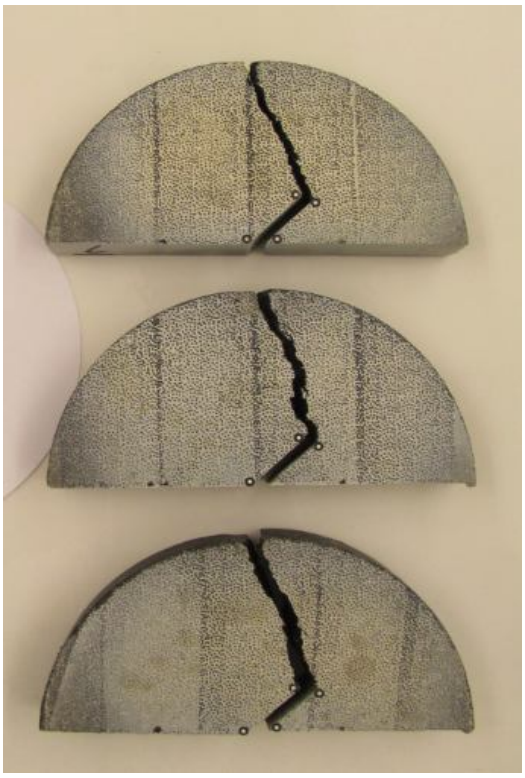

(1) 45°, Mode II (s/r=0.4)

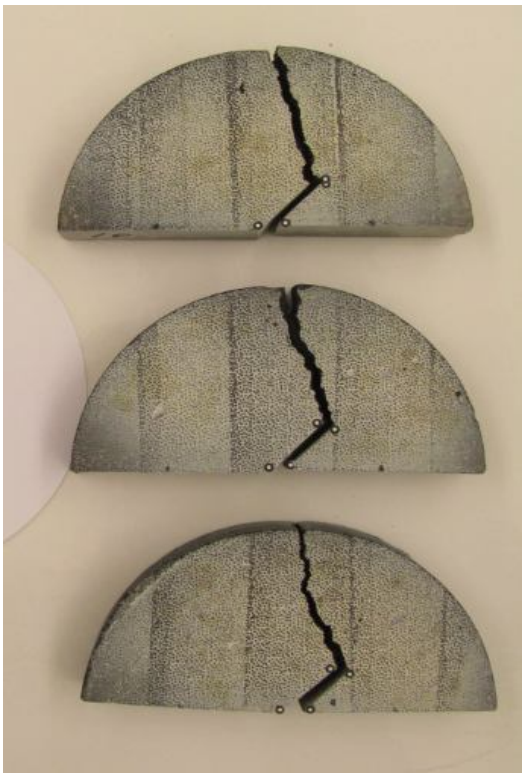

(2) 45°, s/r=0.5

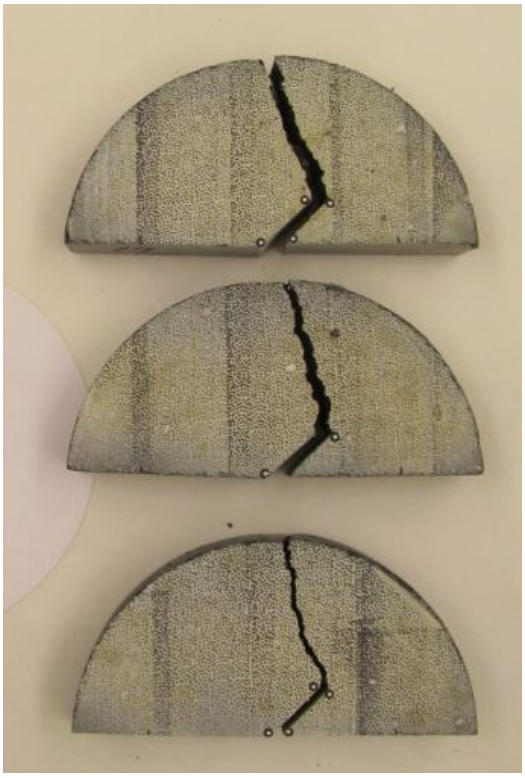

(3) 45°, s/r=0.6

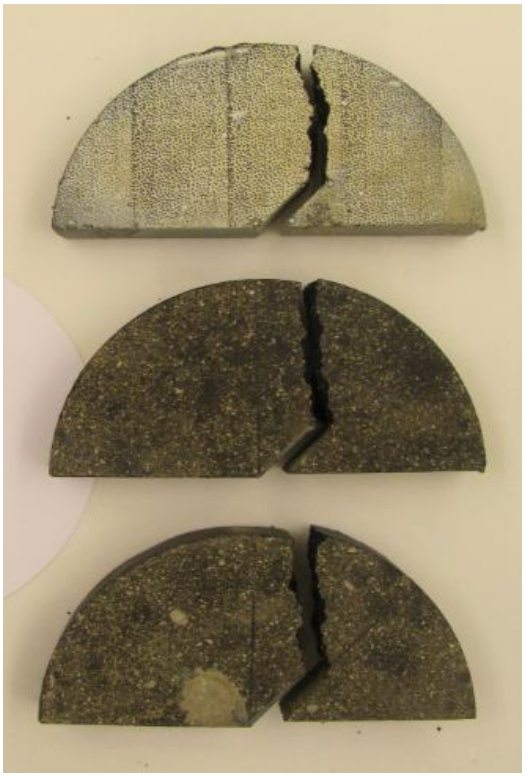

(4) 45°, s/r=0.8

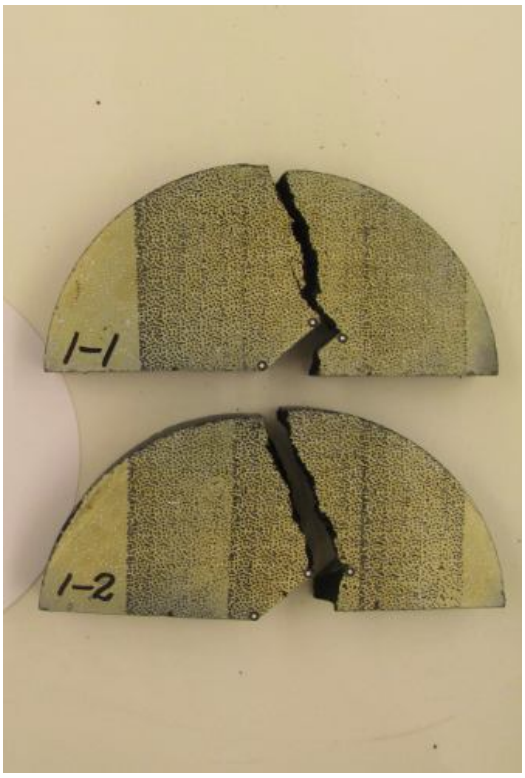

(5) 50°, Mode II (s/r=0.4)

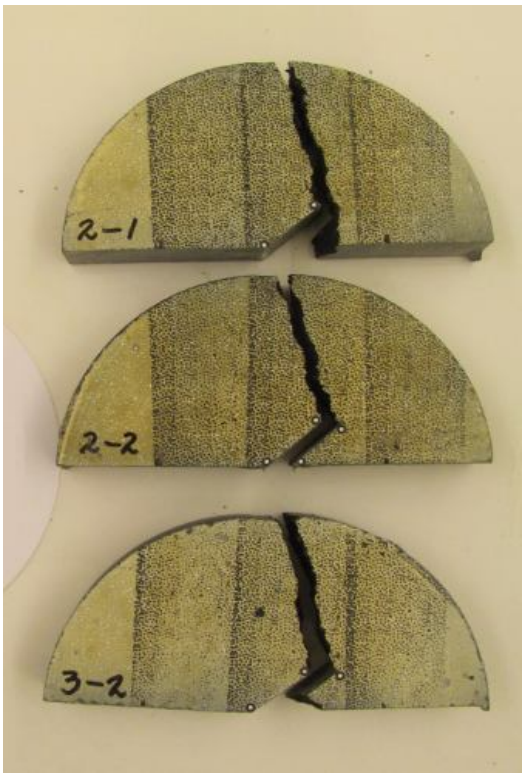

(6) 50°, s/r=0.5

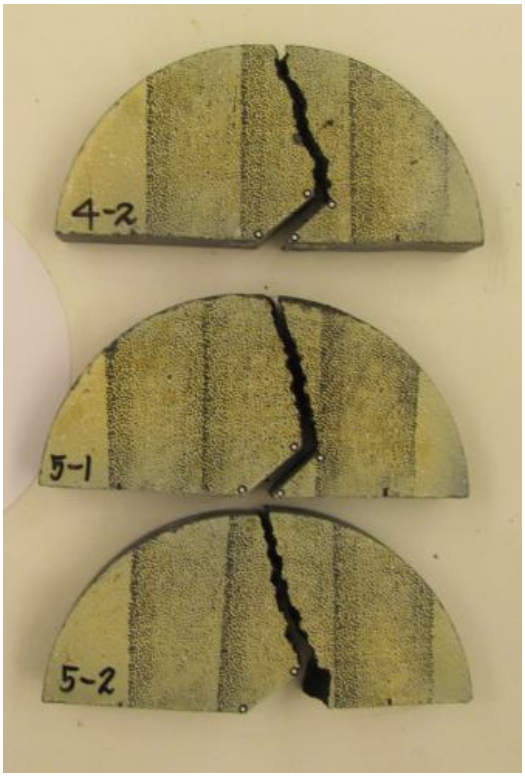

(7) 50°, s/r=0.6

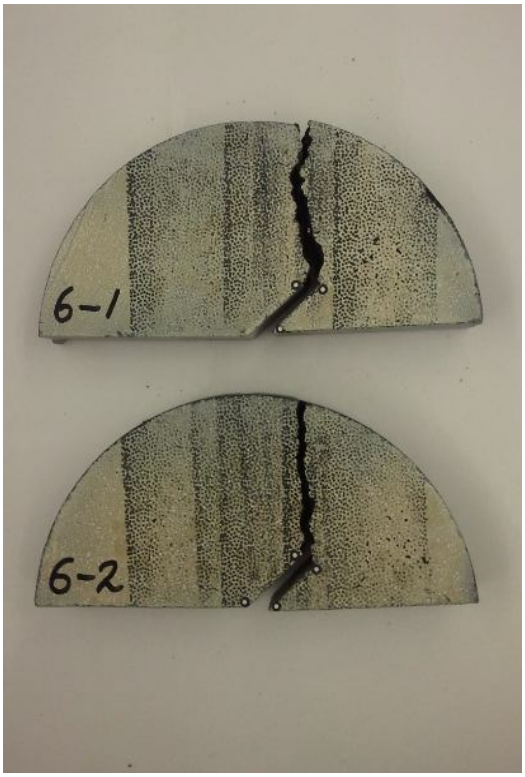

(8) 50°, s/r=0.8

(9) 50°, Mode II, 200 mm/min

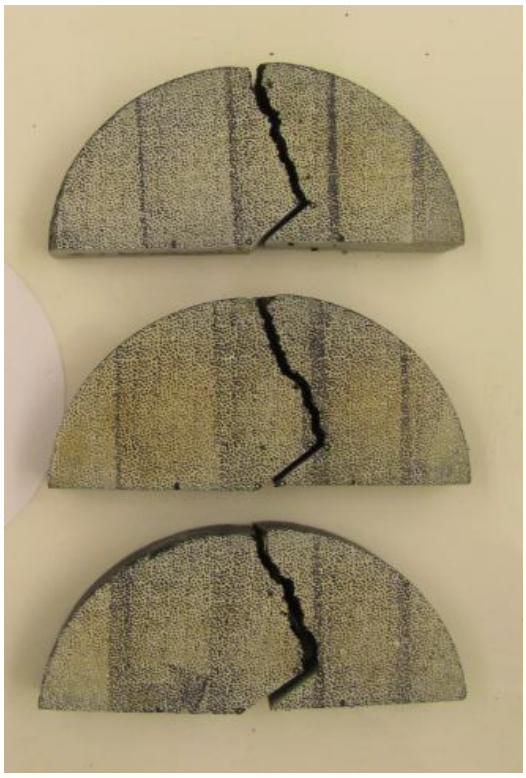

(10) 50°, Mode II, 50 mm/min

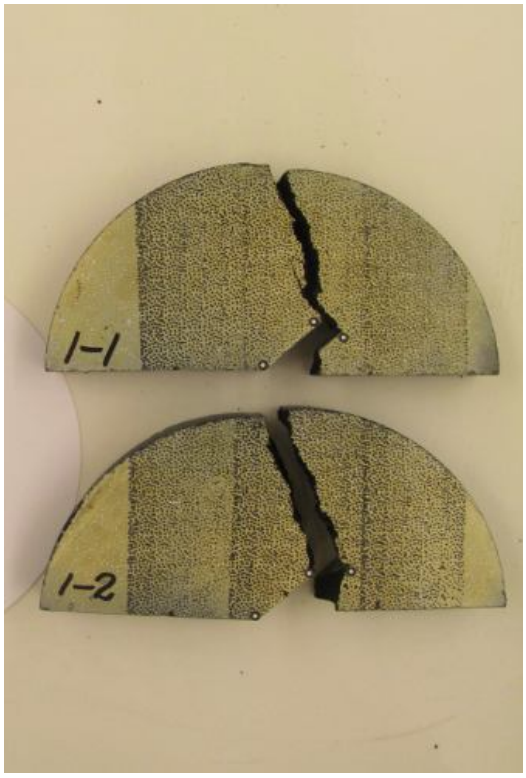

(11) 50°, Mode II, 10 mm/min

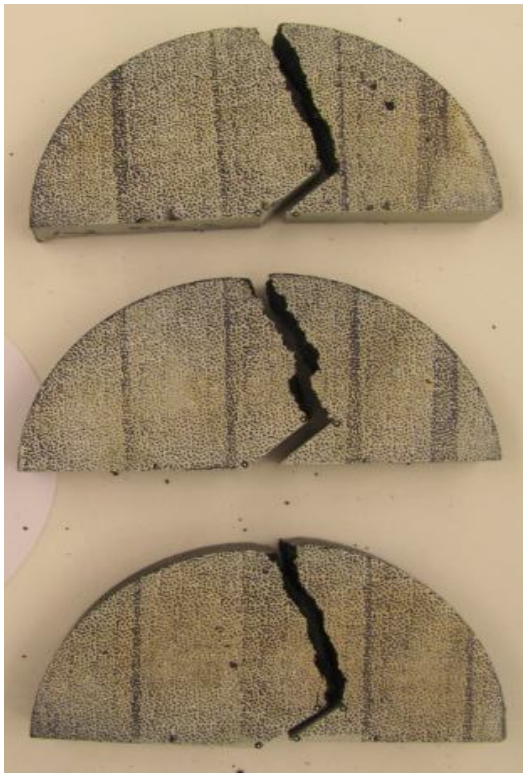

(12) 50°, Mode II, 5 mm/min

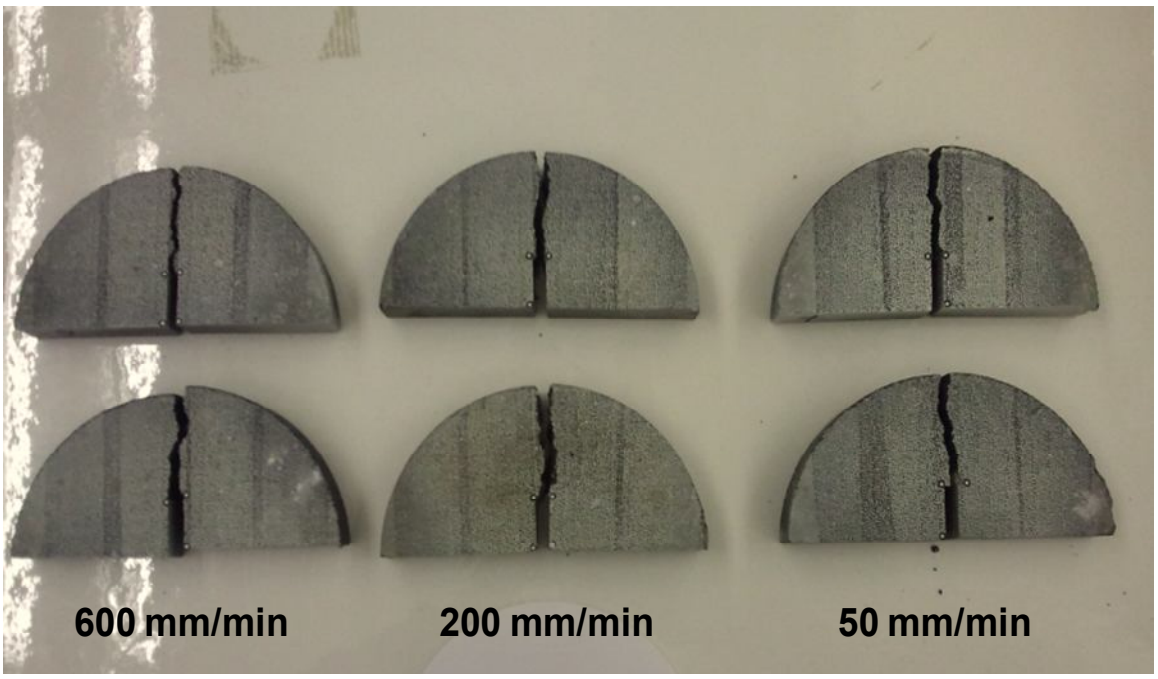

(13) Mode I

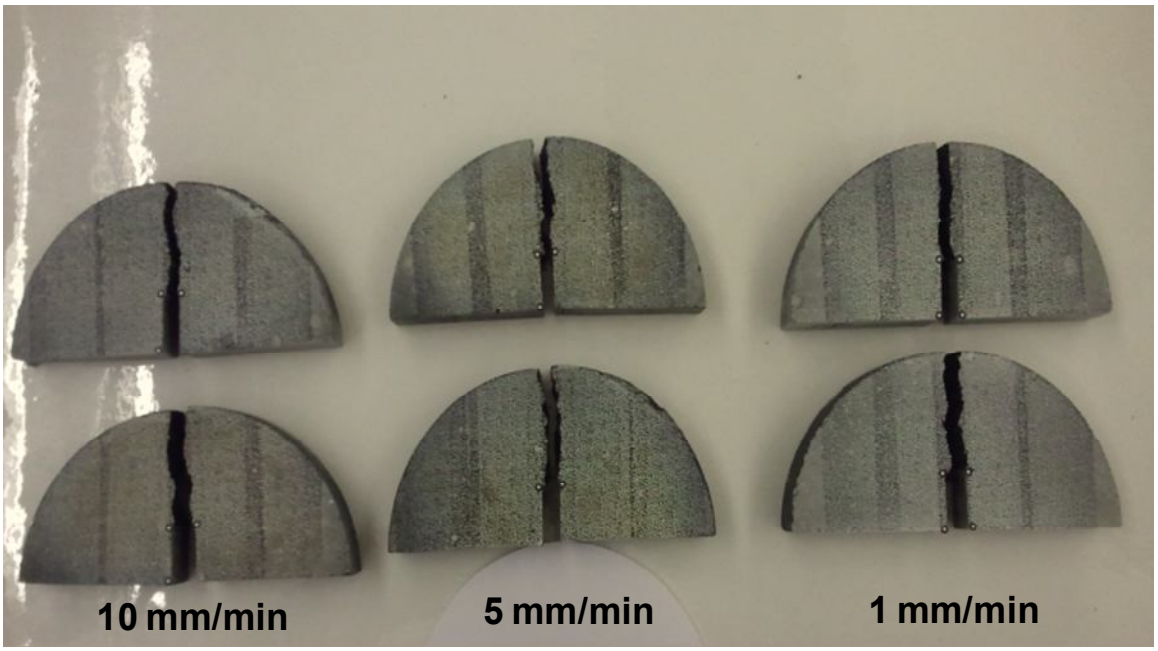

(14) Mode I